Models of microstructure and magnetic properties for magnetic recording media

Verdes, Claudiu Georgel

Models of Microstructure and Magnetic Properties for Magnetic Recording Media

Claudiu Georgel Verdes

B. Sc., M. Phil.

Thesis submitted in candidature of the degree of

Doctor of Philosophy

Department of Physics

Durham University

October 2003

Acknowledgements

I would like to thank Roy for all the help he provided on these projects and for the humour he never forgot to bring along at every meeting. Even when from distance, he helped me focus on the important issues of my work.

I also want to acknowledge the help I received from Prof. Phil Bissell and Prof. Brian Tanner on both the scientific and administrative side.

Financial support from Imation Corp. and Seagate Corp. is gratefully acknowledged.

Many, many thanks to my friends in England, at home and across Europe. Not only they made my time so much more enjoyable but they really helped me through some difficult moments.

Last but not least, my thoughts go to my family. Mom, dad, I cannot thank you enough for all your support. Cami and Cristi, Irina and Stefan, you were always by my side. Ioana, thinking of you brought a smile upon my face.

Claudiu Verdes

Models of Microstructure and Magnetic Properties for Magnetic Recording Media

Thesis submitted in candidature of the degree of Doctor of Philosophy

2003

Three computational models have been developed to simulate magnetic properties of granular media, particulate media microstructures and self-assembled systems.

The granular media model uses an energy minimisation approach to describe the magnetic properties of a system of randomly oriented single-domain particles taking into account dipolar and exchange interactions as well as thermal effects. At low temperature dipolar interactions produce flux closure vortex structures leading to a decrease of both remanence and coercivity. When thermal effects become important, dipolar interactions lead to an increase of the local energy barriers increasing both remanence and coercivity as compared to the superparamagnetic case. Exchange coupling tends to align the magnetic moments producing an increase in the remanence of such systems while cooperative reversals decrease their coercivity.

The particulate media model uses a spherocylindrical approximation for the elongated magnetic particles that are used in tapes. The particles are allowed to move in a viscous solvent under the action of steric and magnetic interactions and of the orienting field. A percentage of the particles are grouped in clusters that behave as rigid bodies during the simulation. The results obtained suggest that the presence of the clusters leads to a disruption in the alignment of the free particles regardless of the cluster size.

A third model uses a Monte-Carlo approach to describe the self-assembly process that occurs in surfactant coated magnetic particles. As the solvent dries the particles form assemblies to minimize the interaction energy. In order to obtain long-range self-assembled systems the particle areal density must be in a narrow range and the particle size distribution must have a standard deviation below 5%. The occurrence of local self-assembly is due to the presence of an attraction term in the interparticle interaction potential. The conditions under which square vs. hexagonal lattice can be obtained are discussed.

Contents

List of figures

List of tables

Chapter 1. Introduction

The interest in the behaviour of strongly interacting magnetic particles has been considerable during the last few decades due to their widespread use in the magnetic recording industry. The continuous decrease in particle size brought in by the need to increase the areal density of recorded information brought a series of new theoretical and technological problems that need to be overcome. Although some studies predicted that maximum recording density that can be achieved with conventional technologies is around $40Gb/in^2$ [1], the advances in technology made possible demonstrations of recording densities of above $100Gb/in^2$ [2].

This increase in the recording density is a result of improvements in the properties of the magnetic materials used but also of the development of new types of recording media based on different microstructures, from magnetic tapes to granular hard disks and antiferromagnetically coupled media. Therefore, a good understanding of the relationship between each type of media and its magnetic properties governed by the interaction between individual particles is required. The aim of this project is to model the properties of various media, both in terms of magnetic properties and microstructure.

The most widespread characterisation techniques for magnetic samples are hysteresis loops and remanence curves with the saturation remanence, coercivity and remanent coercivity being the most used parameters that are related to the strength of the read signal (remanence) and the strength of the field required to write information on the media (coercivity and remanent coercivity).

1.1. Fine particles

Magnetic recording media are made of ferromagnetic materials in which a spontaneous magnetisation exists. In ferromagnetic materials the individual atomic magnetic dipole moments tend to align parallel. However, the total magnetisation in the material may vary from zero to the maximum saturation value depending on the overall arrangement of the atomic dipoles. The variation in the net magnetisation of the sample is due to the existence of small regions or domains within the material. Within each domain all the atomic moments are parallel but the magnetisation orientation in different domains may be different. The boundary that separates two domains with different orientations is called a domain wall. The actual magnetic configuration within the material at a given time will be such that the total energy of the sample is a minimum.

The total energy of a ferromagnetic material in an external field can be written as:

$$E_T = E_H + E_D + E_K + E_W + E_0 \tag{1.1}$$

where $E_H = -\mu_0 \int_V \vec{H} d\vec{M}$ is the energy of the magnetic sample of volume V in an external field $\vec{H}$, E_D is the self-energy due to the demagnetising field acting in the material, E_K is the anisotropy energy, E_W is the domain wall energy and E_0 contains any other contributions that are usually less important than the other terms.

The anisotropy energy is given by the fact that in some materials there are directions that, in the absence of an external field, the magnetisation prefers to be oriented along. The anisotropy can be shape, magnetocrystalline or stress induced, or it can be given by other structural characteristics of the sample. In elongated samples it is the shape anisotropy that is usually dominant. The magnetocrystalline anisotropy is caused by the crystalline structure of the material which may have within it easy directions along certain crystallographic axes. In the case of materials with hexagonal structure (Co, CrO_2) it is much harder to magnetise the specimen along any direction that it is to magnetise the specimen along the c-axis. If θ is the angle between the c-axis and the magnetic moment vector then the anisotropy energy is [3]:

$$E_K = K_0 + K_1 \sin^2\theta + K_2 \sin^4\theta + \cdots \tag{1.2}$$

where K_1 and K_2 are the anisotropy constants for the particular material. In the case of γFe_2O_3 that has a cubic structure, the cube edges are the easy directions, the body diagonals being the hardest. If $\alpha_1, \alpha_2, \alpha_3$ are the direction cosines between the cube edges and the magnetic moment vector then the anisotropy energy is given by [3]:

$$E_K = K_0 + K_1\left(\alpha_1^2\alpha_2^2 + \alpha_2^2\alpha_3^2 + \alpha_3^2\alpha_1^2\right) + \cdots \qquad (1.3)$$

The demagnetisation energy is given by the energy of the magnetic moment of the sample in the internal field generated by its magnetisation. This field is formally equal to a field produced by "free poles" that appear on the surface of the material with a density equal to the perpendicular component of sample's polarisation. Domains are formed in order to minimise this demagnetisation energy by reducing the number of free poles (Figure 1-1) [3].

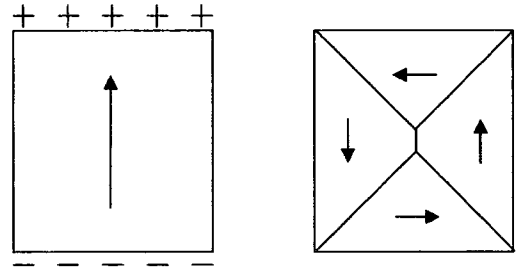

Figure 1-1. Domain formation reduces demagnetisation energy

The domain wall energy E_W is proportional to the domain wall area, the proportionality factor depending on the nature of the magnetic material.

For a single crystal in the form of a cube of edge L in the single-domain state the total demagnetisation energy is proportional to the cube volume and thus varies as L^3. In the multi-domain state for a cubic anisotropy crystal with closure domains the magnetostatic energy is zero and dominant is the wall energy which varies as L^2. Because of the different dependencies of the energy with crystal size in the two cases, there will be a critical size L_c below which the single-domain crystal will have the lower energy state (see Figure 1-2). The value of the critical size is a function of material and it depends amongst other factors on its saturation magnetisation and anisotropy constant. The shape of a particle is also very important for the critical size. Compared to a cubic or spherical particle an elongated particle will have a lower demagnetisation energy when its magnetic moment

lies along its axis. Thus, the elongated particle can have a larger volume and even a larger width than a spherical particle before breaking up into domains [3].

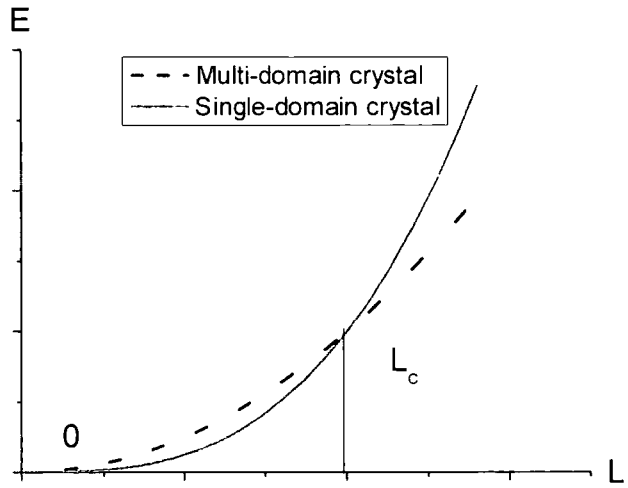

Figure 1-2. Single-domain vs. multi-domain energy variation with crystal size

Single domain particles have the properties that they cannot be demagnetised and, having no domain walls, their magnetisation can be reversed only by rotation.

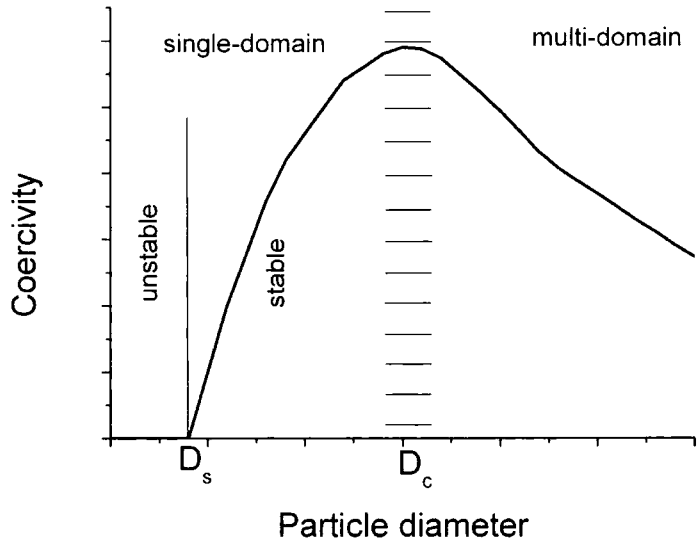

Figure 1-3. Variation of fine particle coercivity with diameter

This behaviour of the magnetic state of a particle also determines the variation of particle's coercivity with size. It is typically found that as the particle size is reduced the

coercivity increases, goes through a maximum and then tends towards zero as shown schematically in Figure 1-3 [3].

The mechanism by which the magnetisation of a particle changes differs from one part of the size range to another. In the region of large particle diameters with multi-domain state the magnetisation changes by domain wall motion. Below a critical diameter D_c which is not well defined the particle becomes single-domain and in this size range the coercivity reaches a maximum as the change in magnetisation takes place by spin rotation. As particle size decreases even further, thermal effects start to play a role in magnetisation changes and the coercivity decreases until at a certain size D_s it becomes zero.

In most commercial recording media the particle size is chosen in the stable region of single-domain behaviour, therefore throughout the model the particles are assumed to be single-domain. In the case of particulate recording media which exhibit a form or incoherent rotation, the particles are modelled as chain of spheres as will be described later.

1.2. Applications

The most widespread use of fine ferromagnetic particles is in the magnetic recording industry. Such particles with various characteristics are the storage foundation for magnetic tapes (audio and video) and hard-drives.

A variety of magnetic media have been used over the years. Very early recorders used ferrous wire. However, most modern magnetic media use a thin layer of ferromagnetic material supported by a non-magnetic substrate. The magnetic layer can be formed of magnetic particles in a polymer matrix (tapes) or the layer can be a vacuum deposited metal or oxide film (hard-drives). The use of a thin magnetic layer permits many possible configurations for the substrate. Audio recording is largely dominated by tapes, but drums and rigid disks are also used. Digital recording, although at one time was dominated by tapes, uses mostly flexible or rigid disks.

The choice of the media influences the way the magnetization is recorded on the disk. Media in which the easy axes of the particles are oriented longitudinally have a much higher remanent magnetization in the longitudinal direction, and favour longitudinal recording. This longitudinal orientation can then be supported by a head design (such as a

ring head) which promotes longitudinal fields. The result is longitudinally recorded magnetization which is the most used recording technique (see Figure 1-4) [4].

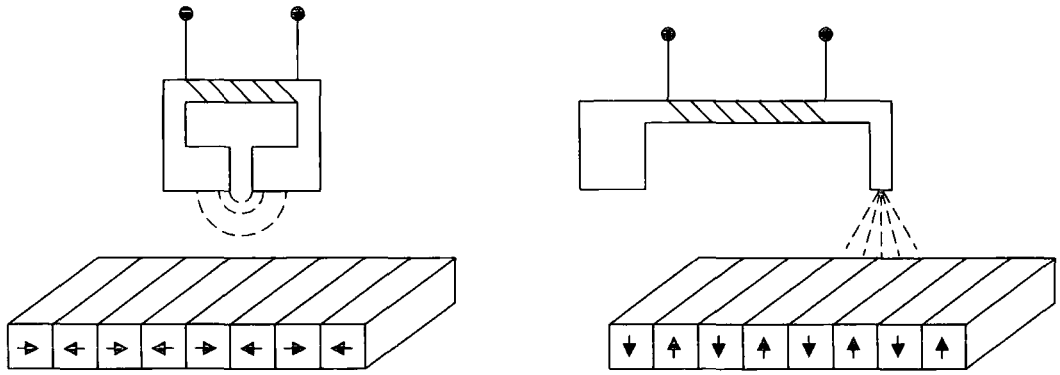

Figure 1-4. Principle of longitudinal (left) and perpendicular (right) recording

Similarly, media can be constructed with crystallites oriented perpendicularly to the field. Such media have a much higher remanent magnetization in the perpendicular direction, and favour perpendicular recording. This perpendicular orientation can then be supported by a head design such as a single pole head which promotes perpendicular fields. The result is perpendicularly recorded magnetization (see Figure 1-4) [4]. In this configuration, to obtain a perpendicular write field a single pole magnet is used for writing. The magnetic flux lines are closed via a return pole that is much larger than the write head so that the magnetic field corresponding to the return pole is sufficiently small not to change the magnetisation of the already written bits. A magnetic soft underlayer is also needed so that the magnetic flux lines close through the underlayer and not through the written bits.

The media used for magnetic recording can be classified by its microstructure which is the result of the fabrication process.

Particulate media [3],[5] are generally made of elongated ellipsoidal particles dispersed either longitudinally or transversally in a polymer matrix and are mostly used for tape applications.

Granular media [3] are obtained using film deposition techniques (plating, thermal or e-beam evaporation, DC or RF sputtering) and thus grains of magnetic material with usually random anisotropy axis are embedded into a metallic matrix that allows exchange coupling between grains. Granular media are mostly used in the production of hard-drives.

Lately, due to their potential for obtaining ultra high density recording, patterned media have become the subject of intense research [6]. They are mainly produced by lithographic techniques (e-beam, X-ray, interference) or by self-assembly effect that occurs in various natural processes. The potential for achieving very high densities with this type of media is due to the fact that it allows access to individual particles in the media thus giving the possibility of using a single particle to store a bit of information.

Although other techniques for recording information are being used (CDs, DVDs), the magnetic recording media still remain, due to the lower production costs and proven quality, the most widely used method of information storage.

1.3. Computer modelling of recording media

In order to extend the limits of the recording densities achieved a good understanding of the physics involved in such system was needed. An analytical approach of the magnetic properties of recording media is very difficult due both to the inherent complexity of multi-body systems and to the different nature of the effects (interactions, thermal activation) that occur at microscopic level in these media. Although several phenomenological models have been proposed such as Preisach [7], [8] and Jiles-Atherton [9], it is difficult to interpret the physical meaning of the parameters used in the models and to relate them to the microscopic characteristics of a specific media.

A different approach is the so-called micromagnetic simulation in which a small volume of a sample is discretised according to the microscopic characteristics of a sample in small entities with uniform magnetisation. The magnetisation of each element is considered independently but is influenced by the interactions with the other elements in the considered volume. This approach allows the use of realistic microstructure parameters that can be measured experimentally such as particle size distribution, packing density, etc. For a given configuration, micromagnetic simulations use either a dynamic description of the magnetic moments [10], a Monte-Carlo energy minimisation of the system [11] or a direct local energy minimisation [12].

Simulations of particulate recording media microstructure [13], [14] using molecular dynamics provide an understanding of the conditions required for obtaining high-

performance media. Although this kind of simulations usually requires a very simplified model of the initial particle dispersion due to its high complexity they can describe with sufficient accuracy various physical properties of the media.

Self-assembled systems are relatively new for magnetic recording media but simulations for self-assembled water/surfactant reversed micelles [15], [16] modelling biological membranes have been performed using Monte-Carlo methods, estimating the conditions required for the self-assembly process to take place.

1.4. Aim of the project

The initial goal of this project was gaining an insight by means of micromagnetic calculations into the way that interparticle interactions influence the behaviour of magnetic granular systems in the presence of thermal activation. Although a lot of effort has been put into research in this area, there is still a lot of contradiction in theoretical results obtained by different authors, using either phenomenological [17], [18], [19], [20], [21], [22], [23] or micromagnetic models [11], [12]. Two main phenomenological models addressing weakly interacting superparamagnetic particle systems (Dormann et. al. [17], [18], [19] and the Morup et. al. [20] , [21], [22]) give opposite results, therefore the need for further clarifications on this issue by using a micromagnetic model. A systematic approach on the influence of various parameters on such particle system was needed to extend these results to other regimes of interaction and temperature effects.

Following the development of the model it became obvious that the formalism could be adapted to a much wider category of magnetic particle systems such as particulate and self-assembled media. To obtain realistic properties of such systems, their microscopic configuration needed to be reproduced. Although in the case of particulate media previous models of the fabrication process have been developed [13], [24], [25], [26], they failed to correctly reproduce important experimental parameters such as the remanence of the hysteresis loop, an issue that is addressed in the particulate media model presented here by the introduction of particle clusters. No previous simulations of self-assembled magnetic particles have been published thus the self-assembly model presented here was based on ferrofluid results [27].

No previously written code has been used in any of the models presented here and, except where referenced, all algorithms were originally developed.

Details of all these models along with the results obtained and comparison with previously published data are presented in the next chapters. Some of the results [28], [29], [30], [31], [32] have already been already published in refereed journals.

Chapter 2. Models of magnetization calculation

2.1. Introduction

Finding the magnetisation state of a magnetic sample is a complicated task due to the nonlinearity in the dependence of $\vec{M}$ on $\vec{H}$ and to the large number of factors that need to be taken into account in order to find a theoretical dependence for a specific case. For a relatively large sample, the magnetisation state is governed mostly by the properties of the material, its shape, the motion of the domain walls which is related to the number and positions of defects and impurities in the structure of the material, the magnetic and thermal history of the sample and the actual applied field and temperature of the sample at the moment when the magnetisation is measured. Even inside a magnetic domain, the local magnetisation is not uniform, small variations occurring due to thermal agitation, interaction and edge effects. For discrete samples where small regions of magnetic material are separated by regions of non-magnetic material (such as magnetic particles found in commercial tapes or granular systems used in hard drives) the orientation of the magnetic moment can change even by 180° from one magnetic region to an adjacent one. Therefore a convenient way to treat this complicated problem is to discretize large continuous samples into a number of very small interacting volumes with uniform magnetisation and to treat all the magnetic regions of discrete samples as being uniformly magnetised. Then, for each of these uniformly magnetised volumes, simple models assuming coherent rotation are used to find the local orientation of the magnetic moment knowing its history, the external field, temperature and interaction effects produced by the other uniformly magnetised volumes in the considered sample. In this chapter several of the most widely used models are presented.

2.2. *The Stoner-Wohlfarth model*

2.2.1. Theoretical model

The Stoner-Wohlfarth model [33] is one of the simplest models in magnetism and describes the properties of single domain particles whose atomic moments are assumed to rotate coherently. The equilibrium position of the magnetic moment of a single domain particle with uniaxial anisotropy in the presence of a magnetic field is found by minimising the total energy of the particle [34].

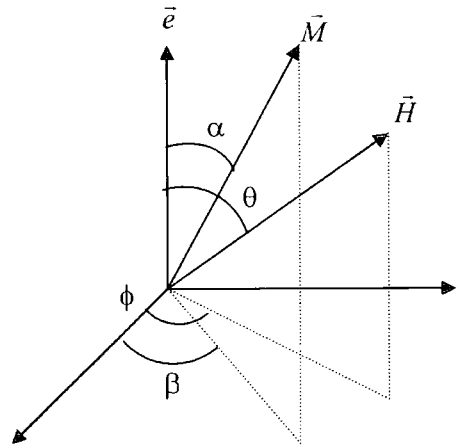

Figure 2-1. Stoner-Wohlfarth particle axis system

Considering the system of coordinates in Figure 2-1, with the easy axis $\vec{e}$ of the particle along the z–axis, the total energy density of the particle can be expressed as the sum of the anisotropy and the magnetostatic energies:

$$E = E_K + E_H \tag{2.1}$$

with

$$E_K = KV(1-\cos^2\alpha), \tag{2.2}$$

$$E_H = -\mu_0 \vec{H}\cdot\vec{M} = -\mu_0 HM_S V(\cos\alpha\cos\theta + \sin\alpha\sin\theta\cos(\phi-\beta)) \tag{2.3}$$

K the anisotropy constant, μ_0 the vacuum permeability, $\vec{M}$ the magnetisation, M_S the saturation magnetisation for the considered ferromagnetic particle and V the volume of the particle.

The energy will be minimum if the energy derivatives with respect to the magnetisation angles are zero:

$$\frac{\partial E}{\partial \alpha} = 0 \tag{2.4}$$

$$\frac{\partial E}{\partial \beta} = 0 \tag{2.5}$$

The second condition yields:

$$\mu_0 H M_S \sin\alpha \sin\theta \sin(\phi - \beta) = 0 \tag{2.6}$$

with the solutions

$$\alpha = 0 \text{ and } \beta = \phi \tag{2.7}$$

It is easy to verify that the condition $\alpha = 0$ is not a minimum so the only solution remains $\beta = \phi$. This means that the easy axis, the magnetic field and the magnetic moment of the particle lie in the same plane.

Using this, the condition (2.4) yields:

$$2K \cos\alpha \sin\alpha - \mu_0 H M_S(-\sin\alpha \cos\theta + \cos\alpha \sin\theta) = 0 \tag{2.8}$$

With the notations

$$H_K = 2K / \mu_0 M_S \text{ and } h = H / H_K \tag{2.9}$$

the expression becomes:

$$\sin 2\alpha + 2h \sin(\alpha - \theta) = 0 \tag{2.10}$$

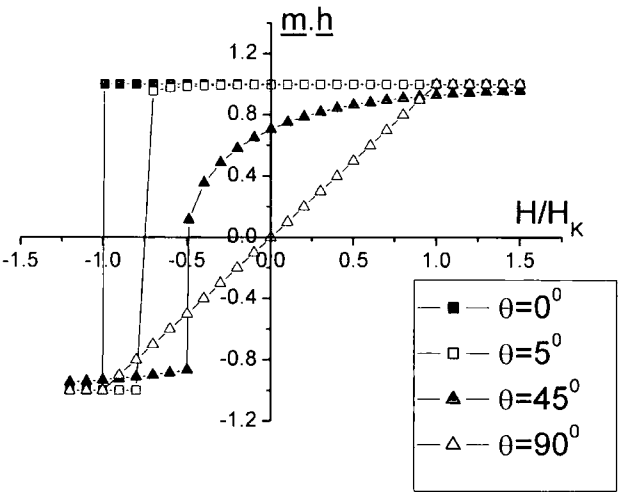

Figure 2-2. Magnetization curves for a Stoner-Wohlfarth particle

This equation does not have an analytical solution for the general case, but it can easily be solved numerically. It is easy to show analytically that for the $\theta = 0°$ case the

magnetization curve has a rectangular shape with a reduced switching field of -1, for $\theta = 45°$ the reduced switching field is 0.5 while for $\theta = 90°$ the field component of the magnetization is linear with the reduced field between $+1$ and -1, results that are also shown in Figure 2-2, along with a magnetization curve for a value of θ for which analytical solution of equation (2.10) is difficult to find.

In order to find the number of solutions for equation (2.10) we can rewrite (2.8) using the following notations:

$$h_z = \frac{H\cos\theta}{H_k},\ h_x = \frac{H\sin\theta}{H_k} \tag{2.11}$$

$$\frac{1}{2}\sin 2\alpha + h_z \sin\alpha - h_x \cos\alpha = 0 \tag{2.12}$$

For a solution of this equation to be an energy minimum, the condition

$$\frac{\partial^2 W}{\partial \alpha^2} \geq 0 \tag{2.13}$$

must be fulfilled. This becomes:

$$\cos 2\alpha + h_z \cos\alpha + h_x \sin\alpha \geq 0 \tag{2.14}$$

Thus, the conditions for the energy minima (2.12) and (2.14) can be conveniently rewritten as:

$$h_x \cos\alpha - h_z \sin\alpha = \frac{1}{2}\sin 2\alpha \tag{2.15}$$

$$h_x \sin\alpha + h_z \cos\alpha \geq -\cos 2\alpha \tag{2.16}$$

The system of equations obtained by replacing the "≥" sign with "=" in the stability equation above determines the parametric equations $h_x = h_x(\alpha)$ and $h_z = h_z(\alpha)$ that separate the area in the (h_x, h_z) plane where the energy as a function of α has two minima from the area where it has just one minimum. Multiplying (2.15) with $\cos\alpha$ and (2.16) with $\sin\alpha$ and adding the results one obtains:

$$h_x \cos^2\alpha + h_x \sin^2\alpha = \sin\alpha\cos^2\alpha - \sin\alpha\cos^2\alpha + \sin^3\alpha \tag{2.17}$$

or

$$h_x = \sin^3\alpha \tag{2.18}$$

Similarly, the parametric equation for h_z becomes:

$$h_z = -\cos^3 \alpha \tag{2.19}$$

Eliminating α from the last two equations, one obtains

$$h_x^{2/3} + h_z^{2/3} = 1 \tag{2.20}$$

representing an astroid in the (h_x, h_z) plane as shown in Figure 2-3. If the (h_x, h_z) representation of the local field is inside the astroid, there are two equilibrium solutions for α. Otherwise there is only one equilibrium solution.

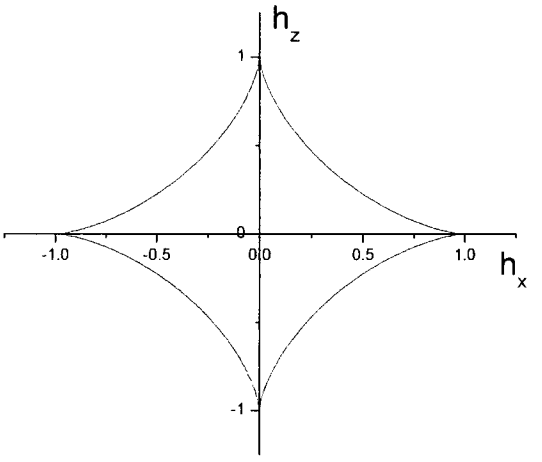

Figure 2-3. The Stoner-Wohlfarth astroid

2.2.2. Numerical approach

Finding an approximate solution for equation (2.10) with the stability condition (2.14) can be achieved using any numerical method for equation solving. In particular, the Newton-Raphson method is one of the fastest but for this method to work properly it needs to start with a relatively good initial approximation of the solution. This initial approximation can be found with another numerical method like bisection or by using a look-up table with solutions for different values of h and θ. However, it turns out that in the model, the most convenient way to store the orientation of the magnetic moment and easy axis is not by using polar angles but rather by using the (x, y, z) components with the constraint that the modulus of the vector is 1. This approach avoids computationally expensive calculations of trigonometric functions for expressions involving scalar products and vector arithmetic leading to a considerable increase in the speed of the program. In

view of this, a direct solution of equation (2.10) would involve again several trigonometric functions and, furthermore, once the equilibrium value of α has been found, a coordinate transformation to find the (x, y, z) triplet corresponding to a moment lying in the same plane as $\vec{e}$ and $\vec{h}$, at an angle α with respect to $\vec{e}$.

To avoid this overhead, a new numerical approach has been developed to find the equilibrium position for the magnetic moment of a Stoner-Wohlfarth particle. The method is based on the fact that a magnetic moment, in the absence of anisotropy, aligns to the direction of the total local field. The effect of the anisotropy is replaced by an "effective anisotropy field", for which an expression is found by formal differentiation of the anisotropy expression with respect to the magnetisation.

$$\vec{H}_{eff} = -\frac{1}{\mu_0}\frac{\partial E_K}{\partial \vec{M}} \tag{2.21}$$

where $\vec{H}_{eff}$ is the effective anisotropy field and $\vec{M}$ the magnetisation of the particle.

Considering that

$$\vec{M} = VM_S\vec{m} \tag{2.22}$$

and

$$E_K = KV\left(1-\cos^2\alpha\right) = KV\left(1-(\vec{e}\cdot\vec{m})^2\right) \tag{2.23}$$

with $\vec{m}$ the magnetisation orientation, equation (2.21) becomes

$$\vec{H}_{eff} = \frac{2K(\vec{e}\cdot\vec{m})\vec{e}}{M_S} = H_K(\vec{e}\cdot\vec{m})\vec{e} \tag{2.24}$$

or, in reduced units,

$$\vec{h}_{eff} = (\vec{e}\cdot\vec{m})\vec{e} \tag{2.25}$$

Thus the reduced effective anisotropy field is simply the projection of the magnetisation orientation vector on the easy axis. Since this value depends on the magnetisation orientation, the process of finding the equilibrium position of the magnetisation will be an iterative one.

Knowing the local magnetic field in relative units $\vec{h}$ the initial orientation of the magnetisation $\vec{m}$ and the orientation of the easy axis $\vec{e}$, the total field, including the effective anisotropy field term becomes

$$\vec{h}_{tot} = \vec{h} + (\vec{e} \cdot \vec{m})\vec{e} \tag{2.26}$$

The new magnetisation orientation will be the orientation of the total field

$$\vec{m}' = \frac{\vec{h}_{tot}}{h_{tot}} \tag{2.27}$$

and the process is repeated until the magnetisation orientation vector doesn't change significantly from one step to the next one.

The algorithm performs very well in the sense that is stable, and usually only 4-6 iterations are required to obtain a solution with a precision of 10^{-8} when the magnetisation doesn't need to switch from one equilibrium position to the other. However, when a switch occurs, the number of iterations needed increases to over 100. To avoid this kind of problem, the numerical algorithm checks first for the existence of one or two solutions using (2.20). If only one solution is to be found, the algorithm starts with an initial approximation for $\vec{m}$ taken as $\frac{\vec{h} \cdot \vec{e}}{|\vec{h} \cdot \vec{e}|}\vec{e}$. Otherwise the two different solutions are found starting with initial approximations for $\vec{m}$ taken as $\vec{e}$ and $-\vec{e}$ respectively. The C++ source code for the algorithm is given in Appendix 1.

2.3. The Landau-Lifshitz model

Unlike the Stoner-Wohlfarth model that describes the equilibrium state of a magnetic single-domain particle, the Landau-Lifshitz model [35] describes the dynamic behaviour of the particle's magnetisation vector in the presence of a local magnetic field.
In the absence of any damping or friction, a magnetic dipole undergoes a precession around the direction of the magnetic field governed by the equation:

$$\frac{\partial \vec{M}}{\partial t} = -\gamma \vec{M} \times \vec{H} \tag{2.28}$$

where $\vec{M}$ is the magnetisation of the dipole, γ is the electron gyromagnetic ratio and $\vec{H}$ the total field acting on the dipole.

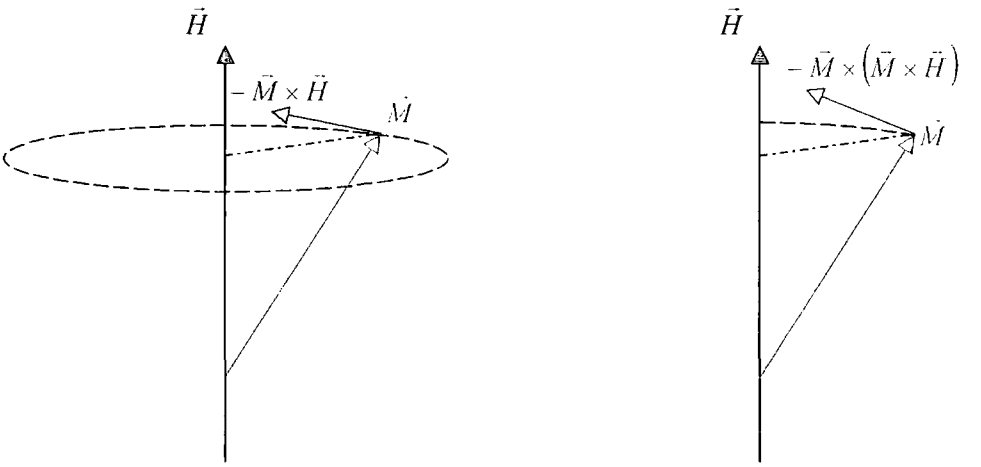

Figure 2-4. Effects of the two terms of the LL equation: a) - gyroscopic b) - frictional

To take into account the fact that in reality the magnetic dipole reaches an equilibrium state, a "frictional" term (see Figure 2-4) was added to equation (2.28) using a phenomenological damping parameter α

$$\frac{\partial\vec{M}}{\partial t}=-\gamma\,\vec{M}\times\vec{H}-\frac{\alpha\gamma}{M}\vec{M}\times\left(\vec{M}\times\vec{H}\right) \tag{2.29}$$

Equation (2.29) is usually referred as the Landau-Lifshitz equation.

A modified form of (2.29) known as Landau-Lifshitz-Gilbert equation is used [36] in order to make the energy dissipation proportional to the dipole's gyration speed.

$$\frac{\partial\vec{M}}{\partial t}=-\gamma\,\vec{M}\times\vec{H}-\frac{\alpha\gamma}{M}\vec{M}\times\left(\vec{M}\times\frac{\partial\vec{M}}{\partial t}\right) \tag{2.30}$$

Equations (2.29) and (2.30) are equivalent for small values of the damping parameter α.

However, equation (2.29) has an unrealistic behaviour for large values of α in the sense that the time required for a reversal of the orientation of the magnetic moment continuously decreases with the increase of α. To compensate for this effect, a modified form of (2.29) obtained by adding a $1/(1+\alpha^2)$ factor is used [36]:

$$\frac{\partial\vec{M}}{\partial t}=-\frac{\gamma}{1+\alpha^2}\vec{M}\times\vec{H}-\frac{\alpha\gamma}{(1+\alpha^2)M}\vec{M}\times\left(\vec{M}\times\vec{H}\right) \tag{2.31}$$

In our model, a dimensionless form of equation (2.31) was used. Considering that the dipole describes a magnetic particle of volume V, saturation magnetisation M_S and orientation of the magnetic moment $\vec{m}$ and using the notations:

$$\vec{h} = \frac{\vec{H}}{M_S} \tag{2.32}$$

and

$$\tau = t\frac{|\gamma|M_S}{1+\alpha^2} \tag{2.33}$$

equation (2.31) can be rewritten in reduced terms as:

$$\frac{\delta\vec{m}}{\delta\tau} = -\vec{m}\times\vec{h} - \alpha\left[\vec{m}\times\left(\vec{m}\times\vec{h}\right)\right] \tag{2.34}$$

Thus, for a magnetic particle with anisotropy, the dynamic behaviour of its magnetic moment can be described by equation (2.31) using the anisotropy effective field (2.21) described in the previous section.

In the model, it is assumed that particles have the uniaxial anisotropy effective field given by (2.24) and the set of coupled differential equations of the form (2.34) is solved using an adaptive-step Runge-Kutta integration method [37].

2.4. *Temperature effects. Arhennius-Néel law*

2.4.1. Theoretical model

As earlier described the magnetic moment of a Stoner-Wohlfarth uniaxial particle can have two equilibrium positions when the local magnetic field is below a critical value given by equation (2.20). In this case, in the energy minimisation approach of the Stoner-Wohlfarth model one of the two equilibrium orientations is chosen depending on the "previous" orientation of the magnetic moment. Once this equilibrium position is found, the only way to change the orientation of the magnetic moment is to change the orientation and/or magnitude of the local magnetic field. However, in reality spontaneous switches of the magnetic moment from one equilibrium orientation to the other happen because of thermal activation effects [38], [39].

Considering an assembly of n identical ferromagnetic particles with two equilibrium positions for the orientation of the magnetic moment, let n_1 be the number of particles with "positive" magnetisation, n_2 the number of particles with negative magnetisation, ν_{12} the probability of a particle to undergo a transition from "positive" to "negative" magnetisation and ν_{21} the probability of a particle to undergo a transition from "negative" to "positive" magnetisation. Here the terms "positive" and "negative" are used to represent the two equilibrium orientations of the magnetic moment.

Since the total number of particles n is constant, we have:

$$n = n_1 + n_2 \tag{2.35}$$

and thus

$$\dot{n}_1 = -\dot{n}_2 = \nu_{21} n_2 - \nu_{12} n_1 \tag{2.36}$$

or

$$\dot{n}_1 = \nu_{21} n - (\nu_{21} + \nu_{12}) n_1 \tag{2.37}$$

with the solution

$$n_1 = \frac{\nu_{21}}{\nu_{21} + \nu_{12}} n + n_{10} \exp\left(-(\nu_{12} + \nu_{21})t\right) \tag{2.38}$$

where n_{10} is the initial number of particles with positive magnetisation. At equilibrium, n_1 and n_2 will be constant and determined by the ratio of the transition probabilities:

$$\frac{n_1}{n_2} = \frac{\nu_{21}}{\nu_{12}} \tag{2.39}$$

By analogy with other processes, it is usual to suppose that [40]

$$\nu_{ij} = \nu_{ij}^0 \exp\left(-V(W_m - W_i)/k_B T\right) \tag{2.40}$$

with $i = 1,2$ and $j = 3 - i$ where W_m is the particle energy density corresponding to the top of the barrier between orientations i and j, W_i is the particle energy density in orientation i, V is the volume of the particle, k_B is the Boltzmann constant and T the temperature. The preexponential factors ν_{ij}^0 are often considered to be constant as even if they are temperature dependent their dependence is much smaller than the exponential factor [41].

Equation (2.40) with the appropriate numerical values shows that when the ratio V/T changes by a factor of less 3 in a critical part of its range the time constant changes

from 10^{-1}s to 10^{9}s, so that it is possible to define a critical volume V_c so that particles with $V < V_c$ exhibit no hysteresis because of spontaneous reversals of the magnetic moment orientation and particles with $V > V_c$ do not exhibit spontaneous reversals thus exhibiting hysteresis. For an average reversal time t, the critical volume becomes:

$$V_c = \frac{k_B T}{W_m - W_i} \ln(\nu_{ij}^0 t) \tag{2.41}$$

Usually it is considered that the preexponential factors for the two possible values of i and j are equal, $\nu_{12}^0 = \nu_{21}^0 = f_0$. With this notation, the critical volume (2.41) becomes [42]:

$$V_c = \frac{k_B T}{W_m - W_i} \ln(f_0 t) \tag{2.42}$$

It has been shown [43] for the case of particles with uniaxial anisotropy that the so called attempt frequency f_0 depends on the anisotropy constant K, the particle volume v, the anisotropy field H_K, temperature T and the electron gyromagnetic ratio γ_0:

$$f_0 = \sqrt{\frac{KV}{\pi k_B T}} \gamma_0 H_K \tag{2.43}$$

However, this quantity is usually taken to be constant, with a value of 10^9 to 10^{10} s^{-1}.

The probability p of a particle to make a transition from positive to negative or from negative to positive magnetisation orientation in a time interval t is given by the ratio $\frac{\Delta n_1}{n_{10}}$ between the number of particles making the transition and the initial number of particles with positive orientation. With (2.38) the expression yields:

$$p(t) = \frac{n_{10} - n_1(t)}{n_{10}} = 1 - \exp(-(\nu_{12} + \nu_{21})t) \tag{2.44}$$

or [12]:

$$p(t) = 1 - \exp\left(-\frac{t}{\tau}\right) \tag{2.45}$$

with the notation

$$\frac{1}{\tau} = \nu_{12} + \nu_{21} = f_0 \left(\exp\left(-\frac{E_m - E_1}{k_B T} \right) + \exp\left(-\frac{E_m - E_2}{k_B T} \right) \right) \tag{2.46}$$

known as the Arhennius-Néel law.

2.4.2. Numerical approach

In the model, in order to implement thermal activations via the Arhennius-Néel law, the decay factor (2.46) needs to be calculated. For that, apart from the particle energies E_1 and E_2 in the equilibrium orientations of the magnetic moment which can be found using the Stoner-Wohlfarth model, the energy corresponding to the magnetic moment orientation for which the particle energy is maximum in a given field is needed.

For the case of aligned easy axis, the expression for the energy barrier $\Delta E = E_m - E_1$ can be easily found and has the form:

$$\Delta E(H) = KV\left(1 - \frac{H}{H_K}\right)^2 = \Delta E_0 (1-h)^2 \tag{2.47}$$

When the magnetic field is oriented as some angle ψ with respect to the easy axis, an approximate value for the energy barrier has been found numerically [44] as:

$$\Delta E(H,\psi) = \Delta E_0 \left(1 - \frac{h_T}{g(\psi)}\right)^{k(\psi)} \tag{2.48}$$

with $g(\psi) = \left(\cos^{2/3}\psi + \sin^{2/3}\psi\right)^{3/2}$ and $k(\psi) = 0.86 + 1.14 g(\psi)$.

However, in the model a different approach to directly find the orientation of the magnetic moment for which the particle energy is maximum has been used.

This method, relies on the fact that the maximum of an expression $e(x)$ is a minimum for the expression $-e(x)$. Considering the expression for the particle energy given by (2.1), the maximum energy orientation will be the orientation for which

$$-E(\vec{M}) = -VK\sin^2\alpha + \mu_0 V\vec{H}\cdot\vec{M} \tag{2.49}$$

has a minimum.

The expression can be rewritten, adding a constant term K that does not change the position of the minimum and considering that $\sin\alpha = \cos\left(\frac{\pi}{2} - \alpha\right)$, as:

$$-E(\vec{M}) + K = VK\left(1 - \cos\left(\frac{\pi}{2} - \alpha\right)^2\right) - \mu_0 V\left(-\vec{H}\right)\cdot\vec{M} \tag{2.50}$$

This expression is similar to the expression for the total energy of a uniaxial particle with the easy axis perpendicular on the initial easy axis of the particle and with the applied field in the opposite direction of the original applied field.

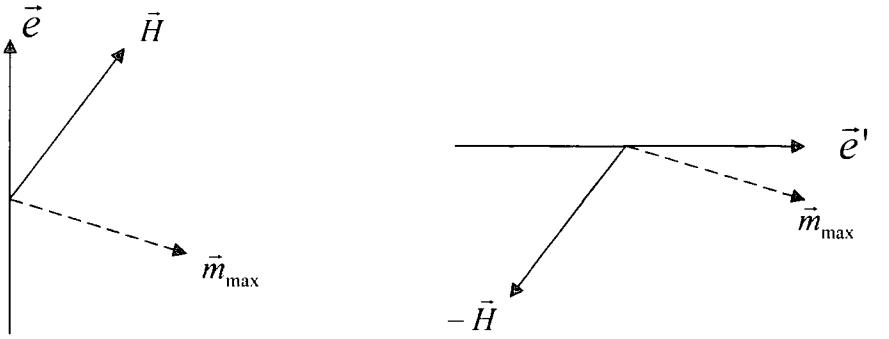

Figure 2-5. Axis transformation used to find the maximum energy orientation of the magnetic moment: a) - original particle b) – hypothetical rotated particle

Thus, in order to find the orientation for which the particle energy is maximum, a hypothetical Stoner-Wohlfarth particle is considered with the easy axis rotated with 90° in the $(\vec{e}, \vec{H})$ plane, upon which a magnetic field $-\vec{H}$ is acting, as shown in Figure 2-5. The equilibrium orientation that is nearest to the orientation of $\vec{H}$ for the hypothetical Stoner-Wohlfarth particle will be the magnetic moment orientation for which the initial particle has maximum energy. This way, the energy barrier needed for the calculation of the Arhennius-Néel law can be determined directly. The C++ code for the algorithm is given in Appendix 2.

With this value known, the transition probability p is easily determined from (2.45), a random number x is generated from a uniform distribution between 0 and 1 and this number is compared with the value of p. If $x > p$ transitions are not allowed and the equilibrium orientation that is nearest to the initial orientation of the particle is chosen. Otherwise, transitions are allowed and a choice is made between the two equilibrium positions using the following algorithm. The equilibrium ($t \to \infty$) probability for the magnetic moment to go in the orientation 1 is calculated from (2.38) and (2.40) as:

$$p_1 = \frac{\exp\left(\frac{E_2}{k_B T}\right)}{\exp\left(\frac{E_1}{k_B T}\right) + \exp\left(\frac{E_2}{k_B T}\right)} \tag{2.51}$$

A random number y is generated from a uniform distribution between 0 and 1 and y is compared with p_1. If $y < p_1$ orientation 1 is chosen. Otherwise orientation 2 is the preferred one.

2.5. *Superparamagnetic particles. Metropolis algorithm*

As shown in (2.41), there is a critical volume or particle size below which the probability of a magnetic moment transition from one equilibrium orientation to the other is close to 1, and the particle magnetisation loop exhibits no hysteresis. In fact, for such small particles the thermal agitation energy is so important that it overcomes the anisotropy energy and its magnetic moment no longer is in one of the equilibrium orientations but can take with a non-zero probability almost any orientation in space.

For such particles, an external applied field will tend to align their moments while the thermal energy will tend to misalign them. This is similar to the behaviour of paramagnetic materials except that the magnetic moments involved in this case are several orders of magnitude larger than in the case of paramagnets. Thus this kind of behaviour is known as "superparamagnetism" and the particles exhibiting it are known as "superparamagnetic" particles [42].

The criterion that is generally used to consider a particle as being superparamagnetic is that its decay time from one equilibrium orientation to the other is less than 100s which is the average time for magnetic measurements taken with vibrating-sample magnetometers. For a particle with the easy axis aligned to the direction of the applied field, using (2.46) and (2.47), the criterion becomes [3]:

$$Kv = 25k_BT \tag{2.52}$$

This expression shows that for a particle of a given volume, there is a temperature value separating the superparamagnetic and stabile behaviour of the particle, value usually referred to as "blocking temperature".

The superparamagnetic behaviour is modelled using a well known Monte-Carlo method, the standard Metropolis algorithm [45] that, for a magnetic particle in a known local field, performs as follows:

1. The initial energy of the particle E is calculated

2. The orientation of the magnetic moment is changed with a small random amount
3. The energy of the particle E' with the magnetic moment in the new orientation is calculated
4. The probability for the change in orientation to be accepted is calculated as:

$$p_a = \min\left(1, e^{-\frac{E'-E}{k_B T}}\right) \tag{2.53}$$

5. A random number z between 0 and 1 is generated from a uniform distribution
6. If $z < p_a$ the change is accepted and the magnetic moment stays in the new orientation. Otherwise, the change is rejected and the magnetic moment returns to its initial orientation.

After a large number of such Monte-Carlo steps, a system of superparamagnetic particles reaches thermal equilibrium, with a Boltzmann distribution of energies.

2.6. Interaction calculations

In order to find the equilibrium orientation of the magnetic moment for a particle, the magnitude and orientation of the local magnetic field acting upon that particle have to be known. Usually, this local field H_{loc} has two major components:

$$\vec{H}_{loc} = \vec{H}_{appl} + \vec{H}_{\text{int}} \tag{2.54}$$

H_{appl} - the external applied field and $\vec{H}_{\text{int}}$ - the interaction field produced by the other particles in the considered system.

The interaction field produced by a particle j on a particle i has in general two components, a dipolar one and an exchange coupling one. The dipolar interaction field is usually expressed as:

$$\vec{H}_{\text{int}}^{ji} = \frac{3\left(\vec{M}_j \cdot \vec{r}_{ij}\right)\vec{r}_{ij} - \vec{M}_j r_{ij}^2}{r_{ij}^5} = \frac{V_j}{r_{ij}^3} M_s \left(3\left(\hat{m}_j \cdot \hat{r}_{ij}\right)\hat{r}_{ij} - \hat{m}_j\right) \tag{2.55}$$

with $\vec{M}_j$ the magnetic dipole of the j particle, $\vec{r}_{ij}$ the distance vector from one particle to the other, $r_{ij} = \left|\vec{r}_{ij}\right|$, V_j the volume of the j particle, M_s the bulk saturation magnetisation of

the j particle, $\hat{m}_j$ the unit vector representing the orientation of the magnetic moment of the j particle and $\hat{r}_{ij} = \frac{\vec{r}_{ij}}{r_{ij}}$.

The exchange coupling field produced by particle j on particle i is has the form:

$$\vec{H}_{exch}^{ji} = C^* H_K \hat{m}_j \tag{2.56}$$

with C^* a phenomenological exchange coupling constant and H_K the anisotropy field defined by (2.9). However, exchange coupling interactions can only occur in certain types of systems and are of a very short range so that they are present only if the two particles are "close enough". In our model, we consider that, when exchange coupling is allowed, it only occurs between particles that have surface-to-surface separation below a given "exchange coupling distance" parameter, d_{exch}.

In order to find the total interaction field for all particles in a system of n particles, a summation over $n-1$ particles is required yielding an algorithm of the order $O(n(n-1))$ which can become very computational time consuming for large systems. Faster algorithms of the order $O(n\ln(n))$ relaying on Fast Fourier Transformations have been developed [46] for systems with periodic positions of particles but for non-organised systems these algorithms cannot be used. In order to increase the speed of the interaction field calculation for such systems, some approximations have to be used.

The expression for the long range dipolar interaction field (2.55) shows that the magnitude of the field acting on a particle decreases with the cube of the distance between the considered particle and the particle interacting with it, $H(r) \propto r^{-3}$ while the number of particles that are at a distance between r and $r+\delta r$ from the considered particle is proportional with the square of the distance, $m(r) \propto r^2$. Therefore, the magnitude of the total interaction field produced by these particles continuously decreases with the distance considered $H(r) \propto r^{-1}$. Thus, as an approximation, only the particles that are at a distance smaller than a conveniently chosen "cut-off radius", r_{cut} can be considered for the summation required for the interaction field calculation.

However, the contributions from the particles outside the cut-off radius cannot be neglected as $\int_{cut}^{\infty} r^{-1} dr = \infty$. With a good approximation these contributions can be found easily considering that the part of the sample outside the cut-off radius is uniformly magnetised with the magnetisation equal with the average magnetisation of the total sample. This can be done either by computing for each particle an interaction tensor with the contributions from all the particles outside the cut-off radius or by using the demagnetising field.

The tensor components that need to be taken into account for a particle j outside the cut-off radius of the considered i particle are:

$$\bar{\bar{T}}_{ij} = \frac{M_s V_j}{r_{ij}^3} \begin{pmatrix} 3r_x^2 - 1 \,, 3r_x r_y, & 3r_x r_z \\ 3r_y r_x, & 3r_y^2 - 1, & 3r_y r_z \\ 3r_z r_x, & 3r_z r_y, & 3r_z^2 - 1 \end{pmatrix} \tag{2.57}$$

with $\vec{r}_{ij} = r_{ij}\hat{r}_{ij} = r_{ij}(r_x, r_y, r_z)$ the relative position of particle j with respect to particle i. Multiplying the tensor formed by adding these components of all particles outside the cut-off radius with the orientation of the total magnetic moment of the system yields an approximation of the interaction field produced by all particles outside the cut-off radius.

The demagnetising field is the internal field produced by the magnetic moment of the sample and it depends on its shape and magnetisation state:

$$\vec{H}_{demag} = -\bar{\bar{N}} \cdot \vec{M} \tag{2.58}$$

with $\bar{\bar{N}}$ being the demagnetisation tensor of the sample and $\vec{M}$ the magnetic moment. For simplicity the demagnetised field is sometimes expressed as being the field produced by hypothetical "free poles" on the surface of the sample with a density given by the normal component of the polarisation. The demagnetisation tensor can only be calculated analytically for simple regular shapes while for more complicated samples a numerical approach is needed. For a finite sample the interaction field calculated with the interaction tensor (2.57) considered for all particles in the system includes the demagnetising field of the sample. In the case of "infinite" samples this approach fails because of the infinite number of tensors that need to be calculated. However even in this case using a sufficiently large cut-off radius for the tensor calculation should provide a sufficiently good

approximation of the interaction field including demagnetising effects. In the case of samples that are "infinite" in one or two dimensions this is due to the fact that the interaction field contributions decrease with distance by r^{-3} and r^{-2} laws respectively. For a sample that is "infinite" in all three dimensions, the demagnetising factor has the same constant value of $\frac{1}{3}$ regardless of the orientation of the sample magnetisation.

Chapter 3. Granular systems

3.1. Introduction

Granular media are obtained by film deposition and the information is stored on the ferromagnetic material crystals that are created during the deposition process. Typically, metal films are deposited in a multilayer process. The substrate is usually aluminium alloy with some sort of overcoat to increase surface hardness, reduce corrosion, and improve the adhesion of the metal film. This is followed by a thin coat of the magnetic material (typically 50-100 nm thick) and by a protective overcoat.

There are a number of film deposition techniques including plating [47] (the metal is deposited via chemical or electrochemical action in a solution), thermal evaporation [48] (the metal is heated in a vacuum and the film is deposited from the vapour), e-beam evaporation [49] (the metal is heated by an electron beam in a vacuum and the film is deposited from the vapour) and DC or RF sputtering [50] (a plasma is created in a vacuum chamber from some inert gas; interactions of the ionized gas with the target "knock" off atoms which are then deposited on the substrate; the plasma can be created with either a DC or ac-RF field). Although sputtering produces slightly lower quality films than evaporation due to damage produced by the high energy ions, sputtering remains the most economical and most popular way of depositing magnetic films.

A model of granular systems has to take into account its particularities as compared to other types of recording media. Among these are the facts that in granular media the particles are randomly placed, usually have a uniform 3D distribution of their easy axis orientations and exchange interparticle interactions can occur between "close enough" particles. For comparison, particulate media have a very narrow distribution of easy axis and no exchange interactions as will be shown in the next chapter.

3.2. Characteristics of the model

The model used for simulations of magnetic properties of granular systems is based on model described in [12] and [28] and it uses the techniques described in the previous chapter to find the magnetisation state of a sample taking interactions and thermal effects into consideration.

The sample model is made of a number of magnetic particles with uniaxial anisotropy having easy axes oriented randomly in 3D, a lognormal distribution of diameters and a lognormal or Gaussian distribution of anisotropy constants. These particles are randomly distributed into a computational cell with the shape of a parallelepiped with the constraint that particle overlaps are not allowed.

3.2.1. Distribution generation

To obtain a 3D random distribution of orientations, several techniques can be used all based on the ability to generate random numbers with a uniform distribution in the [0, 1] interval. The first technique, involves generating two such random numbers x and y and using the spherical coordinates angles $\theta = \arccos(2x-1)$ and $\phi = 2\pi y$ to define the orientation for the easy axis of each particle. For the second technique, triplets of random numbers (x, y, z) are generated for each particles until the vector $\vec{v} = (2x-1, 2y-1, 2z-1)$ has an absolute value less than or equal to 1. Then, the 3D random orientation is described by the unit vector $\vec{e} = \frac{\vec{v}}{|\vec{v}|}$. The average number of random number triplets needed for each particle is $6/\pi$ but even so this technique seems to be computationally faster than the first one because it only involves one call to a mathematical routine, namely *sqrt*, while the first one requires at least three mathematical routine calls (*sqrt*, sin and cos) when the orientation vector is expressed as $\vec{e} = \left(\sqrt{1-x^2}\cos\phi, \sqrt{1-x^2}\sin\phi, x\right)$.

A third method given in [51] involves generating doublets of random numbers (ζ_1, ζ_2) in the [0, 1] interval and computation of $\xi_1 = 1-2\zeta_1$ and $\xi_2 = 1-2\zeta_2$ until the quantity $\xi^2 = \xi_1^2 + \xi_2^2$ is smaller than 1. Then, the 3D random orientation is given by $\left(2\xi_1\sqrt{1-\xi^2}, 2\xi_2\sqrt{1-\xi^2}, 1-2\xi^2\right)$.

The lognormal distribution function in the general case is given by

$$f(x)=\frac{1}{\sqrt{2\pi}\sigma(x-\mu)}\exp\left(-\frac{\left(\ln\frac{x-\mu}{\theta}\right)^2}{2\sigma^2}\right) \tag{3.1}$$

where σ is the shape parameter, μ is the location parameter and θ is the scale parameter. In the model, the "standard lognormal distribution" was used, distribution that is obtained from the general case when $\mu=0$ and $\theta=1$. To generate random numbers with a standard lognormal distribution with a standard deviation σ the following algorithm [37] was used: doublets of random numbers (ζ_1,ζ_2) in the [0, 1] interval were generated and the values $\xi_1=1-2\zeta_1$ and $\xi_2=1-2\zeta_2$ were computed until the quantity $\xi^2=\xi_1^2+\xi_2^2$ was smaller than 1 and the values $l_1=\exp\left(\sigma\xi_1\sqrt{-2\frac{\ln\xi}{\xi}}\right)$ and $l_2=\exp\left(\sigma\xi_2\sqrt{-2\frac{\ln\xi}{\xi}}\right)$ have the required probability distribution function.

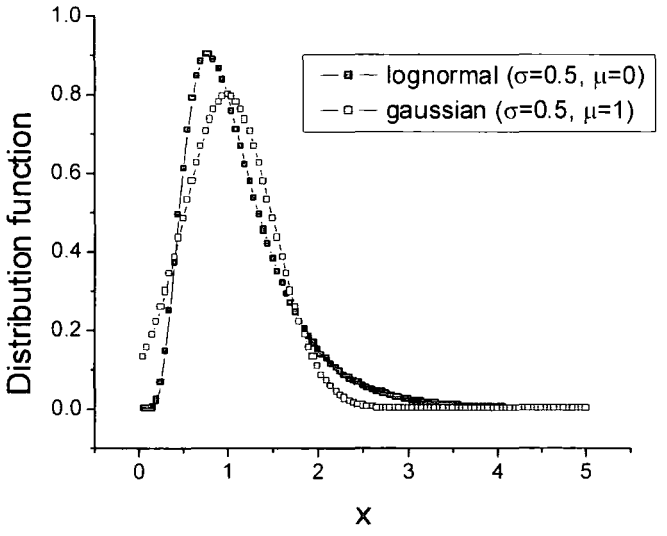

Figure 3-1. Gaussian and lognormal distribution functions

The Gaussian or normal distribution function in the general case is given by

$$f(x)=\frac{1}{\sqrt{2\pi}\sigma}\exp\left(-\frac{(x-\mu)^2}{2\sigma^2}\right) \tag{3.2}$$

where σ is the shape parameter and μ is the location parameter. Random numbers with for a Gaussian distribution with $\mu = 0$ were obtained using the following algorithm [37]: doublets of random numbers (ξ_1, ξ_2) were generated in the [0, 1] interval and the values $g_1 = \sigma\sqrt{-2\ln\xi_1}\cos(2\pi\xi_2)$ and $g_2 = \sigma\sqrt{-2\ln\xi_1}\sin(2\pi\xi_2)$ have the required distribution.

As shown in Figure 3-1 the lognormal distribution function goes to zero for $x \leq \mu = 0$ while the Gaussian distribution even centred on a 1 takes positive values for $x \leq 0$. This property makes the lognormal distribution the natural choice for parameters that can only take positive values such as particle diameters.

3.2.2. Periodic boundaries

Trying to directly simulate the behaviour of very large systems is almost impossible due to limited computational resources (both memory and CPU time). Even if for a moderately large system this would be possible, the same method would not work when trying to study the case of a sample that is infinite in one, two or even three directions (like an infinite wire sample, a thin film or bulk material). In order to overcome this inconvenience a smaller sample of parallelepipedic shape can be used and periodic copies of it used for interaction calculations in the desired infinite dimensions.

Figure 3-2 shows how periodic boundary conditions are used in one dimension. The base cell is shown in the centre of the image with its virtual copies to the left and to the right. Thus particle 1 has as a neighbour the virtual image of particle 2, 2" while particle 2 has as neighbour the virtual image of particle 1, 1'.

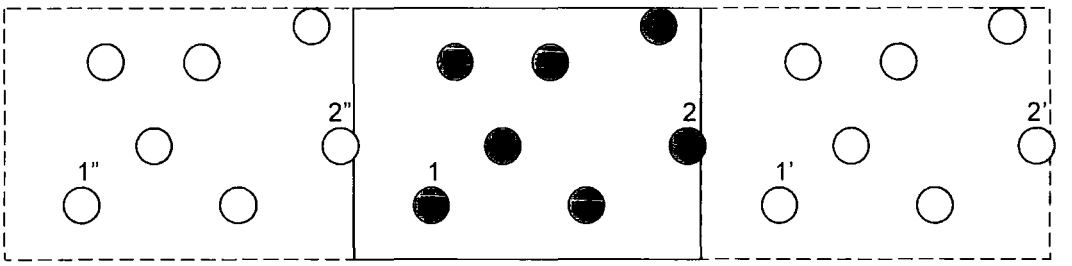

Figure 3-2. Periodic boundary condition in one dimension

In the model, the periodic boundary condition is used both when checking for particle overlaps in the algorithm for generating random particle positions and when calculating interaction fields, if required.

3.2.3. System configuration

The simulated sample, in the shape of a box, is made of spherical magnetic particles separated by non-magnetic material, in order to make the composition similar to that of granular recording media. The algorithm used for generating the configuration of the system requires as input the total number n of particles, the packing density ε representing the ratio between the volume of magnetic material and the total volume of the sample, the standard deviation σ of particle diameter and the aspect ratio (x_a, y_a, z_a) of the parallelepiped in which the particles are to be placed. The use of this aspect ratio as a parameter enables creation of samples with characteristics similar to those of bulk material, thin film, thin sheet or wire. At this stage, the average particle diameter is not actually needed as it is used as unit measure for all sizes in the model.

With these parameters known, n individual particle diameters are generated from a lognormal distribution with the deviation σ using the technique described in the previous paragraph and the total volume v_{mag} of the particles is calculated. Then, the actual size of the cell is calculated as $(x_c, y_c, z_c) = \sqrt[3]{\frac{v_{mag}}{\varepsilon x_a y_a z_a}}(x_a, y_a, z_a)$ to obtain the required packing density.

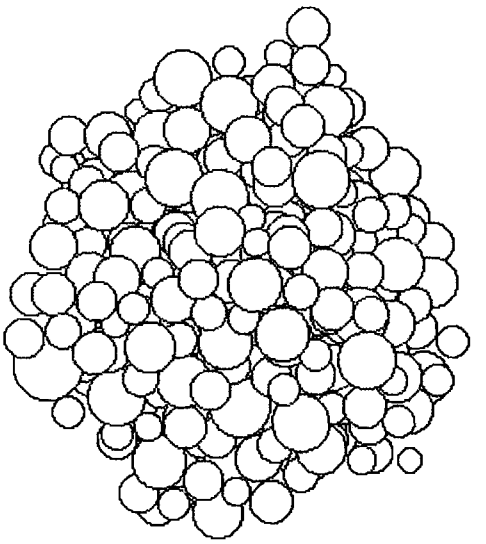

Figure 3-3. Cubic computational cell of 400 particles, 45% packing density and 0.2 standard deviation of diameter

For each particle i random 3D positions in the computation cell are generated as $(x_i, y_i, z_i) = (\xi_x x_c, \xi_y y_c, \xi_z z_c)$ with ξ_x, ξ_y and ξ_z uniformly distributed random numbers in the [0, 1] interval until, considering the periodic boundary condition in three dimensions, no overlap with any of the $1...i-1$ particles is detected. In order to improve the efficiency of this algorithm, the particles are ordered so that random positions for the larger particles are found first. Thus, packing densities up to 45% (see Figure 3-3) can be produced in reasonable time.

For each particle, a 3D random easy axis orientation is generated, a random value from a lognormal distribution of anisotropy fields is used to simulate the distribution of anisotropy constants and another 3D random easy axis is used as initial orientation of the magnetic moment.

3.3. Non-interacting systems

In order to test the validity of the model and the influence of the standard deviation of H_K simulations have been made without taking into account the interaction field between particles.

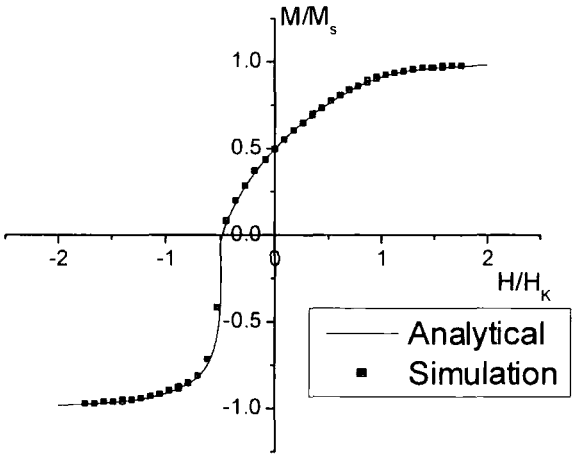

Figure 3-4. Analytical and simulated hysteresis loops of non-interacting Stoner-Wohlfarth particle systems

For a very large system of non-interacting Stoner-Wohlfarth particles with a random 3D distribution of easy axis, the hysteresis loop can be estimated as an integral of the magnetisation distribution function. Considering that the applied reduced field has the magnitude h then the total magnetisation of the system is given by:

$$m(h) = \frac{\int_0^{2\pi}\int_0^{\pi} m(h,\theta,\phi)\sin\theta\, d\theta\, d\phi}{\int_0^{2\pi}\int_0^{\pi}\sin\theta\, d\theta\, d\phi} = \frac{1}{2}\int_0^{\pi} m(h,\theta,\phi)\sin\theta\, d\theta \qquad (3.3)$$

where θ and ϕ represent the easy axis angles in spherical coordinates and the expression $m(h,\theta,\phi)$ is the magnetisation component in the direction of the applied field for a particle with the easy axis given by (θ,ϕ). Since an analytical solution for the Stoner-Wohlfarth equation (2.8) cannot be found the integral (3.3) cannot be directly evaluated. However, a numerical integration of the expression can be performed and the result of that has been compared with the results produced by the model for a system of 10000 non-interacting particles at 0K and with no distribution of anisotropy fields.

As shown in Figure 3-4 there is a very good agreement between two hysteresis loops. Furthermore, a similar comparison has been made between two widely used remanence measurements that are much more sensitive to the easy axis distribution: DC Demagnetisation (DCD) and Isothermal Remanent Magnetisation (IRM). The DCD curve is obtained by saturating the sample in one direction and then successively applying a field in the opposite direction, removing the field and plotting the remanent magnetisation against the value of the field. The field value for which the remanent magnetisation in the DCD curve becomes zero is referred to as remanent coercivity. The IRM curve is obtained by demagnetising the sample (in these simulations thermal demagnetisation has been used) applying a positive field, removing the field and plotting the remanent magnetisation against the value of the field. These remanent curves are a measure of the irreversible changes in the magnetisation configuration of a sample, changes that are intimately related to the easy axis distribution.

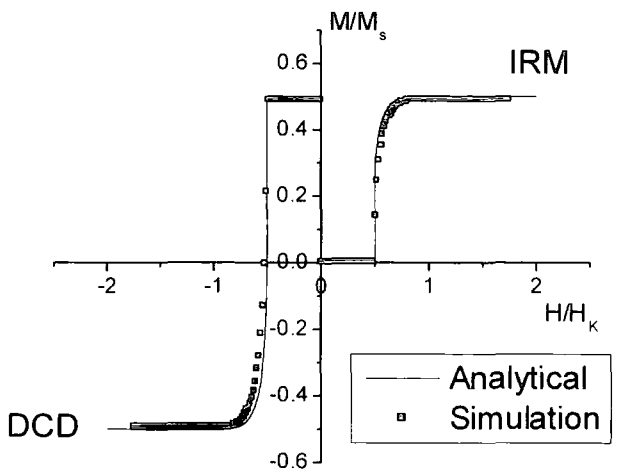

Figure 3-5. Analytical and simulated remanence curves of non-interacting Stoner-Wohlfarth particle systems

Again, a good agreement between the simulations and the analytical results is obtained as seen in Figure 3-5. This is a good validity test showing that the requirements made on the model are correctly implemented.

3.4. *Interaction effects at low temperature*

In order to vary the strength of interactions in the model, configurations with different packing densities in the range 0-40% were used. The following results have been produced using configurations of 5000 particles with a standard deviation of particle diameter of 0.1, the bulk saturation magnetisation of $1400 emu/cc$ corresponding to Cobalt, and anisotropy constants varied in the range $1\times10^{6} - 4\times10^{6}\ erg/cc$ the higher value also corresponding to the bulk Cobalt anisotropy constant. The standard deviation of H_K was also kept constant to a value of 0.1 and exchange interactions with an exchange constant $C^* = 0.3$ and exchange distance $d_{exch} = 0.2$ were also used for some of the simulations. Care must be taken when using the exchange distance in units of average particle diameter (in which all distances are expressed in the model) as when simulating properties of systems with large particles this may result in unrealistically large values for the exchange distance.

In all cases periodic boundary conditions were used in three dimensions to eliminate demagnetising effects and it has been found that a cut-off radius of 5 average diameters is sufficiently large to obtain full interaction effects.

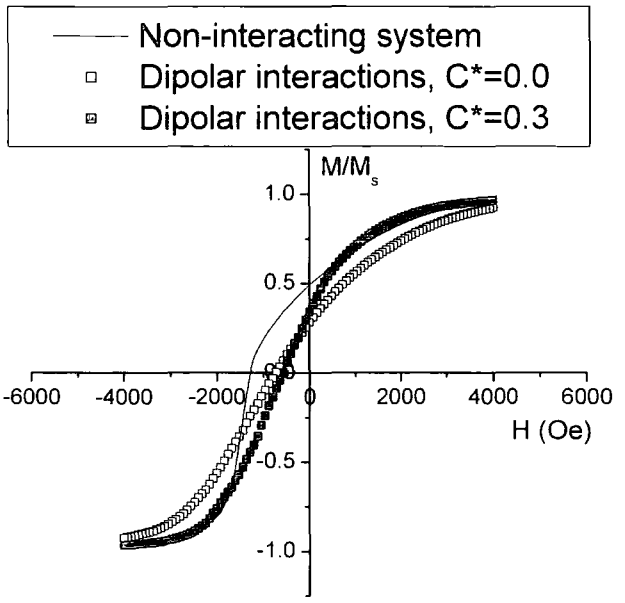

Figure 3-6. Interaction effects on the hysteresis loop of a 40% packing fraction system with anisotropy constant $K = 2 \times 10^6 erg/cc$

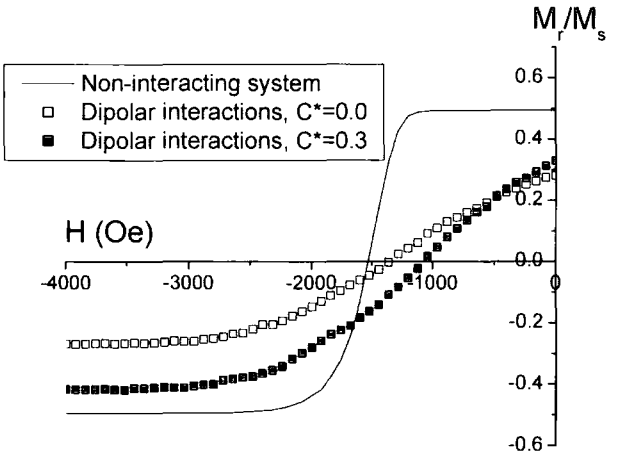

Figure 3-7. Interaction effects on the DCD curve of a 40% packing fraction system with anisotropy constant $K = 2 \times 10^6 erg/cc$

Figure 3-6 shows the effect of interactions on the shape of the hysteresis loop while Figure 3-7 shows similar effects on the DCD curves of the same system. A decrease of the remanence as compared to the non-interaction case is produced by the dipolar interactions

while the exchange coupling lead to an increase of the remanence value. However, both kinds of interactions produced a decrease of coercivity and remanent coercivity.

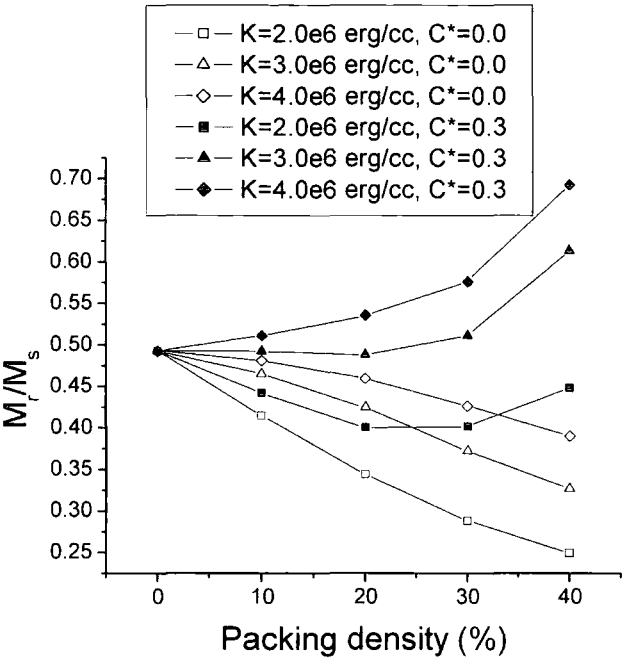

Figure 3-8. Remanence for low temperature systems with different packing densities as a function of anisotropy constant K and exchange parameter C*

A more systematic study of these effects has been conducted for three values of anisotropy constants and several values of packing density corresponding to various strengths of interactions.

Figure 3-8 introduces the effect of different anisotropy values on remanence. In the presence of exchange interactions and for a large anisotropy constant $K = 4 \times 10^6 emu/cc$ the remanence increases with concentration due to the increase in the energy barrier. For lower values of the anisotropy constant these calculations show an initial decrease of the remanence for low concentrations ($\varepsilon = 0.001, 0.1, 0.2$), followed by an increase in the remanence value for high packing fractions when exchange interactions are effective. This behaviour is due to the fact that for low concentrations, the particles are not close enough to experience exchange interactions, allowing the longer-range magnetostatic interactions to dominate; at higher concentrations, the exchange interaction acts to keep the magnetic moments of the particles aligned to reduce the exchange energy.

For the case of zero exchange-coupling, the remanence decreases monotonically with packing density for all values of K. This is in contrast to 2D simulations [52] and indicates the presence of strong demagnetizing interaction fields. It might be expected that the presence of competing dipolar and exchange interactions would have some effects of frustration on the magnetic properties. This is apparent in the minimum in the remanence predicted in Figure 3-8 for $K = 2 \times 10^6 erg/cc$: at low density the average particle separation is too large in relation to the cut-off of the exchange field to have an appreciable effect: hence, the low-density behaviour is dominated by the dipolar interactions. At higher densities the exchange begins to dominate, leading to a predicted increase in remanence. For larger values of K the minimum vanishes and a monotonic increase of M_r with packing density is seen. This is because, first, the large anisotropy mitigates against the formation of closed loop structures, leading to a relatively slow decrease in remanence. Second, it should be noted that in the calculations here the magnitude of the exchange field scales with H_K; thus, the magnitude of the exchange field relative to the dipolar interactions is larger for large K.

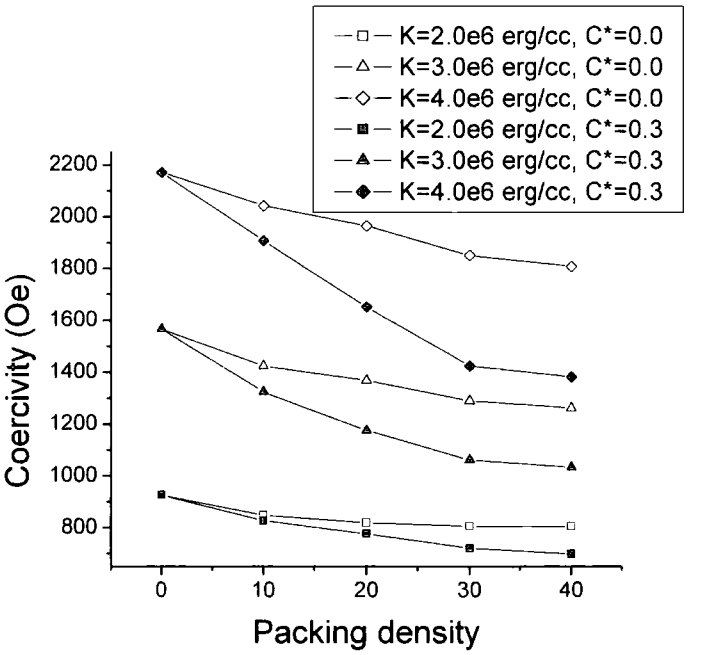

Figure 3-9. Coercivity for low temperature systems with different packing densities as a function of anisotropy constant K and exchange parameter C*

Figure 3-9 shows the decrease of the coercivity with the packing fraction. For the case of dipolar interactions only, this decrease arises because the dipolar interactions favour the demagnetized state [11]. Addition of exchange coupling produces a more rapid decline in the coercivity with concentration, due to the onset of collective magnetization reversal [10]. In 2D simulations such as those given in [10], exchange results in a large degree of correlation. In our case the correlation lengths are relatively small, due to the low packing density and the spatial disorder. However, there remains a strong tendency for the formation of flux closure configurations under the influence of the magnetostatic interactions, leading to a short-ranged order. The exchange interactions give an enhancement of the remanence. However, the predicted hysteresis loops are significantly less square than the 2D case for similar parameters, suggesting that collective reversal is less important. This can be ascribed to the spatial disorder which will naturally limit the correlation length, as will be discussed later.

3.5. *Interaction effects at high temperature*

When the Kv/k_BT ratio becomes very small a non-interacting particle system will show superparamagnetic behaviour with zero remanence and coercivity. Hysteresis loops for systems with interactions are shown in Figure 3-10 and the results show an enhancement in both remanence and coercivity.

The systematic study of interaction effects on remanence for large thermal effects shown in Figure 3-11 was obtained for systems with average diameter of 6nm at 300K values for each a particle is superparamagnetic in the absence of interactions. For these systems unlike those in Figure 3-8, the remanence increases for both cases of dipolar only and dipolar and exchange interactions. For the case of dipolar interactions only, at small concentrations the particles do not experience any interactions and the remanence is zero, as expected for superparamagnetic particles. When the concentration increases, the particles start to experience the magnetic interactions of the surrounding particles.

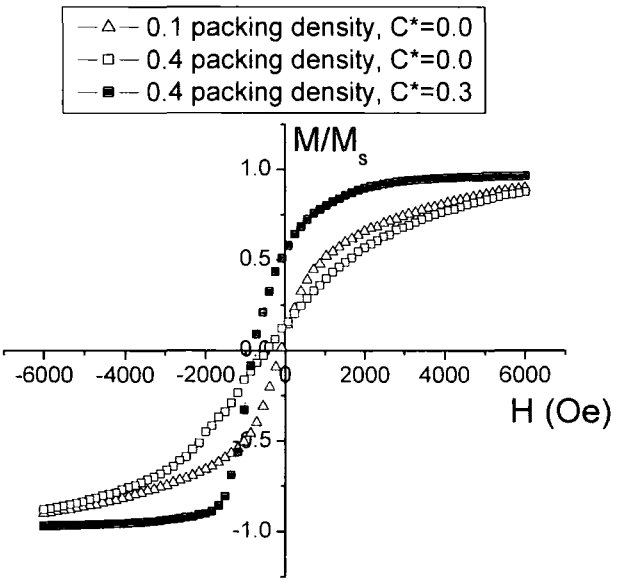

Figure 3-10. Interaction effects for systems with average particle diameter of 6nm, anisotropy constant of 4.0e6 erg/cc and temperature of 300K

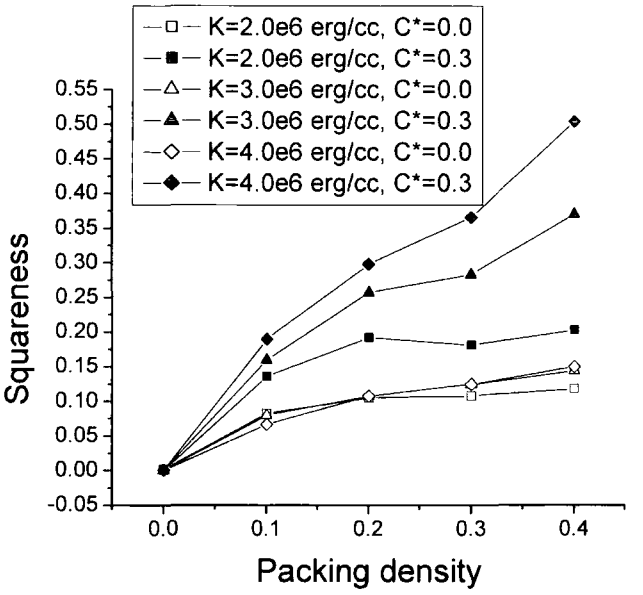

Figure 3-11. Remanence for high temperature systems with different packing densities as a function of anisotropy constant K and exchange parameter C*

The Allia et. al. model [23], using a mean-field scheme with a memory term in the argument of the Langevin function to characterise weakly dipolar interactions in superparamagnetic particle systems finds a similar increase of the hysteretic behaviour of

these systems showing an interaction induced increase in the energy barrier of the particles, results that compare well to experimental measurements presented there. A similar study by Dormann et al. [17], [18], [19] characterising superparamagnetic systems with weakly and medium interactions shows the additional energy barrier due to dipolar interactions. Because of this, some of the SPM particles become blocked, leading to an increase in remanence. Consequently the results predicted here are in this sense supportive of these models.

At the same time, the Morup et. al. model [22], [20], [21] for weakly interacting systems predicts a decrease of the energy barrier with interaction strength, results that fitted a set of experimental data that is singular in the literature. The results presented here as well as those in [17], [18], [19], [23] are in contradiction with these findings pointing to the fact that the Morup et. al. model can only be valid for specific microscopic configurations that favour this energy barrier decrease.

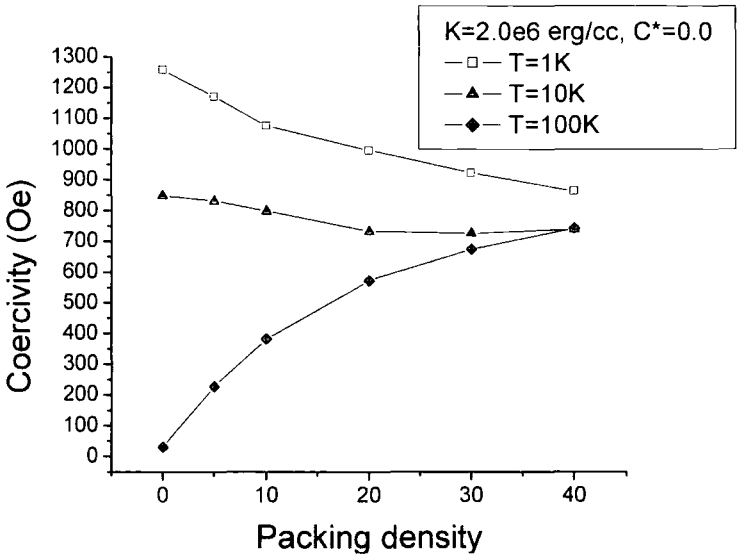

Figure 3-12. Coercivity as a function of packing fraction showing three regimes of behaviour dependent on KV/k_BT

To see the effects of the temperature in a system with dipolar interactions only, the coercivity as a function of concentration for different temperatures was plotted in Figure 3-12. For low temperatures the coercivity decreases with concentration. Even when the particles are very small, if the temperature is low enough, almost all the particles are blocked. In this case the expected behaviour is similar to that of Figure 3-9 in which the

coercivity decreases with concentration. If the temperature is increased to 100 K, all the particles become SPM and the coercivity increases with packing fraction.

For small concentrations, the particles do not interact and the behaviour is purely superparamagnetic with zero coercivity. As the particles become closer, the dipolar interactions start to be important and block the moments, generating coercivity. At an intermediate temperature of 10 K the coercivity is constant with packing fraction.

The variation of the coercivity for different concentrations is plotted in Figure 3-13 for small particles and a small value of the anisotropy constant. These data exhibit a maximum which can be ascribed to the competition of two different processes. At low concentrations the particles are superparamagnetic, but with the increase of the concentration and thereby of the dipolar interaction, the particle moments begin to block. Continuing to increase the concentration, interactions become more important, and leading to longer-range correlations, specifically, the magnetostatic interaction produces flux closure loops which decrease the coercivity as can be seen for the case of blocked particles. Clearly, the effects of interactions on the properties of granular systems are highly complex. The model of Dormann et al. [19] predicts a monotonic increase of energy barrier with interaction strength. However, Figure 3-12 and Figure 3-13 indicate that the model of Dormann et al. cannot be applied under all circumstances, since it would be expected to lead to an increase of H_c with interaction strength. It can be seen that an increase in H_c with interaction strength is only reserved for weakly interacting systems having small values of KV/k_BT, in which the energy barriers arise principally from interactions. The maximum observed in Figure 3-13 suggests that the transitions to an ordered state, leading generally to a reduced coercivity, cannot be neglected in practice. Kechrakos and Trohidou [11] have also observed a similar peak in the coercivity as a function of concentration for a system with zero anisotropy. The results presented here demonstrate that the important factor is KV/k_BT. In order to observe the peak experimentally it is necessary to study a system with KV/k_BT small enough to be predominantly superparamagnetic, but of sufficiently large moment so that the magnetostatic interactions are strong at high densities.

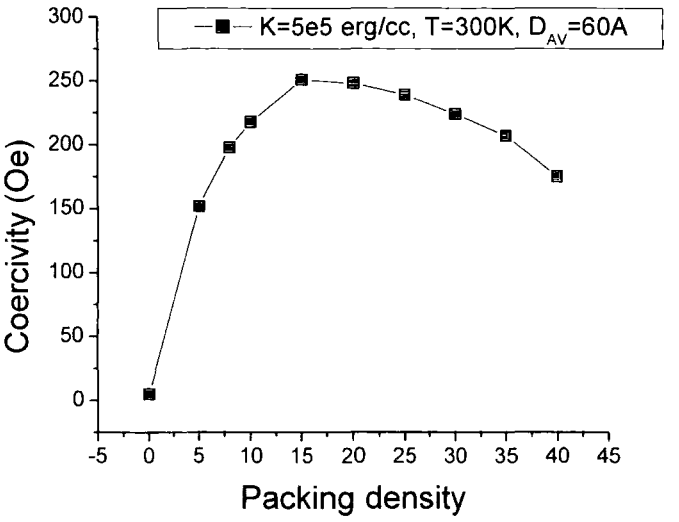

Figure 3-13. Coercivity as a function of packing fraction for systems with low KV/k_BT

Evidence for the existence of correlations can be obtained by investigating a correlation function of the form

$$\xi = \langle \vec{\mu}_1 \cdot \vec{\mu}_2 \rangle \tag{3.4}$$

ξ is clearly dependent on the position relative to the particle under consideration. Here ξ is determined in a coordinate system based on the magnetization direction of the particle under consideration. By this means ξ becomes sensitive to local anisotropies in the magnetic microstructure which would be averaged out in the global coordinate system.

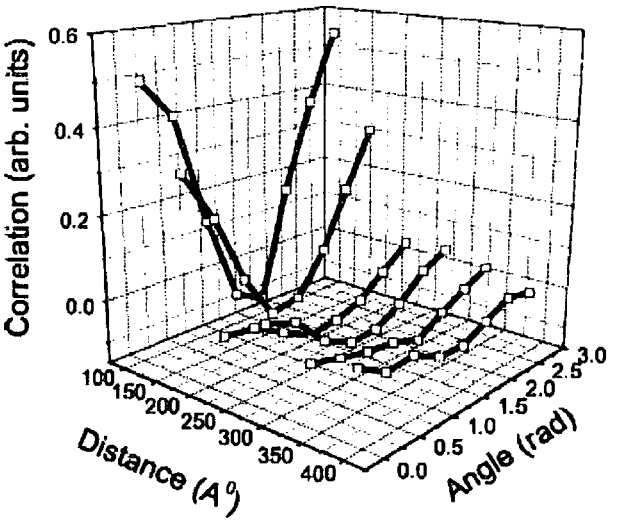

Figure 3-14. Radial and angular dependence of the correlation function for a system with magnetostatic interactions only

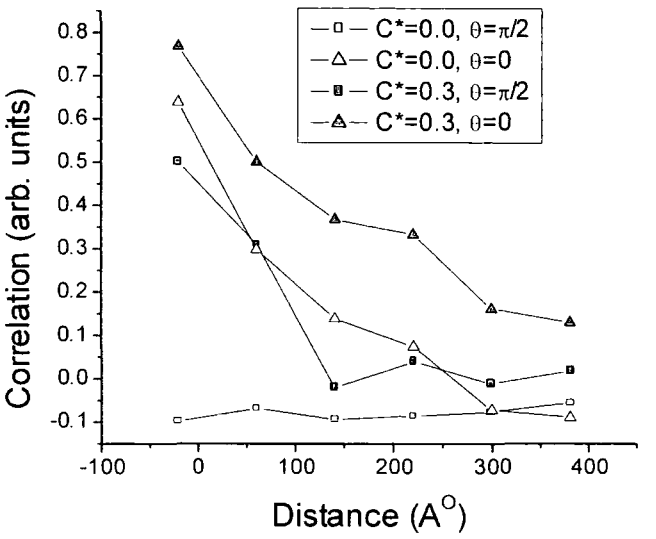

Figure 3-15. Radial dependence of the correlation function for orientations parallel and perpendicular to the local magnetization.

Figure 3-15 gives the radial and angular dependence of the correlation function for a system with magnetostatic interactions only, for $K = 2 \times 10^6 erg/cc$, $T = 4K$, and a packing fraction of 0.4. It can be seen that the system is strongly correlated with a correlation length of a few particle diameters. Equally important is the form of the correlation function, which is consistent with the existence of flux closure configurations. Specifically, we note the strong angular dependence of ξ for small separations. The strong correlations occur along the local magnetization direction, with smaller, negative, values at an orientation perpendicular to this direction, as would be expected for magnetostatically induced clusters. The correlation function for a system with the same parameters, but now including strong exchange coupling, does not show the anisotropy evident in Figure 3-14. This is a result of the exchange coupling which leads to short-ranged ferromagnetic order. The difference in the form of local order between the two cases is demonstrated in Figure 3-15, which shows the radial dependence of the correlation function for orientations parallel ($\theta = 0$) and perpendicular ($\theta = \pi/2$) to the local magnetization. In the case of the magnetostatically coupled system the angular dependence is dramatic, with strong positive correlation parallel to the magnetization direction and a weaker, negative value perpendicular, which is to be expected given the form of the dipolar magnetostatic interaction. The behaviour of the exchange-coupled system shows stronger correlations and

the isotropic form of the correlation function is again consistent with the form of the exchange interaction. The magnetostatically coupled system shows a rapid decrease in ξ with distance for $\theta = 0$, which indicates that the order in this case is either in the form of correlated particle pairs or that the flux closure structures have a small radius. The variation for $\theta = \pi/2$ is less pronounced and indicates negative correlations out to several particle diameters, which is consistent with the formation of clusters or, in the case of particle pair formation, is indicative that the pairs order antiparallel under the influence of the magnetostatic interaction. As mentioned previously, the correlation length, at around two particle diameters, is rather small, which presumably reflects the disordered physical microstructure. These results are consistent with the experimental data shown in [53]. Here measurements of the parameter $\Delta M(H)$, derived from a comparison of the principal remanence curves, demonstrate a change from predominantly magnetostatic interactions to ferromagnetic exchange interactions with enhanced remanence as the exchange between grains is increased by annealing.

Clearly, there is strong evidence for short-ranged correlations in the system, whose form depends on the strength and form of the intergranular interactions. These correlations have a direct bearing on the magnetic properties which are discussed in 3.9.

3.6. Switching field distributions

The effects of interactions on the energy barrier distribution are evident in the switching field distribution (SFD), which is a measure of irreversible magnetization changes. Here the SFD is calculated as the differential with respect to the field of the DCD curve previously described.

Figure 3-16 shows the SFD, considering only dipolar interactions for an anisotropy constant of $K = 2 \times 10^2 erg/cc$. For the noninteracting case, it can be seen that almost all the particles start to rotate at the same field with a small distribution due to the distribution of particle sizes. The smaller particles rotate earlier due to the lower-energy barrier, which is proportional to Kv. As the packing density is increased, the dipolar interactions spread out the SFD and the shape of the curve becomes more asymmetric. From comparing Figure 3-8 and Figure 3-16 it can be seen that the dipolar interactions favour the demagnetized

state, but make the rotation of the particles towards negative saturation more difficult. This is consistent with the formation of flux closure structures. The model of Dormann et al. [19] gives rise to a net increase in the mean energy barrier evidenced by the shift in the peak to larger negative fields. Clearly, the change in width of the energy-barrier distribution implied by the increased width of the SFD is also an important factor and is not predicted by the model of Dormann et al. Essentially, the model of Dormann et al. uses an averaging technique to determine the change of mean energy barrier and ignores the fluctuations in the local environment of each particle. The increase in width of the SFD arises from the local fluctuations, which are clearly an important aspect of the physical description of the problem.

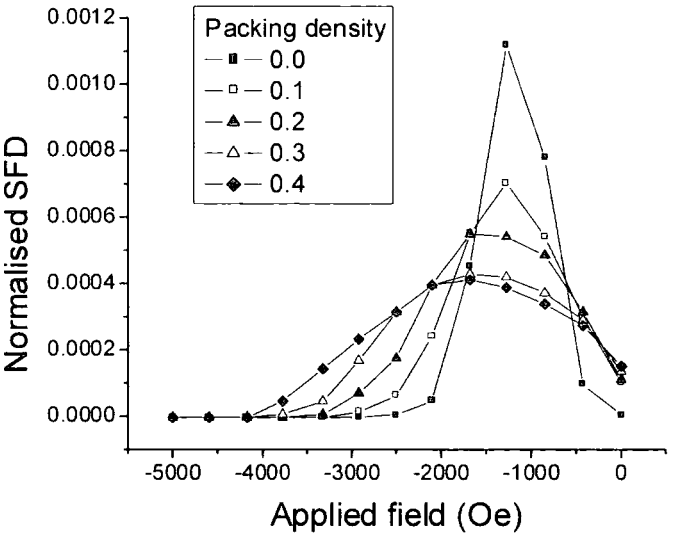

Figure 3-16. Normalised SFD for systems with K=2.0e6 erg/cc at low temperature with dipolar interactions only

A significant variation in the SFD has been noticed when the value of the anisotropy constant has been increased. Figure 3-17 shows the SFD for the case with no exchange interactions for an anisotropy constant value of $K = 4 \times 10^2 erg/cc$. The high-anisotropy constant resists the formation of flux closure loops, preventing the rapid demagnetizing seen in Figure 3-16 for the case without exchange interactions. This results in a more symmetric and broader SFD whose peak position is shifted to higher fields due to the higher anisotropy. It is interesting to note that the SFD has become very broad and flat in this case. This is indicative of a very wide dispersion of energy barriers, perhaps

resulting from the appearance of a large number of shallow local minima resulting from the competition between the anisotropy and the magnetostatic energy. The magnetization reversal then proceeds via a number of intermediate states defined by these minima.

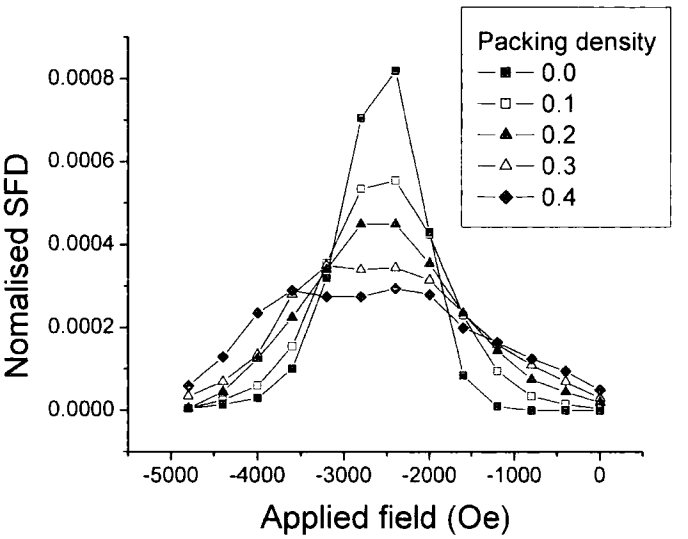

Figure 3-17. Normalised SFD for systems with K=4.0e6 erg/cc at low temperature with dipolar interactions only

These results are consistent with previous work on the initial susceptibility of interacting fine particle systems [54] which showed that at high density the variation of susceptibility with temperature becomes very flat, again indicative of a very wide energy barrier distribution. Calculations of the time dependence of the magnetization that are shown in the next subchapter are also consistent with the existence of an energy surface with many local minima.

For the case of low anisotropy, in the presence of exchange as shown in Figure 3-18 there is remanence enhancement due to exchange. However, the SFD in small negative fields is not significantly different from the case of magnetostatic coupling only. This is not consistent with the expected effect of exchange being to stabilize the magnetized state. The low anisotropy cannot stabilize the remanent state and the tendency to flux closure due to the magnetostatic interactions is the most significant factor as the field is made more negative.

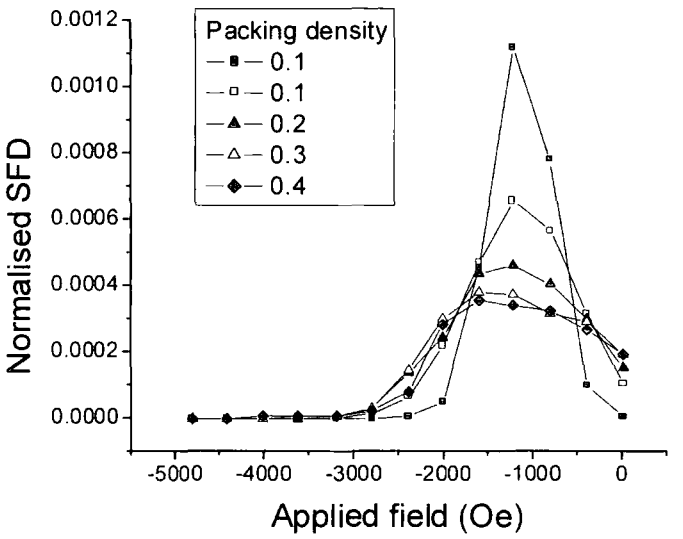

Figure 3-18. Normalised SFD for systems with K=2.0e6 erg/cc at low temperature with dipolar and exchange interactions

The low-anisotropy case exhibits less cooperative reversal as evidenced by the long tail in the SFD in large fields. This suggests that coupling has a dramatic effect on the dynamic behaviour of the system, the frustration arising from competition between the dipolar and exchange interactions. This same competition results in the dip observed in the remanence as a function of packing fraction for the same value of anisotropy constant shown in Figure 3-8.

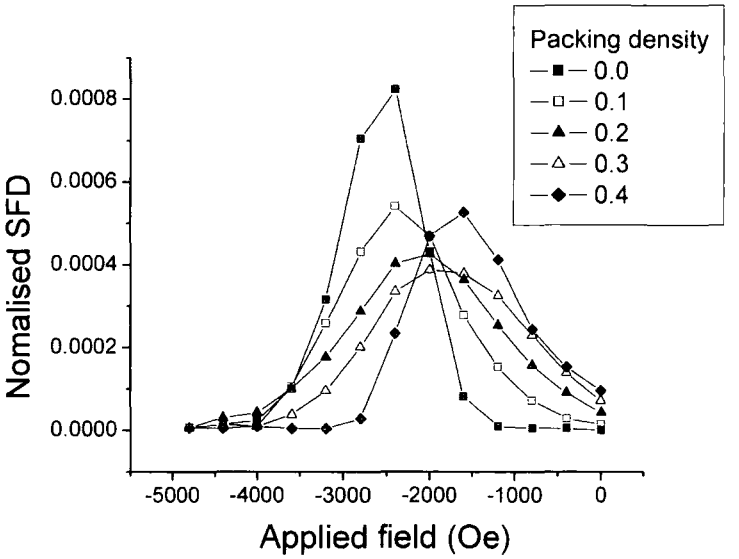

Figure 3-19. Normalised SFD for systems with K=4.0e6 erg/cc at low temperature with dipolar and exchange interactions

Figure 3-19 shows the same system with strong exchange coupling, but this time with the higher-anisotropy constant of $K = 4 \times 10^2 erg/cc$. Once again, for small concentrations the dipolar interactions dominate, but when the packing density is increased the cooperative effects due to the exchange interaction become significant and the remanence coercivity decreases. In negative fields, particles of smaller size and anisotropy start to rotate first, with strong coupling to other particles producing cooperative demagnetization. The effect is more pronounced for the case of strong dipolar and exchange interactions. The SFD also becomes wider, due to the dispersion in the local field when the packing density is increased. As the concentration is increased, the exchange becomes more important, and thereafter the increase of SFD in small fields is less pronounced. The exchange energy tends to maintain the alignment of the moments; this leads to a large gradient of the SFD in large fields, as once the field overcomes the energy barrier, cooperative rotation occurs.

3.7. *Magnetic viscosity effects*

Magnetic recording media are used to store information for long periods of time, typically years, therefore the need for stable storage media so that information can be accurately read when necessary. The need for high densities requires that written bits become smaller, susceptible to thermal fluctuations that can affect the quality of the record. In ferromagnetic materials, in general, the value of the magnetization is time dependent. This dependence generally increases with temperature and decreases with particle size. To characterize the time dependence of magnetization, the "magnetic viscosity", $S = \frac{dM}{d(\ln(t))}$ is used [55].

Since the transition probability (2.45) explicitly includes the measuring time, the described model can also be used to predict magnetic viscosity behaviour of such systems in various conditions. To estimate the viscosity coefficient, the system is saturated with a high magnetic field. Then, the saturation field is removed and an opposite magnetic field, H, is applied. The magnetization of the sample is measured after different periods of time, and the viscosity is calculated as the slope of M vs. $\ln(t)$ curve. Figure 3-20 shows such a

time dependence of magnetisation for a non-interacting system of particles at $T = 100K$. The other parameters used had the following constant values: anisotropy constant $K = 2 \times 10^6 erg/cc$, saturation magnetisation $M_S = 1400 emu/cc$, average particle diameter $d_{av} = 6nm$, exchange distance $d_{exch} = 0.2$ and exchange coupling constant, when indicated, $C^* = 0.2$.

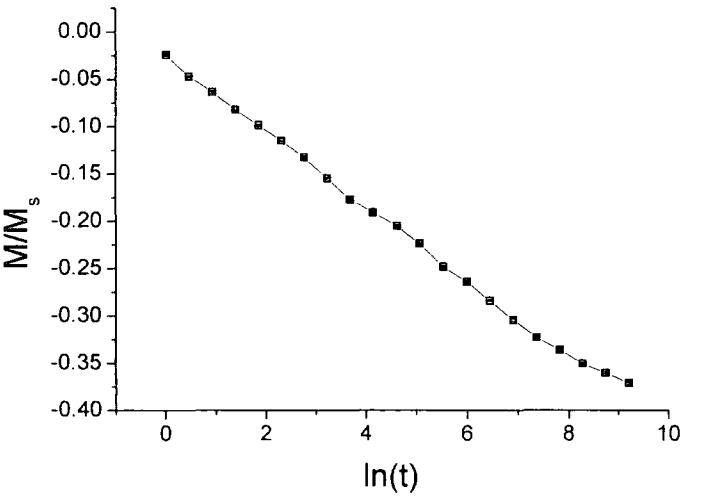

Figure 3-20. Variation of magnetisation with time for a non-interactive system at coercivity

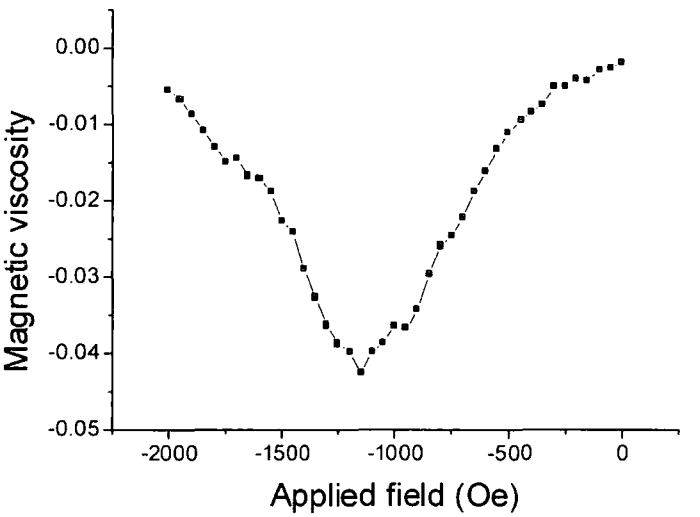

Figure 3-21. Viscosity dependence of the applied field for a non-interacting system at 100K

Conventionally the magnetic viscosity is represented as a function of the applied field H and Figure 3-21 shows the curve obtained for a system of non-interacting particles.

As expected and in agreement with previous work [56], the magnetic viscosity exhibits a maximum (in absolute value) around coercivity. This is because around the coercivity the maximum number of particles have energy barriers close to the critical energy barrier.

Figure 3-22 shows shows the variation of viscosity with packing fraction for systems at 300 K while Figure 3-23 shows the variation of coercivity for the same systems.

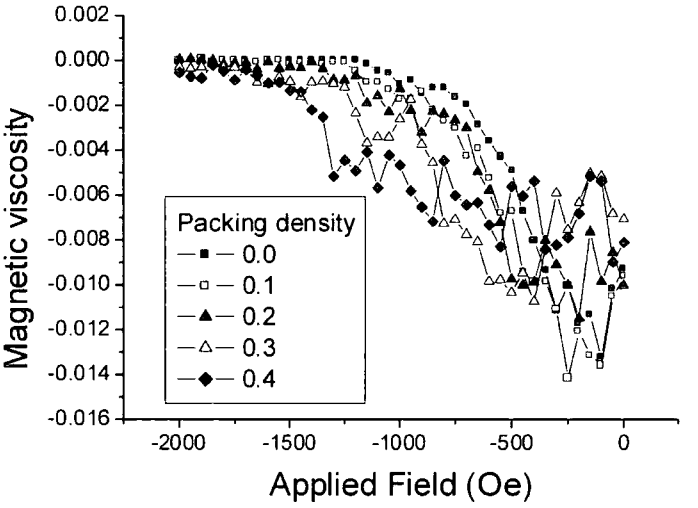

Figure 3-22. Influence of packing density on the magnetic viscosity curves for systems at 300K

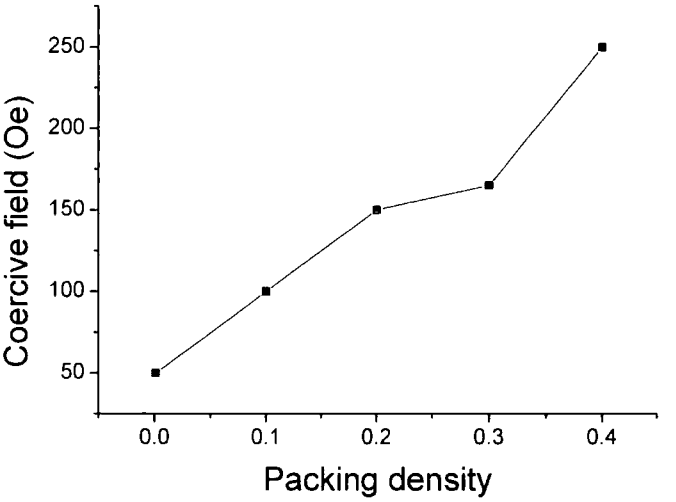

Figure 3-23. Variation of the coercive field with packing density for systems at 300K

These results are for systems with dipolar interactions only and the KV/k_BT value is low enough so that for the system with low packing density most of the particles are superparamagnetic. In the high-density systems, interactions lead to an increase in the energy barrier so that some of the particles become stable, consistent with the results presented in the previous sub-chapter.

Another effect of magnetostatic interactions is the decrease in the viscosity, as well as broadening the curve. This is also true for systems at low temperatures (20K) where all particles are blocked (Figure 3-24).

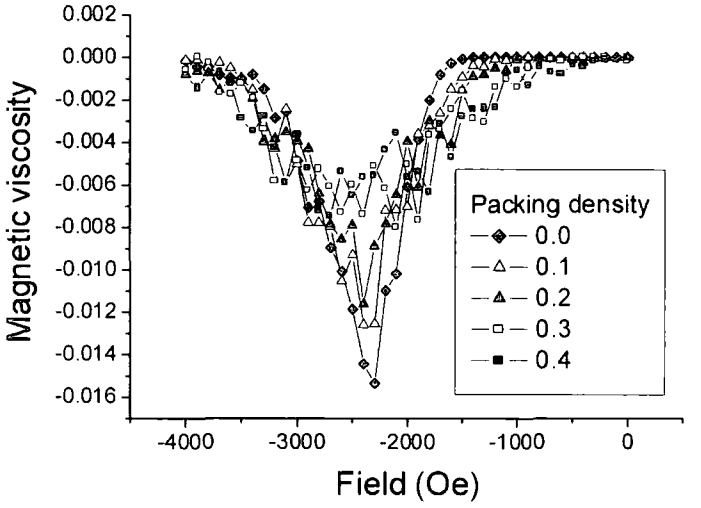

Figure 3-24. Variation of the coercive field with packing density for systems at 20K

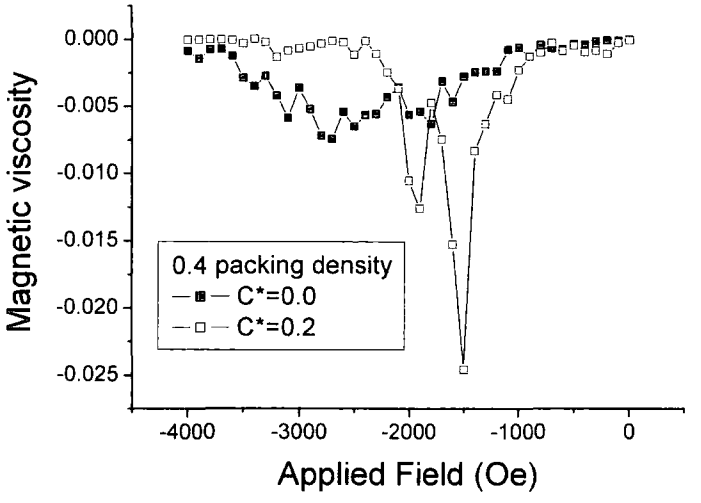

Figure 3-25. Effect of exchange coupling interactions on magnetic viscosity

However, the exchange interactions, which occur mostly in high-density systems, produce a different behaviour. Figure 3-25 shows that exchange coupling produces a substantial increase in viscosity at coercivity while it reduces its value at other fields.

This is consistent with the fact that for such systems, the slope of the hysteresis loop is quite high in this region, due to the formation of "domains" of particles that switch simultaneously. For the relaxation mechanism a similar behaviour is present, in the sense that the whole cluster will relax at once, producing big variations in the magnetic moment, i.e. high values for the magnetic viscosity.

Although the values for the maximum magnetic viscosity are about the same for superparamagnetic and blocked particles, there is a thermal dependence of this. Figure 3-26 shows that, for an intermediate temperature of 100K, at the limit between blocked and superparamagnetic behaviour for most of the particles, the viscosity dramatically increases.

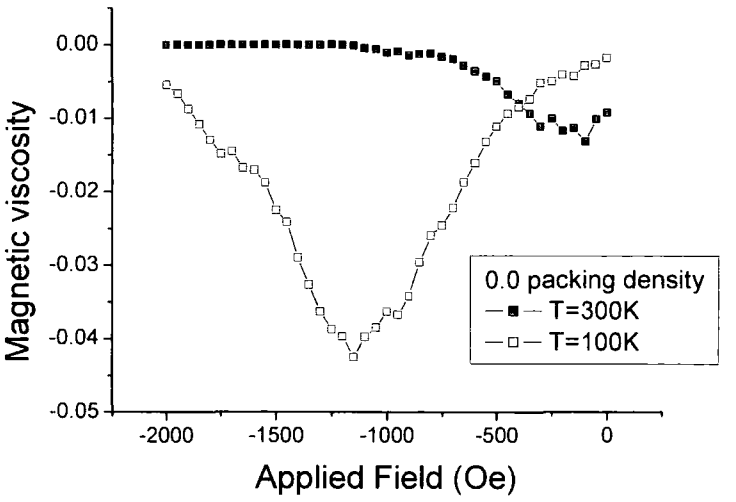

Figure 3-26. Increase of viscosity at an intermediate temperature of 100K

3.8. *Activation volume*

The activation volume is a critical parameter in the characterisation of high density recording media since it determines the smallest unit of magnetic material that can be reversed in a single step and hence defines the minimum bit size. A direct measurement of this parameter is very difficult and thus several indirect methods that allow an estimation of the activation volume have been developed. These methods rely on the concept of

fluctuation field that was first suggested by Néel [57] who showed that a fluctuating magnetic field is a useful analogy to the effect of thermal energy on the magnetic moment of a sample. The moment is coupled to the thermal energy through the magnetisation vector which is acted upon by the fluctuating magnetic field. Subsequently Wohlfarth [58] pointed out that the fluctuation field gave rise to an activation volume of reversal, indicating the fraction of material which reversed coherently in a single step. In granular systems the activation volume can be either larger or smaller than the average grain size, depending on the reversal mechanism and the type of interactions present in the system. In particular, when the grain size is larger than the critical single-domain particle size incoherent reversal occurs leading to activation volumes smaller than the physical particle volume. On the other hand, in the case of thin film media intergranular exchange coupling gives rise to an activation volume that is larger than the grain size itself.

For the case where the time dependence of the magnetisation of a material is measured around coercivity and varies linear with $\ln t$ the fluctuation field is given by [57]:

$$H_f(H) = \frac{S(H)}{\chi_{irr}(H)} \tag{3.5}$$

where S is the magnetic viscosity previously described and χ_{irr} is the magnetic irreversible susceptibility determined by differentiation of the DCD magnetisation curve.

The activation volume can then be deduced from the equation [58]:

$$H_f = \frac{k_B T}{v_{act} M_S} \tag{3.6}$$

with M_S the saturation magnetisation of the bulk material.

If the magnetisation decay is not linear with $\ln t$ a different technique based upon a waiting time approach is used. For two different fields H_1 and H_2 the times t_1 and t_2 required for the magnetisation to decay to a constant value are measured and the fluctuation field is calculated as [59]

$$H_f(H) = \left| \frac{H_2 - H_1}{\ln(t_2 / t_1)} \right|_M \tag{3.7}$$

and the activation volume is again deduced from (3.6). This method can be used either to obtain a constant value of the in-field magnetisation or to obtain a constant value of the

remanent magnetisation (known as corrected waiting time). Both approaches have been tested with the model and the results compared with the results yielded by the S/χ_{irr} method and with experimental results obtained by Antel et al [29].

The simulation parameters chosen for the simulations were $M_s = 1.4\times10^3 emu/cc$, and $K = 2\times10^6 erg/cc$, $D_{av} = 10nm$ and a temperature of $300K$. Both the standard deviation of particle diameter and the standard deviation of anisotropy fields have been varied and no interparticle interactions were considered in the fluctuation field calculations.

The initial results were obtained for a system of perfectly aligned particles for which the in-field and remanent magnetisation is identical and they show consistency between the waiting time method and the S/χ_{irr} method for non-zero values of at least one of the standard deviation parameters, σ_d and σ_K. In the case when both these values are zero, the irreversible susceptibility is infinite for at coercivity and thus the S/χ_{irr} method fails (see Figure 3-27) while the waiting time method still produces reasonable results (Figure 3-28).

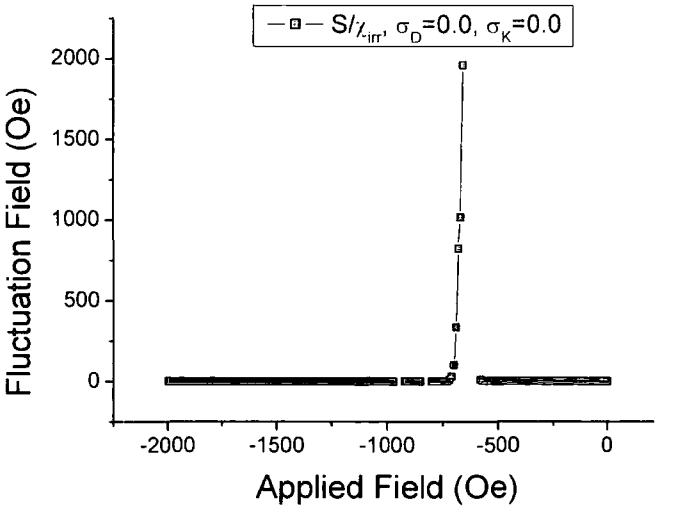

Figure 3-27. Failure of the S/χ_{irr} method to find the fluctuation field on a system of identical perfectly aligned particles

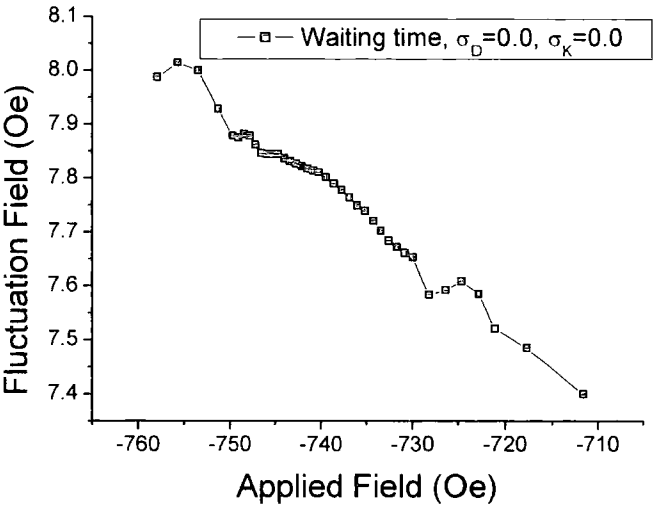

Figure 3-28. Fluctuation field obtained by waiting time method on a system of identical perfectly aligned particles

Figure 3-29 and Figure 3-30 show a good agreement between the two methods when there is a distribution of particle diameters but no distribution of anisotropy fields.

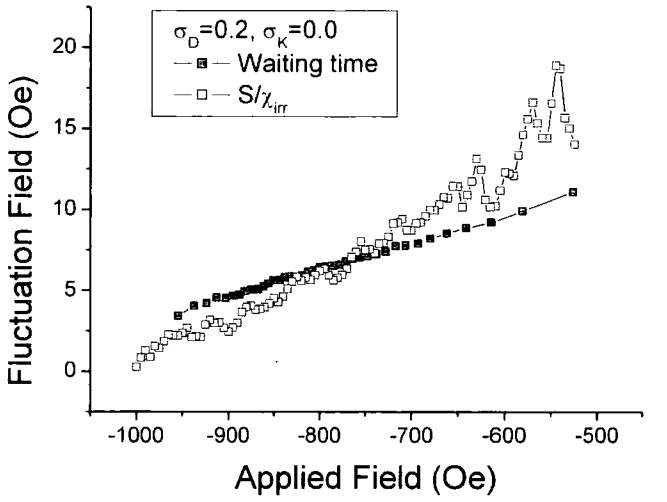

Figure 3-29. Fluctuation field for an aligned particle system with 0.2 standard deviation of size distribution

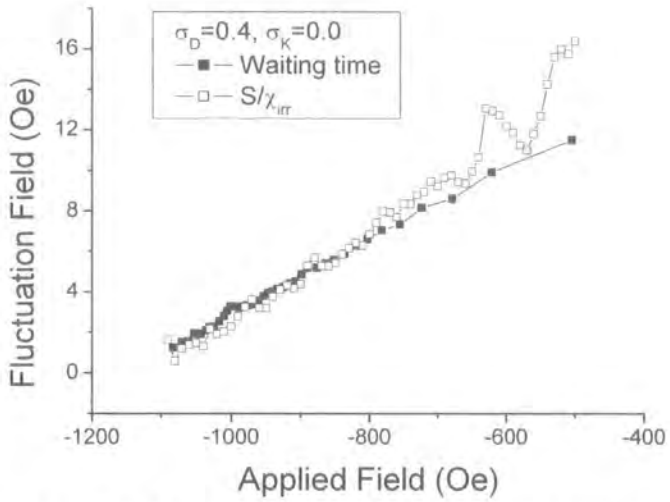

Figure 3-30. Fluctuation field for an aligned particle system with 0.4 standard deviation of size distribution

Figure 3-31 shows the variation of the fluctuation field when there is no particle size dispersion but there is an anisotropy one while Figure 3-32 and Figure 3-33 show the same variation when there is both a size and anisotropy distribution. Again there is a good agreement between the two methods of calculating the fluctuation field.

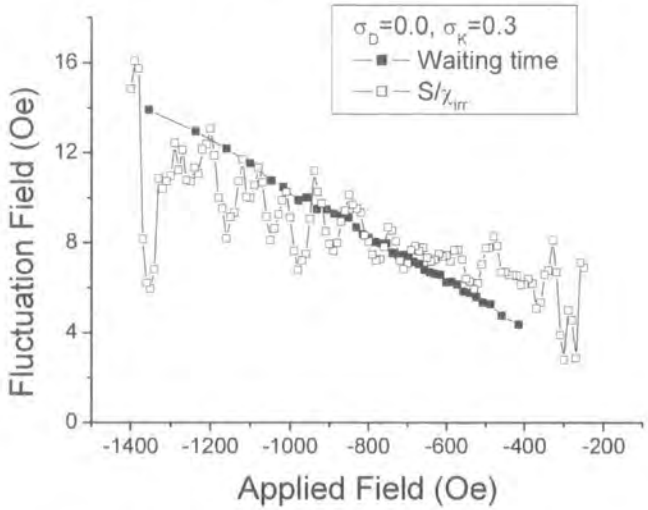

Figure 3-31. Fluctuation field for an aligned particle system with 0.3 standard deviation of anisotropy distribution

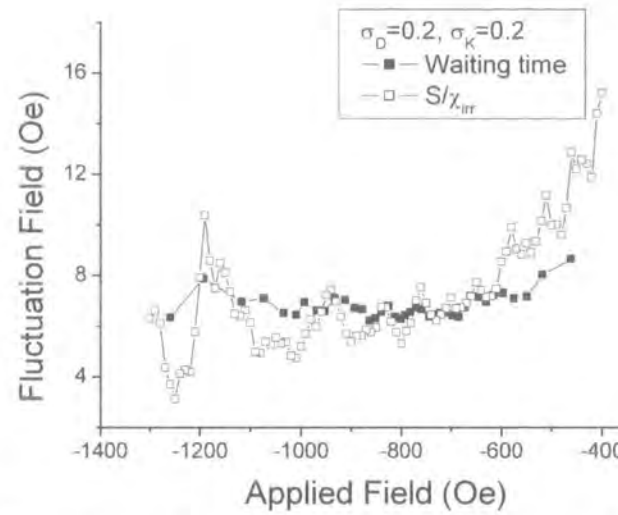

Figure 3-32. Fluctuation field for an aligned particle system with 0.2 standard deviation of size distribution and 0.2 standard deviation of anisotropy distribution

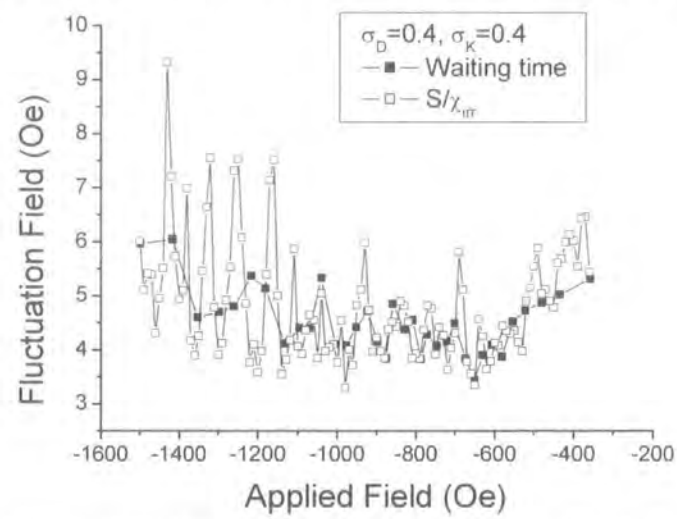

Figure 3-33. Fluctuation field for an aligned particle system with 0.4 standard deviation of size distribution and 0.4 standard deviation of anisotropy distribution

In most cases the fluctuation field obtained was in the range $4-20Oe$, corresponding to activation volumes between $1.4\times10^{-18}cc$ and $7\times10^{-18}cc$, i.e. activation "diameter" between $10nm$ and $20nm$, comparable in the absence of interactions with the actual used value of the diameter.

Simulations for systems with a uniform 3D random distribution of easy axis have been performed in order to investigate the difference between the in-field and irreversible approaches to the waiting time method. Figure 3-34 shows that there is a reasonably good

agreement between the corrected waiting time and the S/χ_{irr} methods while the uncorrected waiting time method produces results significantly different from the other two.

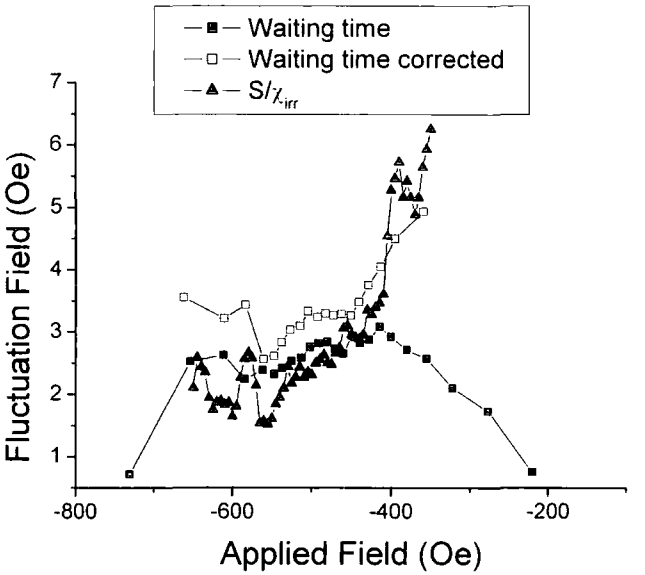

Figure 3-34. Simulated fluctuation field for a random oriented particle system

The experimental results obtained by Antel et. al [29] for a CoCrPtB alloy thin film show a similar qualitative behaviour with a good agreement between corrected waiting time and S/χ_{irr} methods and significantly different results given by the uncorrected waiting time method (Figure 3-35).

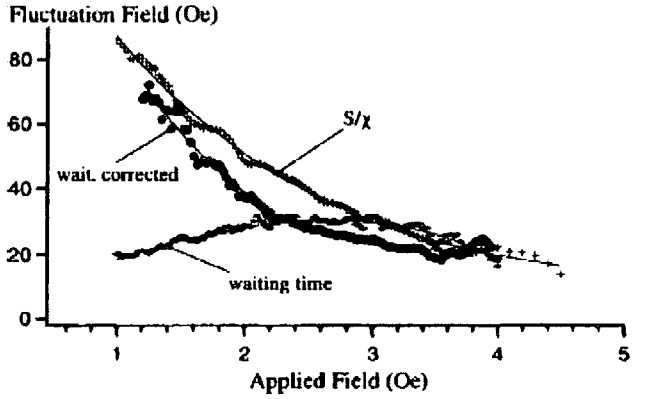

Figure 3-35. Measured fluctuation field for a CoCrPtB alloy thin film

The difference between the scale of the experimental values and that of the simulation results is due to the fact that the simulations were performed independent of the

experiments and were not meant as a fit for the experiments. To obtain quantitative agreement with experimental data, the simulation parameters need to be adjusted by a fit of other magnetisation curves (hysteresis loop, DCD, time-dependance) of the sample.

3.9. Giant magnetoresistance (GMR) considerations

The giant magnetoresistance phenomenon consists in a variation of the electrical resistivity of certain ferromagnetic materials with their magnetic state. This behaviour occurs in samples in which areas of ferromagnetic material are separated by a metallic non-magnetic material such as ferromagnetic multilayers and granular media. It has been shown [60] that the resistivity of the sample is related to the correlation between the magnetic moments of the ferromagnetic areas (ferromagnetic grains in the case of granular magnetic solids).

The phenomenon results from the spin-dependent scattering probability of electrons passing from a nonmagnetic to a ferromagnetic region (interface scattering) and also within the ferromagnetic regions [61]. The model considers that this probability exponentially decreases with the distance covered by the electrons, $p = \exp(-r/r_0)$ where r_0 , the *spin diffusion length*, is the distance after which the probability of the electron maintaining its initial polarization decreases by a factor of $1/e$. Considering this expression for probability, the correlation function related to the GMR becomes

$$\langle \vec{\mu}_1 \cdot \vec{\mu}_2 \rangle = \frac{\sum_{i=1,n} \sum_{j=1,n_i} \vec{\mu}_i \cdot \vec{\mu}_j \exp(-r_{ij}/r_0)}{\sum_{i=1,n} \sum_{j=1,n_i} \exp(-r_{ij}/r_0)} \tag{3.8}$$

where n is the total number of particles and n_i is the number of neighbours considered for particle i. In the simulations a value of 1.5 average particle diameters was considered for the spin diffusion length.

Clearly, the GMR is a macroscopic reflection of the micromagnetic correlations considered in (3.4). However, the difference between the correlation functions described by (3.4) and (3.8) is that the latter is restricted in range by the spin diffusion length, which is a factor which must be considered in relating the GMR to micromagnetic correlations. Also the correlation function was calculated as a function of particle distance and orientation

with respect to the magnetic moment while (3.8) is averaged over all distances and orientations.

The calculated MR curves at different concentrations for the dipolar-only and dipolar and exchange cases show a form similar to that observed experimentally. The experimental data given in [62] for Co-Ag films show dramatically different behaviour for films with packing densities of 0.3 and 0.5. The lower packing density shows a GMR which is close to quadratic in M, whereas the higher packing density shows strong deviations from quadratic behaviour. This change is accompanied by a change in character of the magnetic behaviour from essentially superparamagnetic to ferromagnetic behaviour at the higher density, dominated by the properties of quasidomains formed by the intergranular exchange coupling. This behaviour, including a reduction in the absolute magnitude of the GMR, is perfectly consistent with our model calculations and the conclusion that the GMR is reduced in strongly ferromagnetically correlated systems (see Figure 3-36).

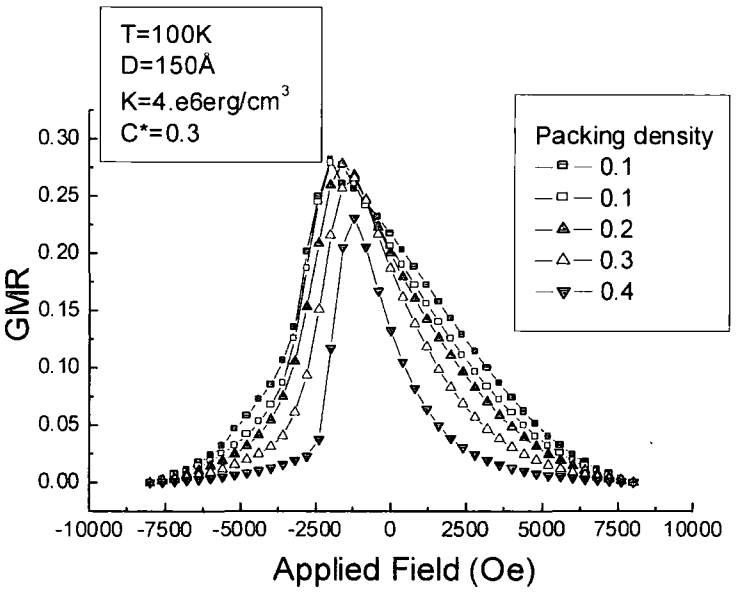

Figure 3-36. GMR curves for systems with different of packing density ε

The form of the GMR curves is characterised using the maximum height of the GMR curve and a "linewidth" given by the field width at half the maximum height of the GMR curve. The GMR can be used as a measure of the degree of local correlation in the

system. For dipolar interactions only, the maximum value of the magnetoresistance is near the coercivity value in agreement with experiment. There is a small increase in the GMR when we increase the concentration. This is due to two reasons: first because, when we increase the concentration, the grains are closer and more scattering events can occur. Second, the dipolar interactions encourage the formation of flux closure loops, which increases the magnetic disorder of the system. On the other hand, an increase in the linewidth is observed, which means that we have more disorder at higher fields. This local disorder increases the spin-dependent scattering and increases the resistance. The effect of the exchange interactions is to give rise to a decrease in the magnetoresistance with concentration. This supports the theory of cooperative effects between neighbouring grains which experience exchange coupling. The local alignment of the grains is detrimental to magnetoresistance because it reduces the magnetic disorder and the spin-dependent scattering of the electrons.

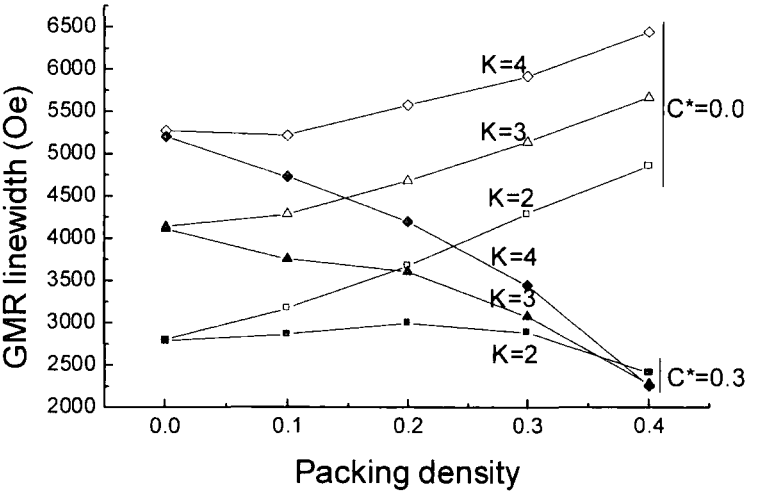

Figure 3-37. GMR linewidth as a function of anisotropy and packing density

In order to quantify this behaviour we consider first the variation of the magnetoresistance "linewidth" with concentration for different anisotropy constants and coupling as shown in Figure 3-37. For the case of dipolar interactions only we observe an increase of the linewidth with concentration. Taking into account that the GMR is a measure of the misalignment of the moments of the grains in the cell this means that spin-dependent scattering starts at lower fields. For the case of exchange, the GMR linewidth

decreases with concentration because the moments of the particles are locally more correlated.

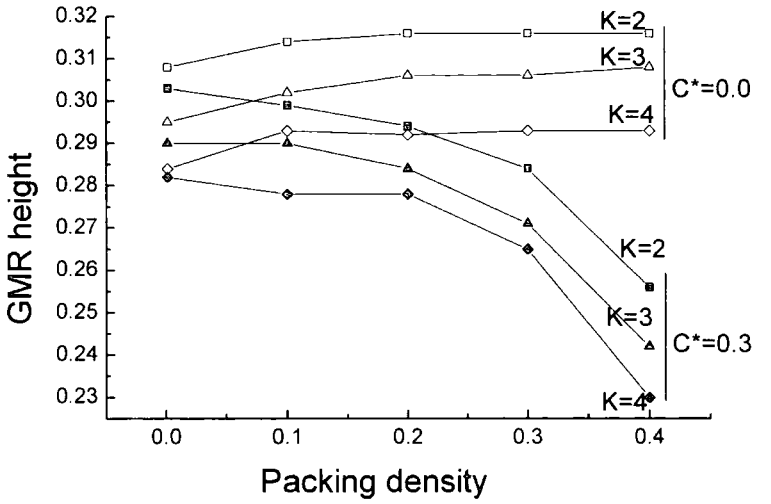

Figure 3-38. GMR height as a function of anisotropy and packing density

The peak height of the GMR can be seen in Figure 3-38 where the GMR can be seen to decrease when increasing the anisotropy. A system with a large value of anisotropy is less mobile, which means that there is less disorder on the local scale defined by the spin diffusion length. We can also observe that the GMR height increases for the dipolar interactions when we increase the concentration. For the case of exchange interactions we can observe a decrease in the height of the peak when we increase the concentration due to the correlation in the system between the magnetic moments of the particles.

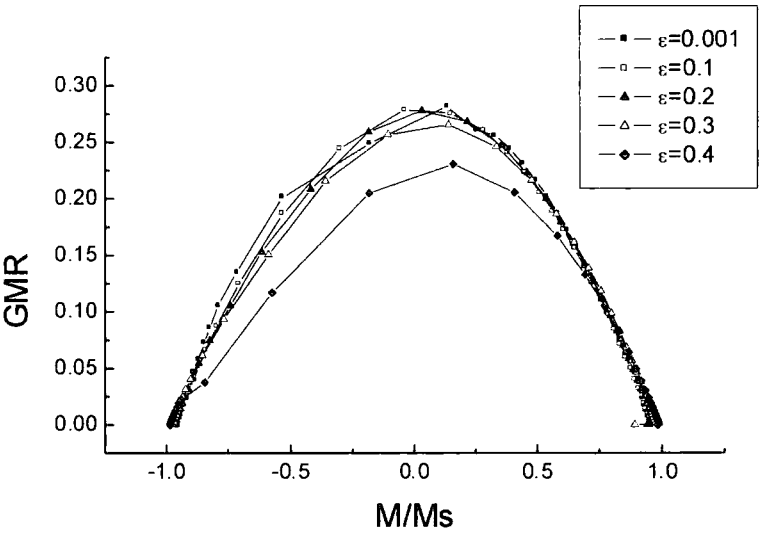

Figure 3-39. GMR variation with the reduced magnetisation of the sample

Finally, Figure 3-39 shows the GMR versus the reduced magnetization, which is given by M/M_S. The exchange interactions result in a reduction of the GMR and a deviation from the parabola expected for a non-interacting system. If the moments within a radius drawn out by the spin diffusion length are correlated due to exchange, then there will be little or no spin dependent scattering and hence no GMR, evidence for cooperative reversal.

3.10. Ferromagnetic resonance

The ferromagnetic resonance (FMR) is a well known investigation technique of ferromagnetic materials. A typical FMR curve is obtained by measuring the microwave absorption coefficient of a ferromagnetic sample as a function of an external applied magnetic field and/or microwave frequency. Depending on the nature of the sample in certain conditions (value of the applied field or microwave frequency) the frequency of the natural gyration mode of the magnetic spins in the sample will match the microwave field frequency leading to a resonant energy transfer from the microwave into the sample. This gives a useful insight on the laws that govern the dynamic of the magnetic spins and on the various parameters involved. However, the interpretation of the data obtained by FMR measurements is not straightforward as they are affected not only by the nature of the sample but also by interaction effects.

The model presented here can also be used to understand how interactions affect the FMR measurements in granular magnetic recording media. The calculations for the microwave absorption coefficient were performed using a method based on the Netzelmann equations for the absorption coefficient of a Stoner-Wohlfarth particle.

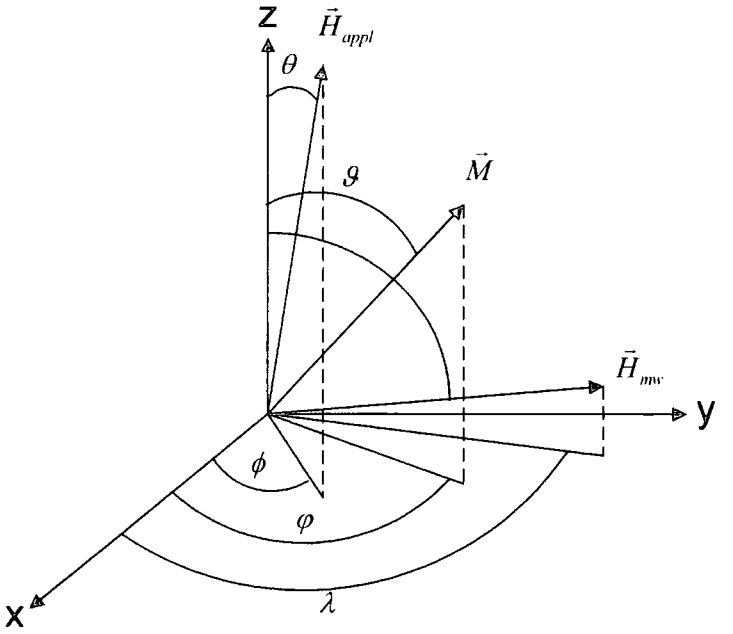

Figure 3-40. Coordinate system for FMR analysis of a Stoner-Wohlfarth particle

It has been shown [63] that for a Stoner-Wohlfarth particle with the orientation of magnetic moment, external magnetic field and microwave field as shown in Figure 3-40 the susceptibility tensor can be expressed as

$$\chi = \frac{\gamma^2\left(1+\alpha^2\right)}{\omega_{res}^2 - \omega^2 + i\omega\Delta\omega}\left[l^2\left(\mu_0 E_{\theta\theta} + \frac{i\omega\alpha M_s}{\gamma\left(1+\alpha^2\right)}\right) + m^2\left(\frac{\mu_0 E_{\varphi\varphi}}{\sin^2\vartheta_0} + \frac{i\omega\alpha M_s}{\gamma\left(1+\alpha^2\right)}\right) + 2lm\frac{\mu_0 E_{\theta\varphi}}{\sin\vartheta_0}\right] \tag{3.9}$$

where ω is the microwave frequency, γ the electron gyromagnetic ratio, α the damping constant, μ_0 the vacuum permeability, M_s the bulk saturation magnetisation of the sample, $E_{\theta\theta}$, $E_{\varphi\varphi}$ and $E_{\theta\varphi}$ are the derivatives of the total energy of the particle with respect to the orientation angles of its magnetic moment at the equilibrium orientation (φ_0, ϑ_0),

$$\omega_{res} = \frac{\gamma\left(1+\alpha^2\right)^{1/2}}{M_s \sin\vartheta_0}\mu_0\left(E_{\theta\theta}E_{\varphi\varphi} - E_{\theta\varphi}^2\right)^{1/2} \tag{3.10}$$

$$\Delta\omega = \frac{\gamma\alpha}{M_s}\mu_0\left(E_{\theta\theta} + \frac{E_{\varphi\varphi}}{\sin^2\vartheta_0}\right) \tag{3.11}$$

and the weight factors

$$l = \sin\delta \sin(\varphi_0 - \lambda) \tag{3.12}$$

$$m = \cos\vartheta_0 \sin\delta \cos(\varphi_0 - \lambda) - \cos\delta \sin\vartheta_0 \tag{3.13}$$

select the tensor component measured for a given orientation of the microwave field and magnetisation. These equations can be reduced to a dimensionless form using the transformations:

$$\tilde{\omega} = \frac{\omega}{\gamma\mu_0 H_k} \text{ and } e = \frac{E}{2K} \tag{3.14}$$

with K the anisotropy constant of the material and $H_K = \frac{2K}{M_s}$ - the anisotropy field. This way the reduced susceptibility has the form:

$$\tilde{\chi} = \frac{d(M/M_s)}{d(H/dH_k)} = \frac{H_k}{M_s}\chi = \frac{1+\alpha^2}{\tilde{\omega}_{res}^2 - \tilde{\omega}^2 + i\tilde{\omega}\Delta\tilde{\omega}} \times \left[l^2\left(e_{\theta\theta} + \frac{i\tilde{\omega}\alpha}{1+\alpha^2}\right) + m^2\left(\frac{e_{\phi\phi}}{\sin^2\theta} + \frac{i\tilde{\omega}\alpha}{1+\alpha^2}\right) + 2lm\frac{e_{\phi\theta}}{\sin\theta}\right] \tag{3.15}$$

where

$$\tilde{\omega}_{res} = \frac{(1+\alpha^2)^{1/2}}{\sin\theta}(e_{\theta\theta}e_{\phi\phi} - e_{\theta\phi}^2)^{1/2} \tag{3.16}$$

$$\Delta\tilde{\omega} = \alpha\left(e_{\theta\theta} + \frac{e_{\phi\phi}}{\sin^2\theta}\right) \tag{3.17}$$

The numerical calculation of the energy derivatives is done via a formalism in which the derivatives of an expression f depending on a unit vector $\vec{m} = (\cos\varphi\sin\theta, \sin\varphi\cos\theta, \cos\theta)$ with respect to the spherical coordinate angles of the vector are calculated as follows:

$$\frac{\delta f}{\delta\alpha} = \frac{\delta f}{\delta\vec{m}} \cdot \frac{\delta\vec{m}}{\delta\alpha},\ \alpha = \theta, \varphi \tag{3.18}$$

$$\frac{\delta\vec{m}}{\delta\theta} = (-\cos\varphi\cos\theta, -\sin\varphi\cos\theta, \sin\theta) \tag{3.19}$$

$$\frac{\delta\vec{m}}{\delta\varphi} = (-\sin\phi\sin\theta, \cos\varphi\sin\theta, 0) \tag{3.20}$$

At each applied field the micromagnetic model described previously is used to calculate the stationary magnetic state. The imaginary part of the susceptibility is then

calculated using the local field for each particle, thus explicitly including interactions into the calculations. However, since this description of FMR assumes that the magnetic moment is in the equilibrium position, the Metropolis algorithm used to describe the behaviour of superparamagnetic particles is no longer used.

Figure 3-41 shows the simulated FMR curves for systems with different packing densities ε when only dipolar interactions are taken into account. The most significant aspect of the interaction increase is a decrease of the peak FMR value as well as a broadening of the curve. However, the resonance field does not seem to be affected by the strength of dipolar interactions. The initial width of the FMR curve observed for the very low packing density system is due to the random orientation of the easy axis and anisotropy fields existing in the system. The broadening of the curve induced by increasing the strength of dipolar interactions shows the effect of the local field acting upon each particle. This effect is superimposed over the initial width but the fact that the resonance field is not shifted shows that dipolar interaction fields average to zero. These results are in agreement with simulations including dipolar interactions only obtained by Thomas et. al. [64] for the case of a spherical sample.

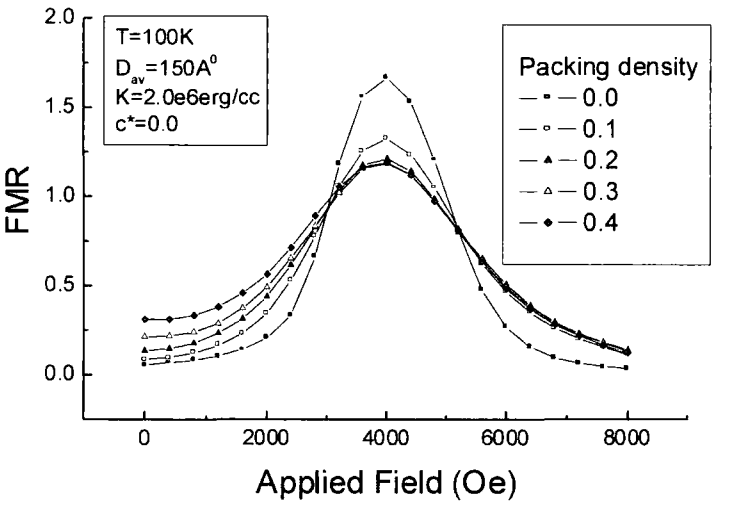

Figure 3-41. Dipolar interaction effects on FMR simulations

This is not the case when exchange interactions are present. As seen in Figure 3-42, the presence of exchange coupling leads, along with a further decrease in the FMR peak value and a further increase in linewidth, to a very pronounced shift of the resonant field

towards lower values. This is evidence of the fact that the exchange interaction field is not symmetric in the sense that for system with non-zero magnetisation the exchange interaction field, which has the same orientation as the individual magnetic moment that produces it, has a preferential direction along the direction of the magnetisation of the sample.

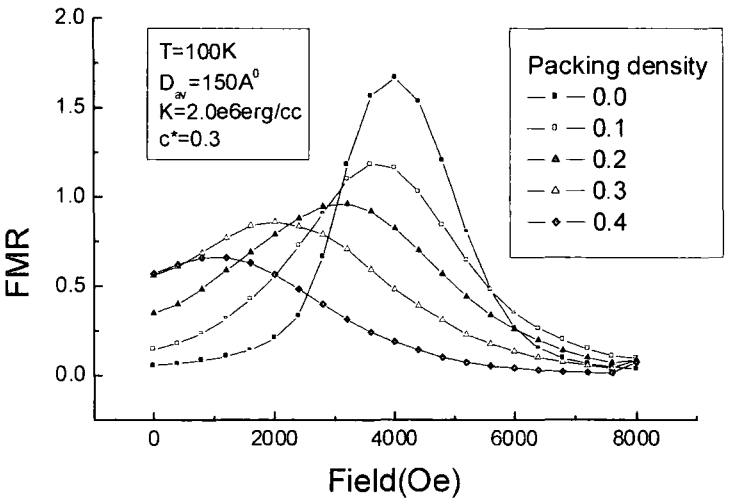

Figure 3-42. Exchange coupling and dipolar interaction effects on FMR simulations

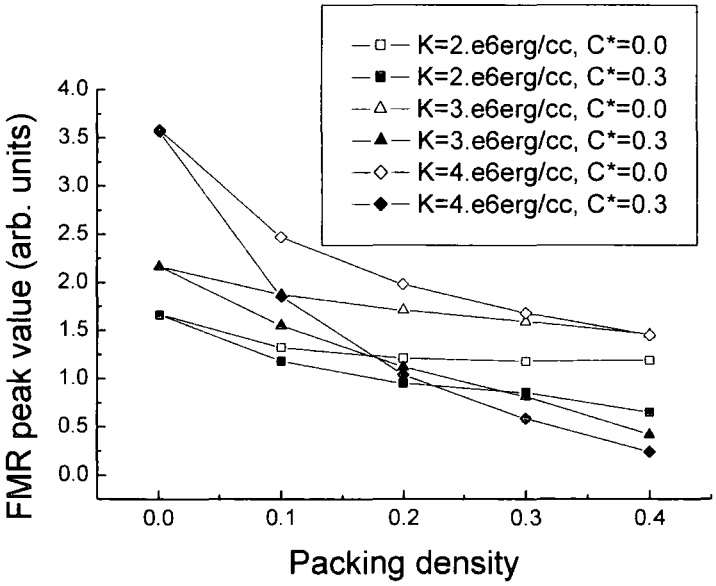

Figure 3-43. Variation of FMR peak value with interactions for different values of anisotropy

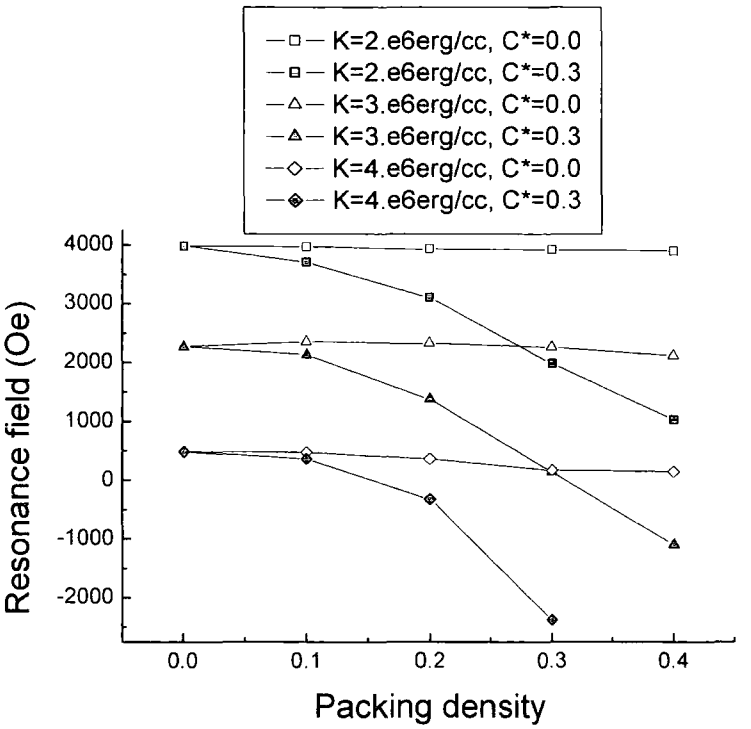

Figure 3-44. Resonance field variation with interactions for different values of anisotropy

Systematic results for these effects are shown in Figure 3-43 (variation of peak value), Figure 3-44 (variation of resonance field) and Figure 3-45 (variation of linewidth). It is clear that both types of interactions lead to a decrease of the peak FMR value, that the resonance field is only affected by the exchange interactions and that both dipolar and exchange interactions lead to an increase in the linewidth. However, since when increasing the value of the anisotropy constant the resonance field decreases and the linewidth of the curve increases, this makes it difficult to estimate the linewidth of the curve in the case of $K = 4 \times 10^6 erg/cc$ as even around zero applied field, the absorption coefficient doesn't decrease to a value below half its peak value.

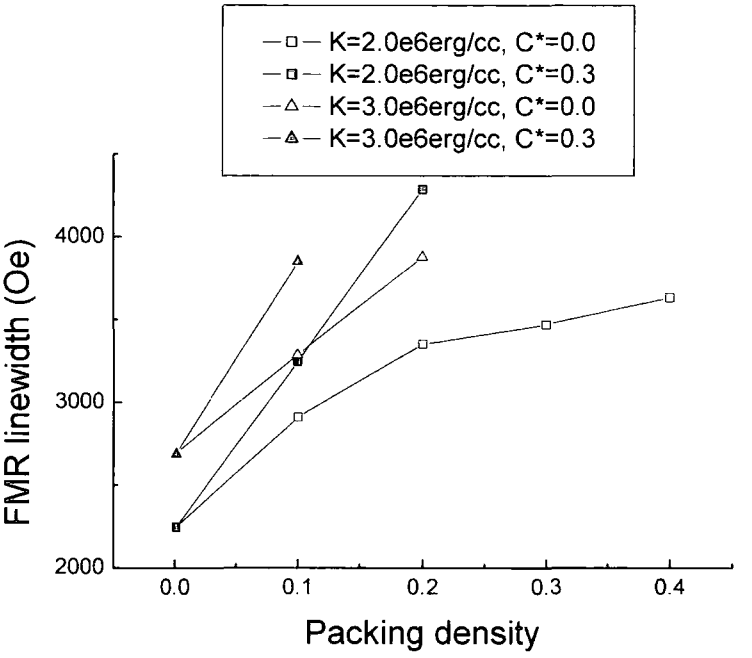

Figure 3-45. Variation of FMR linewidth with interactions for different values of anisotropy

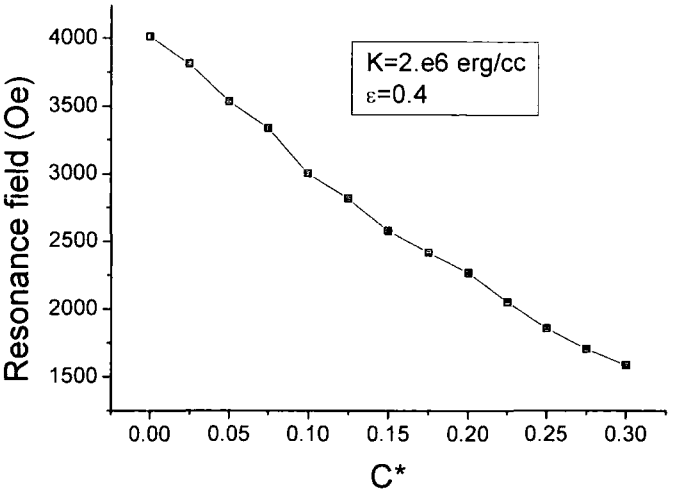

Figure 3-46. Variation of resonance field with exchange coupling parameter

A more systematic study on the influence of exchange coupling interactions on the resonance field is shown in Figure 3-46. Here only a system with a high packing density $\varepsilon = 0.4$ was considered so that the exchange interactions will have a large contribution. It can be seen that when the exchange coupling constant C^* is varied in the range 0.0...0.3 the resonance field almost linearly decreases. This confirms the hypothesis that the

interaction field leads to an increased local magnetic field felt by each individual particle, with the result that a smaller external applied field is needed to achieve resonance.

However, it is important to note the fact that the influence of the damping parameter on the resonance curves is quite similar to the influence of interactions (Figure 3-47).

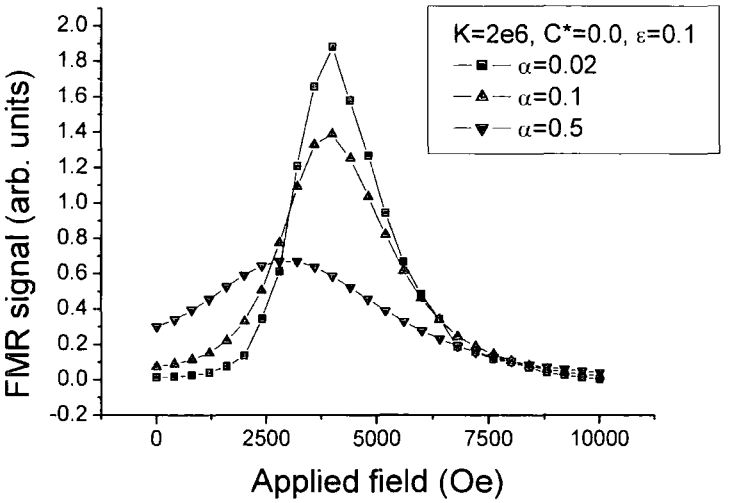

Figure 3-47. Effect of damping parameter variation on FMR curves

Here it can be seen that an increase in the damping parameter α produced a change in loop shape similar to that produced by interaction effects. This leads to the implication that the increase in exchange interaction may consequently affect the damping parameter. This is further evidence of the ability of FMR to probe the intrinsic state of the system and the need for it to be used together with other methods of characterisation such as magnetoresistance, magnetisation, remanence and ΔM curves to decide which of the possible explanations is the real cause for a certain effect.

Chapter 4. Metal particle dispersions

4.1. Introduction

Although the storage industry is more biased towards very high-density recording media types like hard-drives or optical devices as CDs or DVDs for a large number of applications magnetic tapes are still of great importance. In cases when fast random access to the data stored is not a major issue but long term stability of the written information is needed, as is the case of back-up torage, the low cost solution of magnetic tapes is usually preferred. For this reason effort is put into research and development of the process of tape manufacturing, in order to improve their recording densities and stability.

This process [65], [66] is very complex, and each manufacturer employs a different one, usually proprietary, the details of which are restricted by confidentiality. However, they generally follow a pattern which will be briefly discussed.

The magnetic particles, usually referred to as "magnetic pigment", that will form the memory units of the final product are dispersed in a solvent together with wetting agents, resins, activating agents, additional particles and lubricants.

The wetting agent or surfactant acts as an intermediary between the surface of the pigment and the solvent. Its effect is to wet the pigment and break up agglomerates, thus dispersing individual particles into the solvent. The surfactant contributes a repulsive force to the particle-particle interaction that is sufficient to overcome the short range Van der Waals forces and prevent irreversible aggregation.

A blend of resins with different properties such as flexibility, physical and chemical stability and durability is used, taking into account the availability of suitable solvents and their compatibility with the other constituents and the substrate film.

The activating or cross-linking agent is added to the resin when it is required to be set or hardened from the liquid phase to the solid phase.

Additional particles may be added to the dispersion for different purposes. Carbon black may be added to increase the electrical conductivity of the final coating in order to help reduce the build up of static electricity while abrasive powder may be added to improve the surface characteristics required during the movement of the tape in the tape transport system and over the tape heads. Lubricants are used to reduce friction and wear of a tape during use. They also help to prevent wear of the heads and reduce temperature build up due to friction points in the transport system.

The first stage of the dispersion preparation is the wetting of the magnetic pigment in a solvent with the aid of the surfactant. The premixing is carried out in a sawtooth mill and the high viscosity of the mix ensures high shear forces generated by the blade rotating at several thousand revolutions per minute. The wetting process is exothermic and is usually carried out in a water cooled vessel, the magnetic pigment being added to the surfactant and solvent mix. When the wetting is complete a mixture of resins dissolved in a solvent is slowly added to maintain the conditions of high shear.

After the premix, the mixture is milled to generate a homogeneous dispersion of magnetic pigment. The milling is usually by a ball mill which generates very high shear forces that serve to separate the pigment particles and disperse them within the matrix of resin molecules.

On completion of the milling stage the dispersion is diluted or letdown in order to lower its viscosity, a process that renders the dispersion to a state suitable for coating onto the substrate film. The letdown is carried out under high shear conditions by slowly adding a resin and solvent mixture.

Before the dispersion is coated, the resins must be activated to promote hardening by cross linking. This usually entails the addition of a hardener which is designed to set the resin at a speed compatible with an efficient coating and finishing machine. The coating of the dispersion is usually performed by a coating machine which also performs aligning, drying and calendering. A common method of coating is known as knife coating. The knife is a precision knife blade held at a critical height above the surface of the moving substrate film and lying transverse to the direction of motion. The dispersion is exuded onto the substrate surface from a reservoir in front of the blade. The motion of the substrate drags

the dispersion under the knife blade to yield a coating with a thickness determined by the distance between the substrate and the blade.

Immediately after coating, the particles of the magnetic pigment are aligned by the influence of orientating magnets to give the coating the desirable magnetic characteristics for recording, which are high squareness and coercivity.

The resins need to be set as soon as possible after the pigment has been magnetically aligned. The tape is passed through a heated area to assist the evaporation of the solvents and the curing of the resins. Before the resins are completely set, it is possible to improve the surface qualities of the tape by calendaring. The tape is passed under pressure between highly polished rollers which serve to smooth the surface and possibly compress the layer. The process is finished by cutting the tape to the required width and winding it onto reels for packaging. The model described in this chapter concentrates on simulating the alignment and drying processes of the dispersion used in the magnetic tape process, which are extremely challenging physical problems, complicated by the presence of interparticle interactions.

4.2. Metal particles

The metal particles that are used as magnetic pigment usually consist of an iron metal phase with a thin passivation layer that is needed to stabilise the particle against oxidation since Fe is pyrophoric. The passivation layer is usually 4-6 nm thick. The particles are acicular in shape with a length of a few tenths of a micron and an aspect ratio of 5-10.

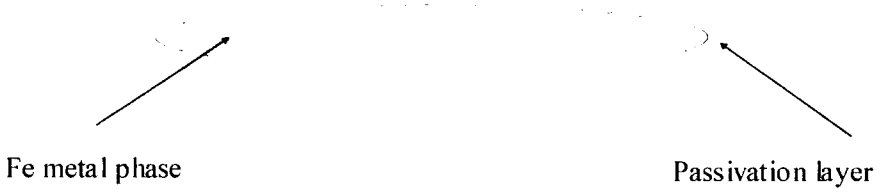

Figure 4-1. Metal particle constituents

The recording density of magnetic media using metal powder almost doubles every year [67] and one of the major factors that contributed to this is the advance in the metal

powder fabrication techniques leading to particles with significantly improved performances as shown in Table 4-1 [68].

Property	MP1 (e.g., Toda B-III)	MP2 (Dowa HM-101)	MP3 (Dowa HM-94)
Density (gm/cc)	5.48	5.73	5.70
Coercivity (Oersted)	1605	1830	2355
Moment (emu/gm)	120	143	146

Table 4-1. Properties of different generations of metal particles

These improvements resulted from the introduction of new technologies such as the use of novel materials such as Fe-Co alloys and continuous reduction in the particle size. In the model, particles with characteristics of the MP3 generation are being simulated.

4.3. Description of the model

The model, based on the model described in [66] and [24] takes into account a number of particles that are modelled as cylinders with two hemispheres at the ends. The particles have lognormal distribution of diameters and lengths. For convenience, in the model the particle radii and half lengths are used as shown in Figure 4-2. These model particles include both the Fe core and the passivation layer.

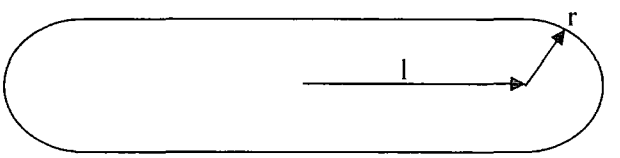

Figure 4-2. Model particle

The computational cell is chosen with an y/x aspect ratio of approximately the same value as the average particle aspect ratio so that in the resulting configuration, when most

particles are aligned to the direction of the applied field, the number of particles is of the same order when measured on the two directions. The height of the computational cell is chosen so that the magnetic pigment volume fraction in the resulting configuration is in the range of 40% as obtained experimentally. A periodic boundary condition is used in the x and y directions. A given number of particles are uniformly randomly distributed in the computational cell with the constraint that no particle overlaps are allowed and a molecular dynamic type of simulation is performed considering both steric and magnetic interactions between any two particles.

Steric interactions arise from bond stretching, bond angle bending or bond torsion in the passivation layer molecules when they come in contact to molecules from the passivation layer of a different particle. Thus, in the model steric interaction between two particles is taken into account when the minimum distance between their surfaces becomes less than a given repulsion distance d_{rep}. To find the minimum distance between the surfaces of the particles, the distance between any two points on their axes is expressed as:

$$d^2 = \left(\vec{\delta} + \lambda_2 l_2 \vec{u}_2 - \lambda_1 l_1 \vec{u}_1\right) \cdot \left(\vec{\delta} + \lambda_2 l_2 \vec{u}_2 - \lambda_1 l_1 \vec{u}_1\right) \tag{4.4}$$

with $\vec{\delta}$ the vector between the particle centres, l_1 and l_2 the half lengths of the particles, $\vec{u}_1$ and $\vec{u}_2$ the directions of the particle axis and $\lambda_1, \lambda_2 \in [-1,1]$ two parameters that describe the position of the points on the axis. The values of the λ parameters for which the distance has a minimum can be found using the conditions:

$$\frac{\partial d^2}{\partial \lambda_1} = 0 \text{ and } \frac{\partial d^2}{\partial \lambda_2} = 0 \tag{4.5}$$

If one of the values found for λ_1 or λ_2 lies outside the $[-1,1]$ interval, the minimum distance is calculated for the four particular cases, $\lambda_1 = \pm 1$ and $\lambda_2 = \pm 1$ by solving the equations

$$\left.\frac{\partial d^2}{\partial \lambda_1}\right|_{\lambda_2 = \pm 1} = 0 \text{ and } \left.\frac{\partial d^2}{\partial \lambda_2}\right|_{\lambda_1 = \pm 1} = 0 \tag{4.6}$$

and choosing the smallest of the four values.

A steric repulsion force of the conveniently chosen form

$$F_{rep} = F_0 \left(d_{rep} - d_s\right)^2 \tag{4.7}$$

is considered if the surface to surface separation between the two particles d_s, calculated from (4.4) as $d_s = d - r_1 - r_2$ with r_1 and r_2 the radii of the particles, becomes less than the repulsion distance. The strength coefficient F_0 was chosen large enough to enforce that no particle overlaps will be produced by the magnetic attraction between particles while the repulsion distance d_{rep} was chosen small enough, usually about 5% of the average particle radius, to ensure a short-range effect on the steric repulsion. The interaction force is repulsive and oriented in the direction given by the two points corresponding to λ_1 and λ_2 on the cylinder axes. The resulting steric torque is also calculated for each particle.

An additional vertical steric-like force with its resulting torque is used for every particle whose centre is below the bottom or above the top of the computational cell in order to force the particle to stay within the computational cell.

The magnetic interaction forces between two particles are calculated using a pole-pole approximation. Each particle is considered to have two magnetic charges q, placed in the cylinder ends, so that the dipole made by the two charges is equivalent to the magnetic moment of the particle

$$q \cdot 2l = M_s V \tag{4.8}$$

where l is the cylinder half-length, M_s is the saturation magnetisation and V the volume of the core material. The magnetic force is calculated as the sum of the forces between the magnetic charges, with the magnetic torque calculated in a similar way. An additional torque corresponding to an applied orienting pulse field applied on the y-axis is added to the total torque of each particle in the initial stage of the simulation.

Since the particles are considered to be in a solvent of viscosity η, the equation of motion for a particle is written [69], [70]:

$$\begin{aligned} m\dot{\vec{v}}_{\perp} &= \vec{F}_{\perp} - N_{\perp}\vec{v}_{\perp} \\ m\dot{\vec{v}}_{\parallel} &= \vec{F}_{\parallel} - N_{\parallel}\vec{v}_{\parallel} \end{aligned} \tag{4.9}$$

where m is the particle mass, $\vec{F}_{\perp}$ and $\vec{F}_{\parallel}$ are the perpendicular and parallel (to the particle axis) components of the force acting on the particle, $\vec{N}_{\perp}$ and $\vec{N}_{\parallel}$ are the proportionality

coefficients for the viscosity forces and $\vec{v}_{\perp}$ and $\vec{v}_{\parallel}$ are the perpendicular and parallel components of the particle velocity.

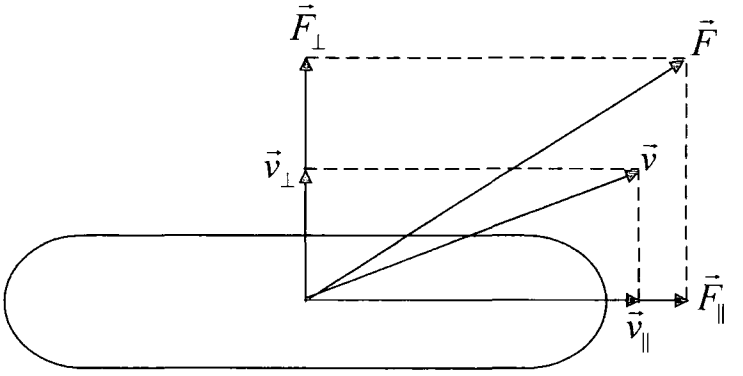

Figure 4-3. Perpendicular and parallel forces and velocities of a particle

Assuming the value of η is big enough so that in a fraction of the considered time-step the particles reach the limit velocity, the new perpendicular and parallel components of particle velocity can be calculated as shown in Figure 4-3:

$$\vec{v}_{\perp} = \frac{\vec{F}_{\perp}}{N_{\perp}}, \vec{v}_{\parallel} = \frac{\vec{F}_{\parallel}}{N_{\parallel}} \tag{4.10}$$

Thus, the total velocity of the particle and the displacement for a time-step can be easily found. A similar technique is applied for the rotation motion [71], [72]. In this case only the perpendicular torque and angular velocity are calculated because the rotation of a particle around its axis doesn't produces any change. The model does not take into account the variation of the viscosity coefficient due to the solvent evaporation during the drying process.

To simulate the drying process, a few techniques have been tried. The first one was the use of a gravity-like force acting on all particles but this one produced an agglomeration of particles on the bottom of the computational cell with packing densities higher than the required ones. A second technique was the use of a surface tension force combined with a continuous decrease of the computational cell height but this technique led to an agglomeration of particles on the top of the computational cell, again with packing densities higher than desired. The best results were produced by using successive rescaling of each particle's z coordinate with some coefficient with a value less than unity (see Figure 4-4). Thus, assuming that the bottom of the computational cell is at $z_b = 0$, at every step the z

position of each particle is changed from z_p to $z'_p = f \cdot z_p$ with $0 < f < 1$ and the computational cell height changes from h_c to $h'_p = f \cdot h_p$. After that the system is allowed to evolve until there are no particle overlaps and all particles are within the computational cell. In practice, the rescale coefficient f is chosen above 0.95 in such a way that the packing density of the system increases each time by a constant amount.

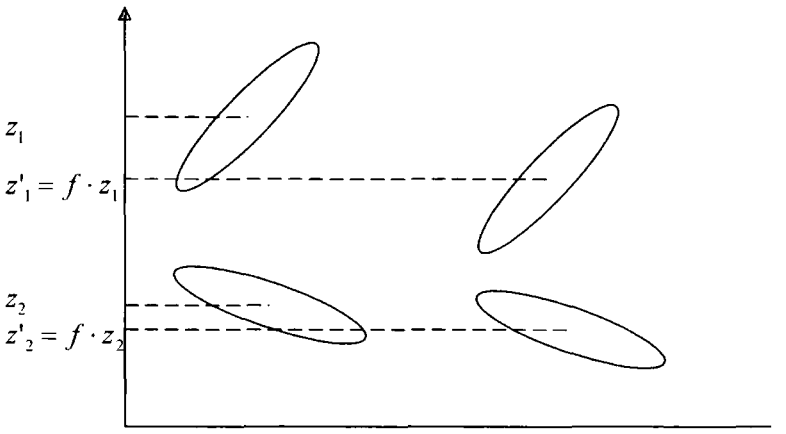

Figure 4-4. Rescale of particle z-position to simulate the drying process

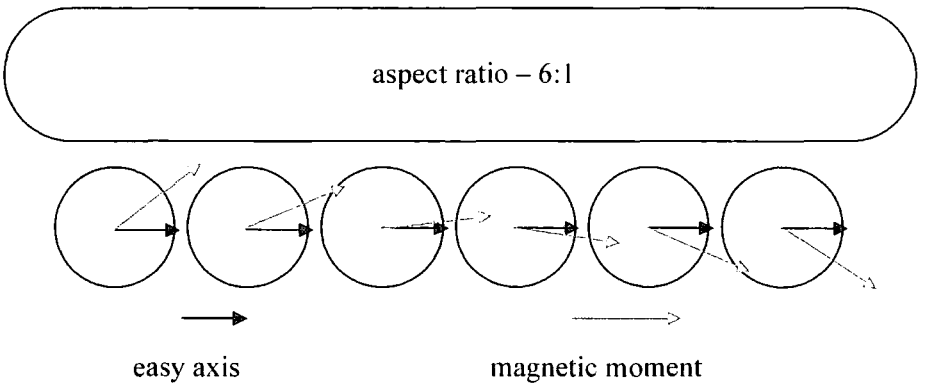

Figure 4-5. Approximation of an elongated particle with a chain of spheres

The configurations obtained after simulating the drying process are used to study the effect of the microstructure on the magnetic behaviour of such tapes. The magnetic properties are simulated using the model described in Chapter 3. However, in order to allow non-coherent rotation within one particle, each of these is approximated with a chain of magnetic spheres [73], [74]. For simplicity, the number of spheres was taken equal to the particle aspect ratio. The easy axes of the sub-particles are along the main particle axis and

they are positioned at equal distances on the axis (see Figure 4-5). The total volume of the spheres equals the volume of the Fe metal phase of the initial particle and exchange interactions are only used between two neighbouring spheres of the same particle.

4.4. The need for clusters

Drying simulations were performed with the model described above, starting from initial packing densities of 5% metal particles and using a dry-down ratio of 1:8 to produce a particle density of around 40%, consistent with the experimental values. Typical values used for the simulation parameters were average particle diameter of $16nm$, average particle size of $80nm$, $M_s = 800emu/cc$, $\eta = 1cps$ and orienting field pulse $H_o = 2000Oe$. Depending on the duration of the orienting field pulse, the configurations obtained showed a degree of particle alignment to the direction of the field, alignment that is also reflected in the squareness of the simulated hysteresis loops, as shown in Figure 4-6, Figure 4-7 and Figure 4-8.

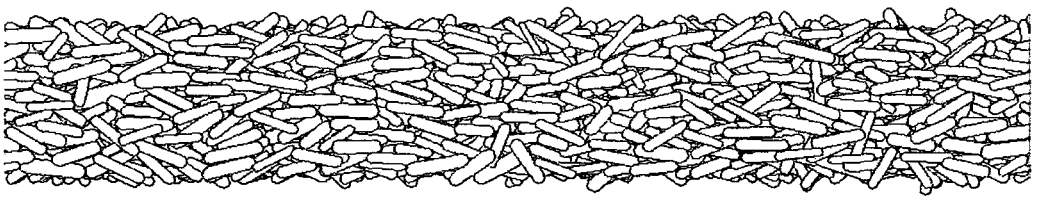

Figure 4-6. Configuration obtained for a pulse field of 0.02s

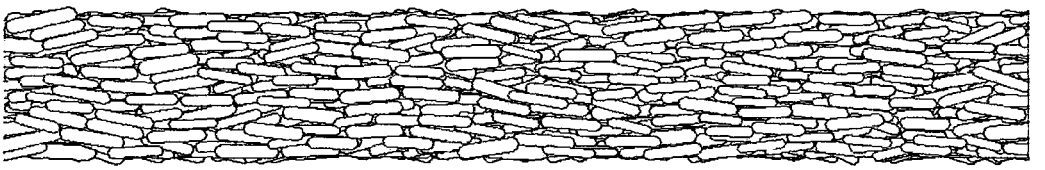

Figure 4-7. Configuration obtained for a pulse field of 0.1s

The results, consistent with previous work in this field [14], [24], [25], [26] show that using a suitable orienting field pulse, the magnetic particles can be aligned to obtain systems with squareness close to 1. However, experimentally the values obtained for the squareness are usually in the range 0.8-0.9 and at microscopic level particles that are not aligned to the direction of the orienting field are observed. In fact, it has been shown [68], [75] that clusters of particles are formed during the pigment manufacturing process, the particles being chemically bound one to each other. These clusters are then present throughout the

magnetic tape fabrication and they are also found in the finite product as shown in Figure 4-9.

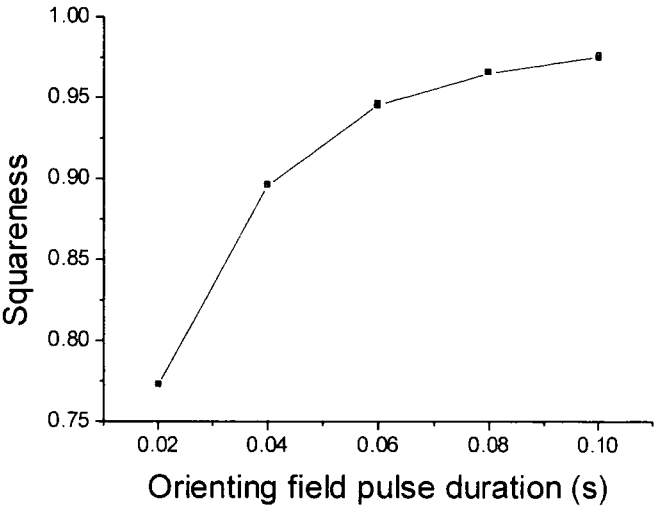

Figure 4-8. Squareness variation with duration of the orienting field pulse

Figure 4-9. Particle clusters observed experimentally in magnetic tapes

It became obvious that, in order to obtain realistic microstructures from the simulations performed, particle clusters had to be included in the model.

4.5. Cluster model

A rigorous analysis of the cluster size distribution and of their intrinsic particle configuration in real magnetic tapes is difficult to employ. Therefore, the computational model tries to bring an insight into how these particle agglomerates behave during the

drying process of the pigment solution and how they influence the properties of the resulting microstructure.

The particle clusters are generated before the actual drying simulation starts using a "hit and stick" procedure. Initially, a single particle is placed with a random orientation of its axis in the point of minimum energy of an attraction potential. Another particle is placed in a random position and with a random orientation so that it does not overlap with the initial particle. Random Monte Carlo moves following a standard Metropolis algorithm are then performed on the second particle until it collides with the initial one. Other particles are then added in turns following the same procedure until a cluster of the desired size is formed. The shape of the obtained cluster can be controlled by using different distributions for the initial random position of the particles. Thus, if this position is chosen at random on the surface of a sphere, spherical agglomerates are formed while if the position is chosen at random on the surface of a cylinder, cylindrical agglomerates are formed (see Figure 4-10).

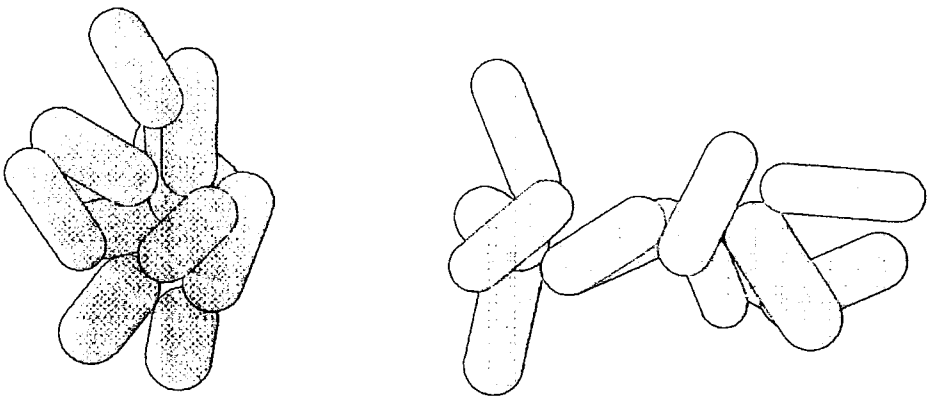

a) Spherical cluster **b) Cylindrical cluster**

Figure 4-10. Clusters obtained using different initial random positioning of particles

However, it has been noticed that in order for the shape of the cluster to be observable, the clusters have to contain a relatively large number of particles, usually above 15. Apart from that much more important than the cluster shape is the particular orientation of each particle in the cluster since, as shown in Figure 4-11 and Figure 4-12, the differences between the hysteresis loops of various clusters with the same shape hide any systematic differences that may occur between the hysteresis loops of clusters with different shapes. Thus, for reason of simplicity, only clusters with a spherical symmetry of the initial particle position were used in the simulations.

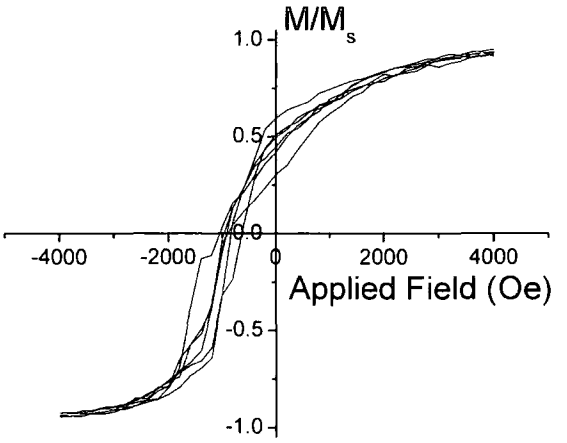

Figure 4-11. Hysteresis loops obtained for different spherical clusters of 15 particles

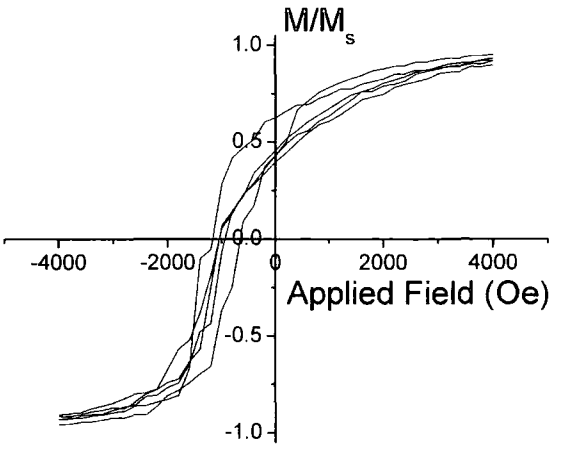

Figure 4-12. Hysteresis loops obtained for different cylindrical clusters of 15 particles

A number of clusters obtained via the method described above were used for the drying simulations. The interactions between clusters and other particles either free or belonging to other cluster were calculated as the sum of individual interactions between the considered particle and each particle of the cluster. The torque acting on a cluster was calculated with respect to the mass centre of the cluster. The values of the drag coefficients for clusters are very difficult to estimate due to the random positioning and orientation of the particles that form them and in simulations the drag forces acting on clusters have been

approximated with the drag forces acting on an equivalent sphere with a volume twice the volume of the cluster particles.

To make a systematic study of the influence of cluster distribution, we needed a method to produce distributions of cluster sizes. For a given particle system we chose the number N of clusters of a specific size n to exponentially decrease with its size. To achieve this we considered the distribution function:

$$N(n) = \left[N_0 \cdot \exp(-k*(n-2))\right], \quad n \geq 2 \tag{4.11}$$

where $[x]$ denotes the largest integer smaller than the real value x, N_0 is the number of clusters containing two particles and k is a parameter that allows changes in the width of the distribution.

Both the value of N_0 and k influence the maximum cluster size, due to the truncation required to obtain integer numbers. Also, N_0 must be chosen large enough so that a true distribution is produced and allow clusters of relatively large size to be created.

However, in order to be able to compare the results obtained for different cluster size distributions the ratio between the number of cluster particles and the number of free particles needs to be kept constant so when changing the cluster size distribution the total number of particles needs to be changed as well.

4.6. Parameter influence on resulting configurations

Simulations have been carried on to study the influence of several factors on the final dispersion properties. The main interest areas have been the effect of cluster particle ratio (the ratio between the number of particles parts of clusters and the total number of particles in the system), cluster size distribution and orienting field.

In order to study the effect of cluster particle ratio, several initial configurations have been produced using the same clusters but different numbers of free particles, so that the ratio between the number of cluster particles and the total number of particles varied from 0.05 to 0.20. The results have been also compared with a configuration containing no clusters.

Figure 4-13 and Figure 4-14 show an expected decrease in squareness and coercivity but this decrease is not linear with the cluster particle ratio, suggesting that this behaviour is not only due to the intrinsic lower values for the squareness and coercivity of a cluster but also to some other mechanism that induces a decrease of these values for the free particles in the system.

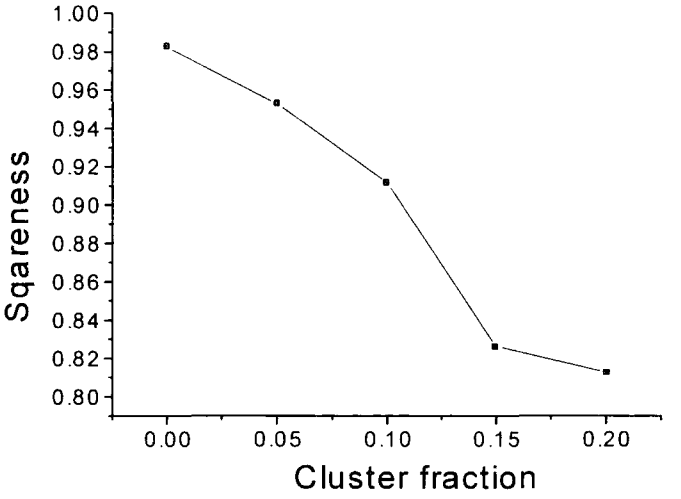

Figure 4-13. Variation of system's squareness with cluster particle fraction

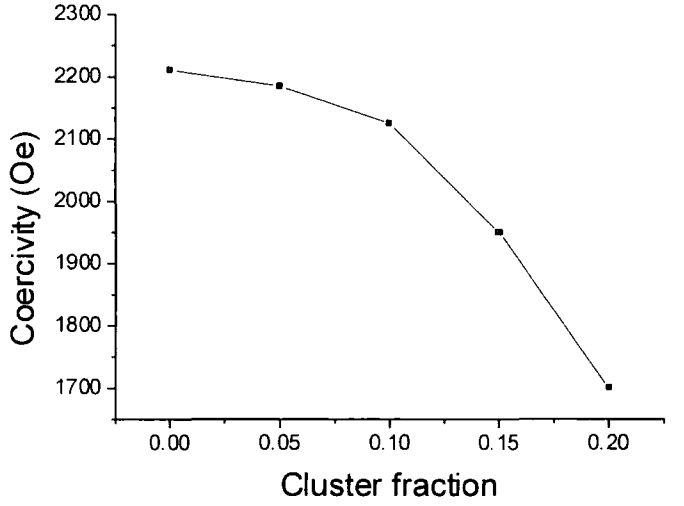

Figure 4-14. Variation of system's coercivity with cluster particle fraction

As shown for systems without clusters (Figure 4-8), an important factor for the characteristics of the obtained configurations is the orienting field that is applied in the form of a short pulse at the first stages of the drying process. The magnitude of this field and the duration of the pulse can have a dramatic influence on the behaviour of the system.

For these simulations of systems containing clusters, the same value for the orienting field $H_0 = 2000Oe$ was used while the pulse duration was varied from 0 to $0.1s$.

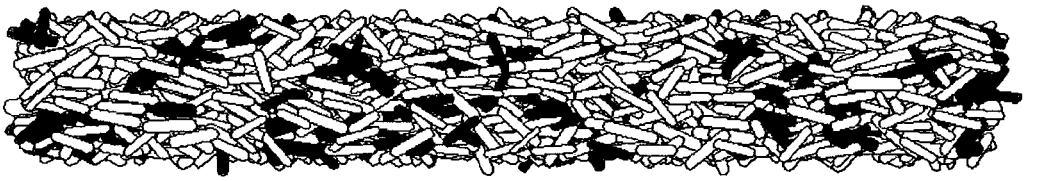

Figure 4-15. Configuration obtained for an orienting field pulse duration of 0.02s

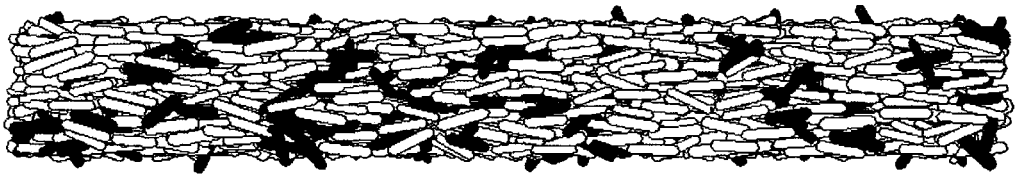

Figure 4-16. Configuration obtained for an orienting field pulse duration of 0.10s

Figure 4-15 and Figure 4-16 show the influence that the duration of the field pulse has on how the particles align (darker particles are cluster particles). The effects on the squareness (Figure 4-17) and coercivity (Figure 4-18) of the obtained configurations are similar to those on systems without clusters (results that are also shown for comparison) with a shift towards lower values due to the misaligned particles in clusters.

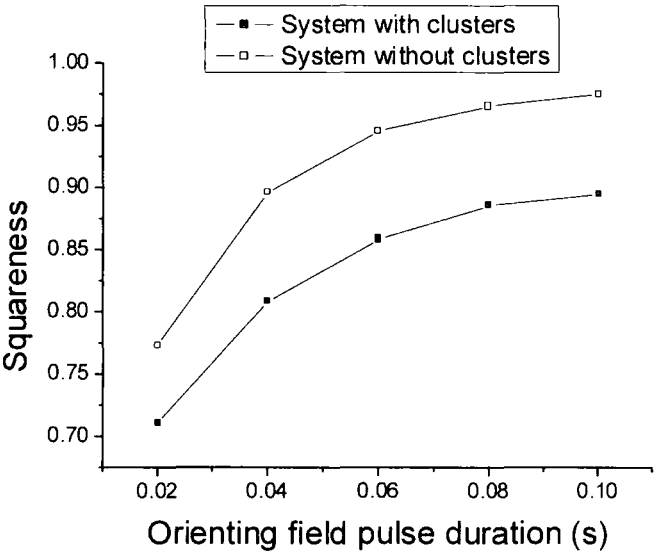

Figure 4-17. Squareness variation with duration of the orienting field pulse

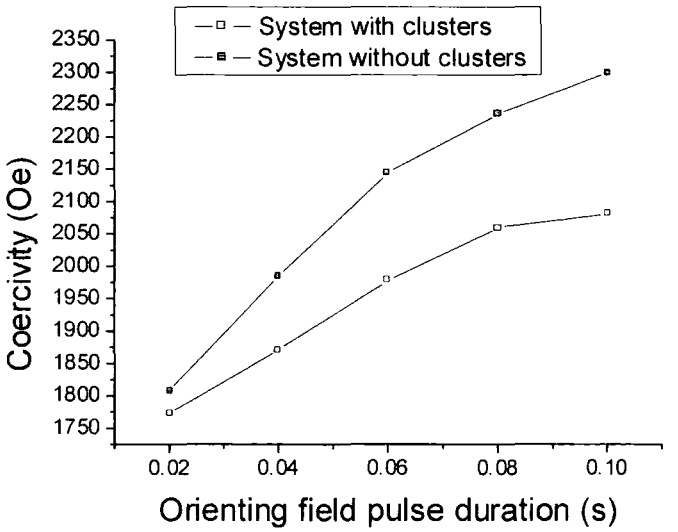

Figure 4-18. Coercivity variation with duration of the orienting field pulse

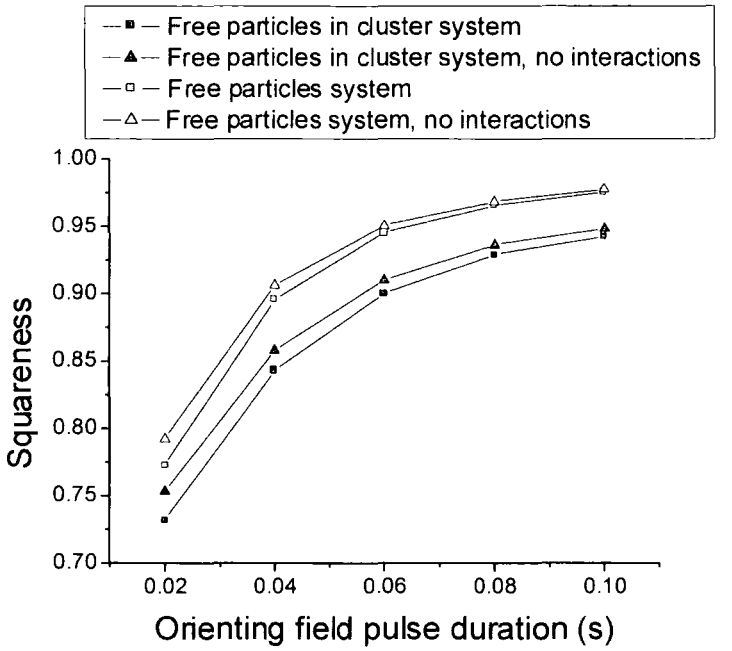

Figure 4-19. Variations of squareness with the duration of the orienting field. Comparison between systems with and without clusters including and excluding interparticle interactions respectively

However, it is not only the cluster particles that contribute to the decrease in squareness and coercivity. Figure 4-19 shows a decrease of the squareness of the free particles in a system with clusters as compared to the value obtained for a system without clusters. In order to make a distinction between the decrease in squareness due exclusively

to the misalignment of particles and the decrease due to different interaction fields brought in by the presence of clusters, the squareness values obtained when not taking into account interparticle interactions were plotted as well. The results clearly show a reduction in the free particle alignment brought by the presence of clusters in the system. This effect can be ascribed to the fact that the presence of the clusters with their random oriented particles disrupts the alignment of the free particles that they come in contact with.

To see how the cluster size distribution influences the obtained microstructure, simulations have been performed in which the k parameter in (4.11) was varied in the range $0.5-2.0$ to change the shape of the cluster distribution in the system, while the number of clusters with two particles N_0 was kept at a constant value of 150. The number of free particles was varied to keep the cluster particle ratio constant.

The configurations were obtained using orientation field pulses of two different durations, i.e. for $0.06s$ (Figure 4-20 and Figure 4-21) which is not sufficient for the alignment process to saturate and for $0.1s$ (Figure 4-22 and Figure 4-23) when most of the free particles are aligned to the direction of the orienting field.

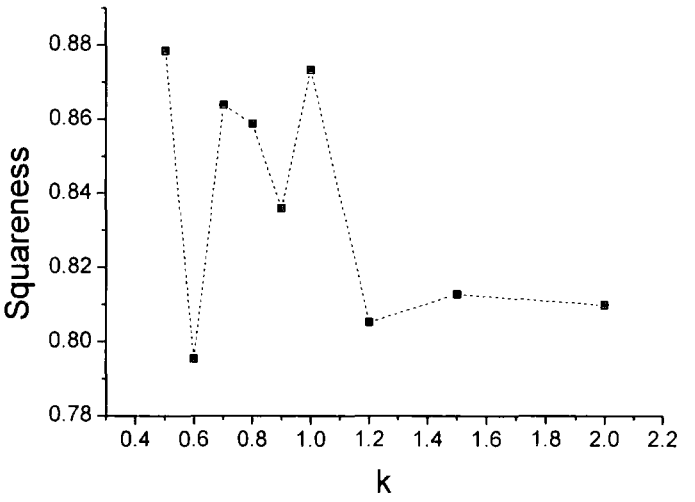

Figure 4-20. Variation of squareness with the value of k at a field pulse duration of 0.06s

However, in neither case can be observed a trend on the variation of either squareness or coercivity with the distribution although one would normally expect the squareness of the system to decrease when increasing the ratio of large clusters because the

larger the cluster the smaller its effective anisotropy. This is due to a random walk effect, which essentially averages over the individual particle orientations in a given cluster.

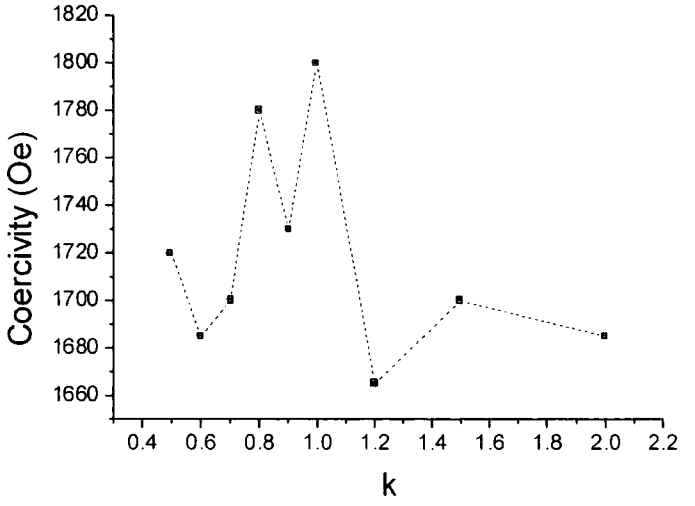

Figure 4-21. Variation of coercivity with the value of *k* at a field pulse duration of 0.06s

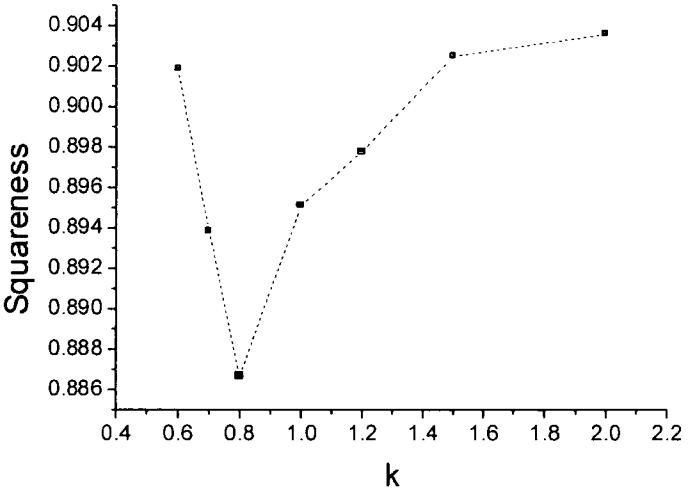

Figure 4-22. Variation of squareness with the value of *k* at a field pulse duration of 0.1s

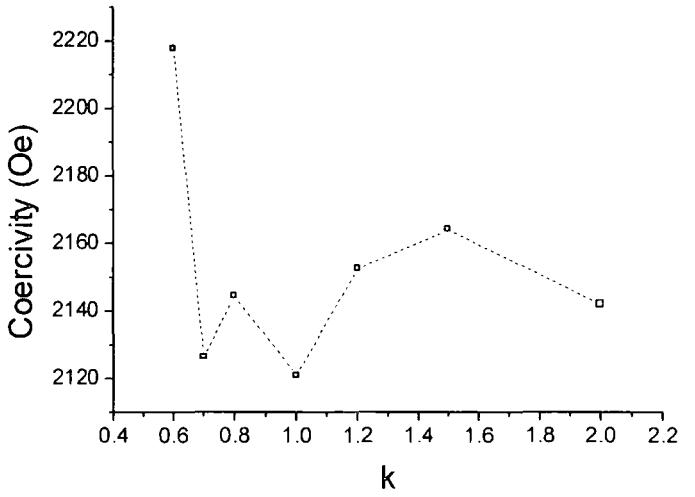

Figure 4-23. Variation of coercivity with the value of *k* at a field pulse duration of 0.1s

For example, according to Stoner-Wohlfarth a large cluster with randomly oriented easy axes has a squareness of 0.5. Such a cluster, which will not be subjected to a torque in the aligning field, will still exhibit remanence of around 0.5. This is not the case for very small clusters (two or three particles) that can have a large net anisotropy when the angles between the axes of their particles are small (see Figure 4-24).

Figure 4-24. Large cluster with small or no anisotropy (left); small cluster with high anisotropy (right)

The fact that no decrease in squareness is observed when the cluster size increases shows that it is not the cluster size that is important but the fact that they are present in the system. The lack of influence of the cluster size on the squareness can be ascribed to the fact that the disruptive effect of several small clusters is larger than that of a single large cluster since the total surface of contact with the free particles is larger in the case of the smaller clusters. However, this is just a hypothesis and further work is needed to thoroughly test it.

One of the approximations used in the model that affects the particle alignment is the fact that during the drying simulation the magnetic moment of a particle is assumed to be oriented in the direction of the particle axis and based on this assumption the interparticle interaction forces and torques are calculated along with the torque produced by the orienting field. In reality, the magnetic moment of the particle will be in a equilibrium position between the particle axis and the local magnetic field while the torque acting on the particle will be given by the particle's anisotropy energy. This leads to an overestimation of the torque, especially when the angle between the particle axis and the local field is large as is usually the case in the initial stage of the simulation when the orienting field acts on the randomly oriented particles. A next stage in the development of the model should take this into account by using a Stoner-Wohlfarth like model to dynamically estimate the orientation of the particle's moment during the drying simulation. On the other hand, when the moment is no longer aligned to the particle axis, the pole-pole approximation used for the particle interaction calculation will no longer be valid and a different method should be employed. A possible solution would be the use of the chain of spheres model for the interaction calculations during the drying process simulation.

The model also makes possible the investigation of the effect of the presence of clusters on the noise obtained in the reading process. Using the microstructures obtained from the drying process simulation, the granular media model can be used to describe the magnetisation state of the system after a "writing" process and it can be adapted to estimate the signal that would be obtained by a read head from the media.

Chapter 5. FePt self-assembled particle systems

5.1. Introduction

In order to increase the areal density of magnetic recording media, a lot of effort is put into using smaller particles as well as using a smaller number of particles per recorded bit. The ultimate limit that can be achieved would be using one particle per bit. In order to achieve this, a certain number of difficulties must be met related not only to the physical ability to safely store the information on a single particle for a sufficiently long period of time but also to the technological ability to identify each individual particle and read/write the information on it at the high speeds required by the market. More than that, these improvements must not involve high production costs so that the products will be economically viable.

The first problem, concerning the stability of the information written on a single particle is related to the thermal effects. As shown in (2.46) as the particle size decreases in order to achieve higher recording densities, the average time for a spontaneous reversal of its magnetic moment orientation decreases, leading to loss of information. To avoid that the particle volume must be kept above the critical value given by (2.41). This can be achieved either by using an exchange coupling of the particle with an antiferromagnetic substrate, thus increasing the effective volume of the particle or by using materials with a higher anisotropy constant that, according to (2.41) will produce a decrease of the critical volume leading to a better stability for information written on particles of a given size. For this reason materials such as FePt (which has a very high anisotropy of approximately $7 \times 10^7 erg/cc$) are being used to produce novel recording media.

The second problem, concerning the ability to identify each individual particle in the recording media, requires the particles to be ordered in arrays so that the position of each one can be theoretically found by knowing only the array parameter and orientation.

To achieve this high degree of particle ordering several techniques [6] are currently being investigated, the most common ones being lithographic deposition and self-assembly. The most common methods used for lithographic deposition are electron beam lithography [76], [77], x-ray lithography [78], [79] and interference or holographic lithography [80], [81]. Most common self-assembly techniques are heterogeneous nucleation of magnetic atoms on metallic surfaces [82], metallic reduction in a magnetic field [83], [84] and reverse micelles [85], [86].

This chapter will focus on simulations of the reverse micelles technique used for obtaining self-assembled systems of FePt magnetic nanoparticles.

The experimental procedure for producing such systems is described in [86]. A combination of oleic acid and oleyl amine is used to stabilize the monodisperse FePt colloids and prevent oxidation. The synthesis is based on the reduction of $Pt(CH_3COCHCOCH_3)_2$ by a diol and the decomposition of $Fe(CO)_5$ in high-temperature solutions. The composition of the particles is adjusted by controlling the molar ratio of iron carbonyl to the platinum salt. The particle size can be tuned from 3 to 10 nm by first growing 3 nm monodispersed seed particles in situ and then adding more reagents to enlarge the existing seeds to the desired size. These particles are isolated and purified by centrifugation after the addition of a flocculent and can be redispersed in nonpolar solvents in a variety of concentrations. When the FtPt colloids are spread on a substrate and the carrier solvent is allowed to slowly evaporate FePt nanoparticles superlattices are produced.

5.2. Description of the model

The model tries to simulate the behaviour of a colloidal system of FePt particles with a surfactant shell during the drying of the solvent and to lead to an understanding of the processes that lead to the self-assembly of these particles.

Started as a molecular dynamics type of simulation, initial calculations showed that for the given particle size the thermal effects are large enough to allow the system to rapidly reach thermal equilibrium. Thus a Monte-Carlo algorithm was subsequently adopted as a method of investigation.

In the model each particle is considered to be a metal core sphere coated with surfactant molecules. These surfactant molecules have a hydrophobic head and a hydrophilic tail so that, in order to avoid contact with solvent molecules the head attaches to the FePt metal core. Such particles interact via a repulsion potential when the metal core surface-to-surface separation becomes less than twice the surfactant molecule length, as shown in Figure 5-1. Also, when due to solvent evaporation or to Brownian motion a particle is left outside the solvent, a surface tension like potential acts on the particle trying to bring the hydrophilic tails of the surfactant molecules back in contact with the solvent.

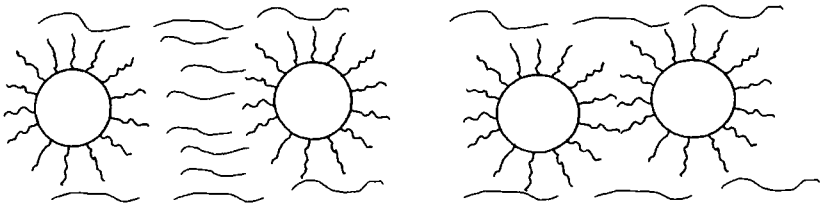

Figure 5-1. FePt particle interaction depending on separation: no interaction (left), repulsion (right)

Although in other self-assembly simulations [15], [16] surfactant and solvent molecules are individually considered as well as other components of the dispersion, in this model surfactant coated metallic particle are represented as a singular entities moving in a viscous fluid representing the solvent, an approach similar to that used in simulations of ferrofluids [27].

As described in [27], the steric interaction potential between such two surfactant coated particles i and j can be described by the formula:

$$\frac{W_{ij}}{k_B T} = 2\pi d^2 \xi \left[2 - \frac{l_{ij}+2}{t} \ln\left(\frac{1+t}{1+l_{ij}/2} \right) - \frac{l_{ij}}{t} \right] \tag{5.12}$$

with $l_{ij} = 2s_{ij}/d$, and $t = 2\delta/d$ where s_{ij} is the surface-to-surface separation between the metallic core of the particles, δ is the surfactant molecule length and d is the diameter of the metallic core. The parameter ξ controls the strength of the interaction and is related to the nature of the surfactant and with the areal density of surfactant molecules attached to the metallic core.

As shown in Figure 5-2, following [27], for surfactant molecules larger than $2nm$, which is the case for the surfactants used in the FePt self-assembly experiments, the steric repulsion energy is much larger than both the magnetic interaction energy and Van der

Waals energy for a wide range of surface-to-surface separation values. Therefore in most cases both the magnetic attraction and Van der Waals energies will be neglected in calculations.

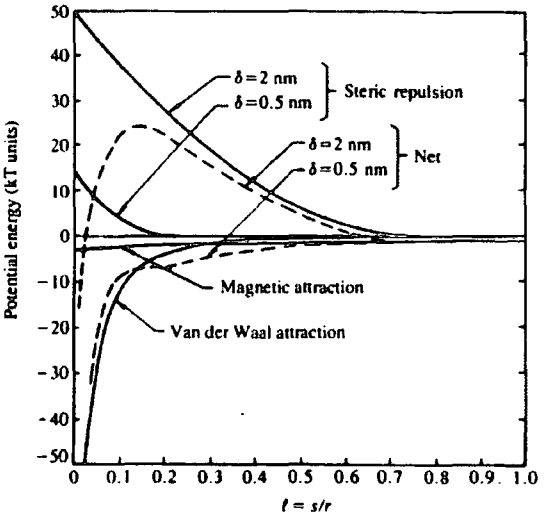

Figure 5-2. Comparison between the steric repulsion energy and Van der Waals and magnetic energies

The model takes into account a system of such surfactant coated particles with a lognormal distribution of diameters, particles that are randomly uniform distributed in the volume of a computational cell with the constraint that overlaps are not allowed. The computational cell can be either in the shape of a box when simulating the behaviour of a dip-coating sample or in the shape of a section of a cylinder, as shown in Figure 5-3 when simulating the behaviour of a droplet sample. Periodic boundary conditions are used in the x-y plane.

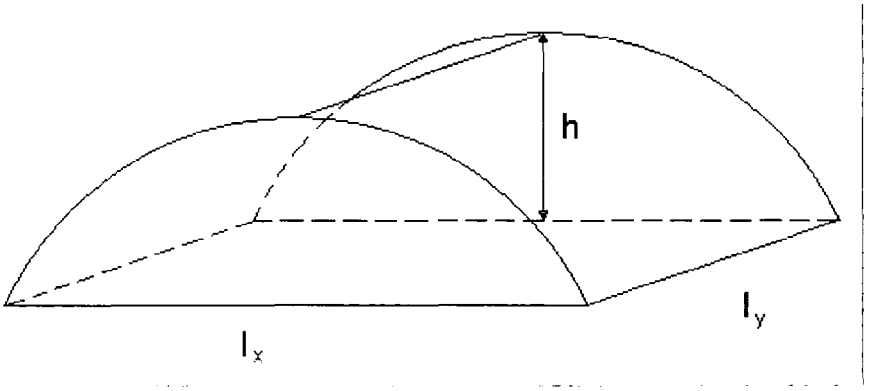

Figure 5-3. Cylinder section computational cell

The flow diagram of the program is shown below:

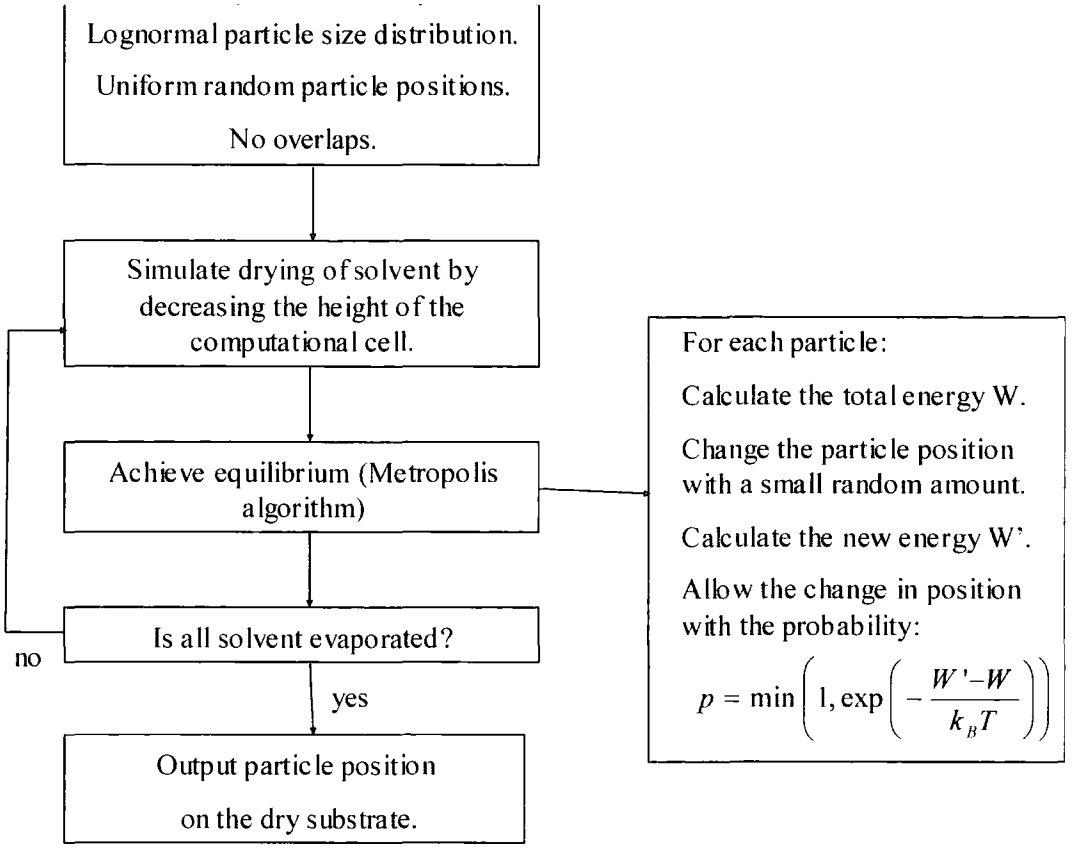

Thermal equilibrium is achieved via a standard Metropolis Monte-Carlo algorithm. The total energy of the system W is calculated, a random particle is moved by a small random amount and the energy of the system in the new state W' is evaluated. A transition probability is defined as $p = \min\left(1, \exp\left(\frac{W'-W}{k_B T}\right)\right)$ and a random number x is generated from a uniform distribution in the $[0,1]$ interval. If the random number x is less than the transition probability p the change of the particle position is accepted, otherwise the particle is returned to its previous state. The whole algorithm is repeated a large number of times to ensure that the system reaches the equilibrium state.

The energy of the system is calculated taking into account the repulsive interparticle interaction as well as the surface tension potential which has been chosen to be linear with the distance between the top of the particle and the computational cell surface.

The drying of the solvent is simulated through a stepwise decrease of the computational cell height, a decrease that is performed so that at each step the volume packing fraction of the system $V_{metal}V_{cell}$ increases by a constant amount.

5.3. Easy axis alignment

In order to ensure a maximum signal obtained by the read head, efforts are made to align the easy axis of the particles to the read-write direction by using a strong magnetic field. However, when particles are very small thermal agitation can impose significant limits to this alignment process as.

The model previously described was used to analyse the conditions that must be met in order to obtain a significant degree of alignment in a suspension of FePt particles and the results are being compared with a thermodynamic equilibrium analysis of such systems. The degree of alignment can be expressed as the "squareness" of the particle assembly, i.e. the average component of the easy axis orientation that is along the direction of the applied magnetic field. For a completely aligned system the squareness is 1.0 while for a completely misaligned one its value is 0.5. Considering the coordinate axis in Figure 5-4 this squareness can be expressed as:

$$\langle|\cos\theta|\rangle = \langle|\cos\alpha\cos\beta - \sin\alpha\sin\beta\cos\varphi|\rangle \tag{5.13}$$

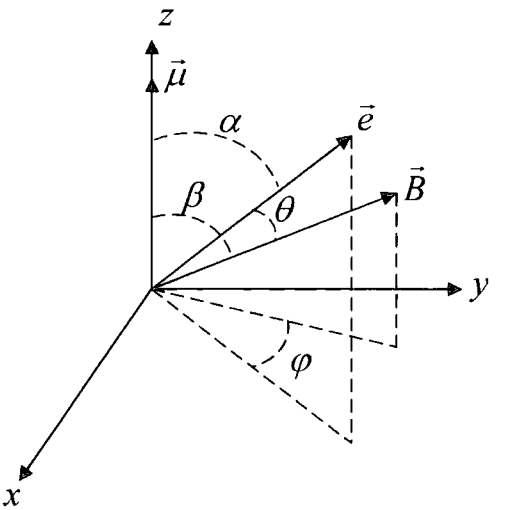

Figure 5-4. Orientation axis and angle notation for a particle in colloidal state

At thermal equilibrium, the energies of the particles will have a Boltzmann distribution. Thus, considering that a system of non-interacting particles with magnetic moment $\vec{\mu}$ easy axis orientation $\vec{e}$, volume V and anisotropy constant K is under the effect of an external applied magnetic field $\vec{B}$, the average value of a function $f(\alpha,\beta,\varphi)$ can be expressed as

$$\langle f \rangle = \frac{\int_0^{\pi}\int_0^{\pi}\int_0^{2\pi} f \exp\left(-\frac{KV}{k_B T}\sin^2\alpha\right)\exp\left(\frac{\mu \mathrm{B}}{k_B T}\cos\beta\right)\sin\alpha\sin\beta\, d\alpha\, d\beta\, d\varphi}{\int_0^{\pi}\int_0^{\pi}\int_0^{2\pi} \exp\left(-\frac{KV}{k_B T}\sin^2\alpha\right)\exp\left(\frac{\mu \mathrm{B}}{k_B T}\cos\beta\right)\sin\alpha\sin\beta\, d\alpha\, d\beta\, d\varphi} \tag{5.14}$$

With the notations

$$a = \frac{KV}{k_B T} \text{ and } b = \frac{\mu B}{k_B T} \tag{5.15}$$

the expression for the squareness of the system becomes [87]

$$\langle |\cos\theta| \rangle = \frac{1}{I}\int_0^{\pi}\int_0^{\pi}\int_0^{2\pi} |\cos\alpha\cos\beta + \sin\alpha\sin\beta\cos\phi| \cdot \cdot \exp(-a\sin^2\alpha + b\cos\beta)\sin\alpha\sin\beta\, d\alpha\, d\beta\, d\varphi \tag{5.16}$$

with

$$I = \int_0^{\pi}\int_0^{\pi}\int_0^{2\pi} \exp(-a\sin^2\alpha + b\cos\beta)\sin\alpha\sin\beta\, d\alpha\, d\beta\, d\varphi \tag{5.17}$$

or, separating terms and using the substitutions $\cos\alpha = t$, $\sin^2\alpha = 1-\cos^2\alpha$ and $\cos\beta = x$

$$I = 2\pi\exp(-a)\frac{\exp(b)-\exp(-b)}{b}\int_{-1}^{1}\exp(at^2)dt \tag{5.18}$$

The presence of the absolute value function in expression (5.16) makes impossible the analytical evaluation of the integral but numerical techniques can be used to obtain an estimate of its value. An easier approach is to evaluate the alignment in the system by using

$$\langle \cos^2\theta \rangle = \frac{1}{I}\int_0^{\pi}\int_0^{\pi}\int_0^{2\pi} (\cos\alpha\cos\beta + \sin\alpha\sin\beta\cos\phi)^2 \cdot \cdot \exp(-a\sin^2\alpha + b\cos\beta)\sin\alpha\sin\beta\, d\alpha\, d\beta\, d\varphi \tag{5.19}$$

which can be expressed as:

$$\left\langle \cos^2\theta \right\rangle = \frac{2\pi}{I} F(b)\exp(-a)\int_{-1}^{1} t^2 \exp(at^2)dt + \frac{\pi}{I}\left(\frac{2}{b}\sinh b - F(b)\right)\exp(-a)\int_{-1}^{1}(1-t^2)\exp(at^2)dt \tag{5.20}$$

with

$$F(b) = \frac{2}{b}\sinh b - \frac{4}{b^2}\cosh b + \frac{4}{b^3}\sinh b \tag{5.21}$$

The expressions (5.16) and (5.20) can be numerically calculated for given values of the parameters a and b to find the alignment parameter of the system in certain conditions.

These statistical results have been compared with the values obtained by simulations performed on large particle systems (more than 10000 particles) in which the magnetic interparticle interaction is not taken into account. Figure 5-5 and Figure 5-6 show a good agreement between the values obtained by the two methods both for $\langle|\cos\theta|\rangle$ and $\langle\cos^2\theta\rangle$.

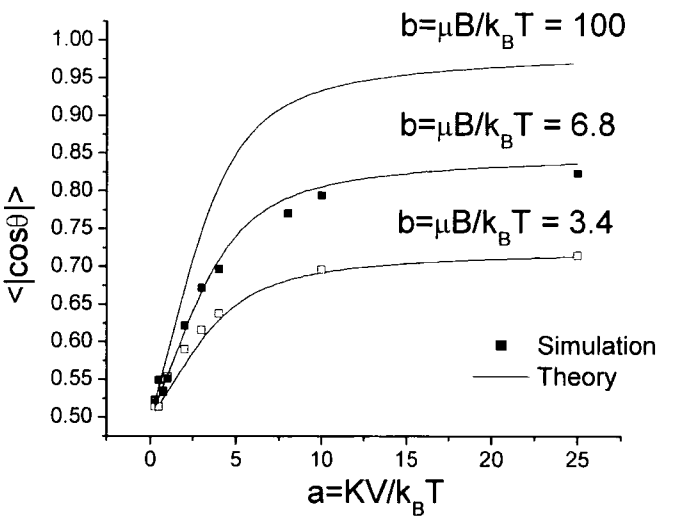

Figure 5-5. Variation of <|cosθ|> with parameters *a* and *b*

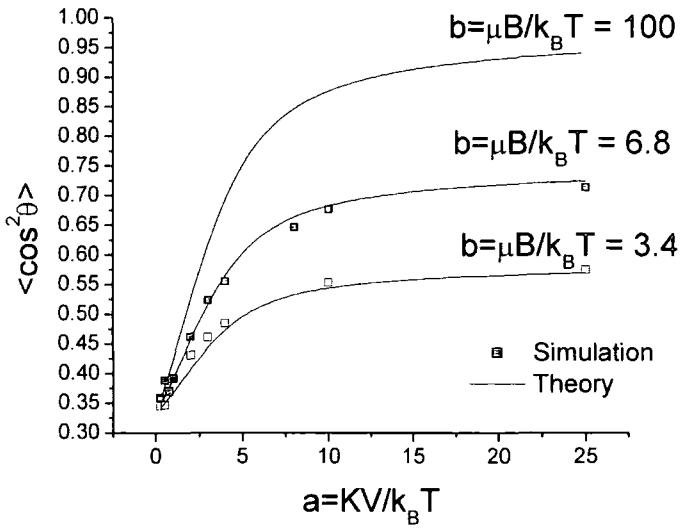

Figure 5-6. Variation of $\langle\cos^2\theta\rangle$ with parameters a and b

The results were obtained for systems of particles with average diameter of $3nm$, with a saturation magnetization of $500emu/cc$ at a temperature of $300K$. The first set of results was obtained for an external applied magnetic field of $20kOe$ which corresponds to a value of the b parameter of 3.4. The field value for the second set of results was $40kOe$ corresponding to $b = 6.8$ while thermodynamic results were also obtained for an unrealistic value of $b = 100$ for comparison.

It is obvious that in order to obtain a good easy axis alignment both anisotropy and magnetostatic energies must be at least one order of magnitude larger than the thermal agitation energy. This is due to the fact that the link between the easy axis and the magnetic field is not direct but rather through the orientation of the magnetic moment. So, to align the easy axis to the field direction, the magnetostatic energy must be sufficiently large for the magnetic moments of the particles to follow the direction of the applied field but the anisotropy energy must also be large enough for the easy axis to be able to align to the direction of the moment.

In practical terms, the most obvious way to obtain a better alignment would be to increase the $\frac{V}{T}$ ratio since this is involved in the expression of both a and b. However, other problems may arise due to the fact that by decreasing the temperature at which the alignment process takes place the carrier fluid becomes more viscous while an increase of

the particle size is technologically difficult and it would decrease the limit of the achievable recording density. As in most cases, a compromise must be made between the need to increase the particle size to reduce the thermal effects and the desire to keep it as low as possible for obtaining very high recording densities.

5.4. Critical density

When studying the self-assembly process induced by the drying of the solvent in a droplet of colloidal state FePt nanoparticles, a determining factor is the density of particles in the system. However, what is important is not the initial volume density but rather the final areal density of the configuration assuming that all the particles in the droplet end up in a monolayer. This areal density relates to the average particle-particle distance and thus to the strength of the interaction potential that leads to self-assembly. With the aid of the model, a systematic study on the effect of areal density, particle size dispersion and surfactant interactions. Except where explicitly stated otherwise, the simulations presented here were performed using the interaction potential described in (5.12).

Figure 5-7 shows a system with an particle areal density corresponding to that of a hexagonal structure with surface-to-surface separation larger than twice the surfactant molecule length λ. Because of the thermal agitation particles are uniformly distributed on all available area but there is no evidence of ordering even at local scale. The repulsive interaction potential only occurs when, due to the Brownian motion, the surface-to-surface separation between two particles becomes less than 2λ and the repulsive forces occurring in these cases have random orientation.

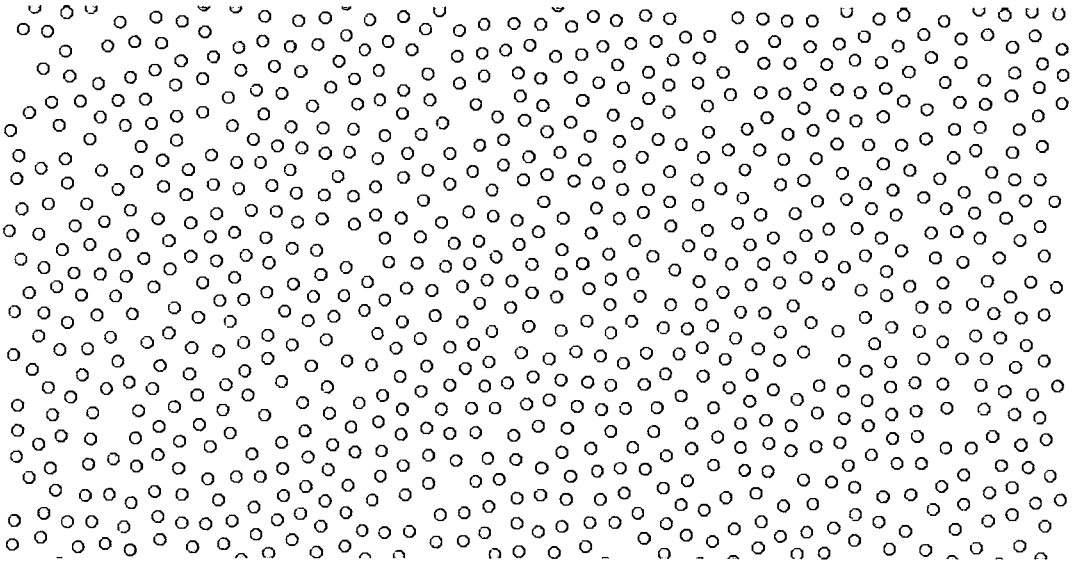

Figure 5-7. Lack of ordering when average interaction potential is weak

When an areal packing density above the critical density corresponding to a hexagonal structure with surface-to-surface separation 2λ is used, a repulsive interaction occurs between most or all of the first-order neighbour particles leading to the local-ordered structure shown in Figure 5-8. However, when the areal density is not much larger than the critical one, the strength of the repulsive forces (i.e. the interaction potential gradient) is not large enough to force long-range order. In this case thermal agitation leads to limited size of the ordered areas.

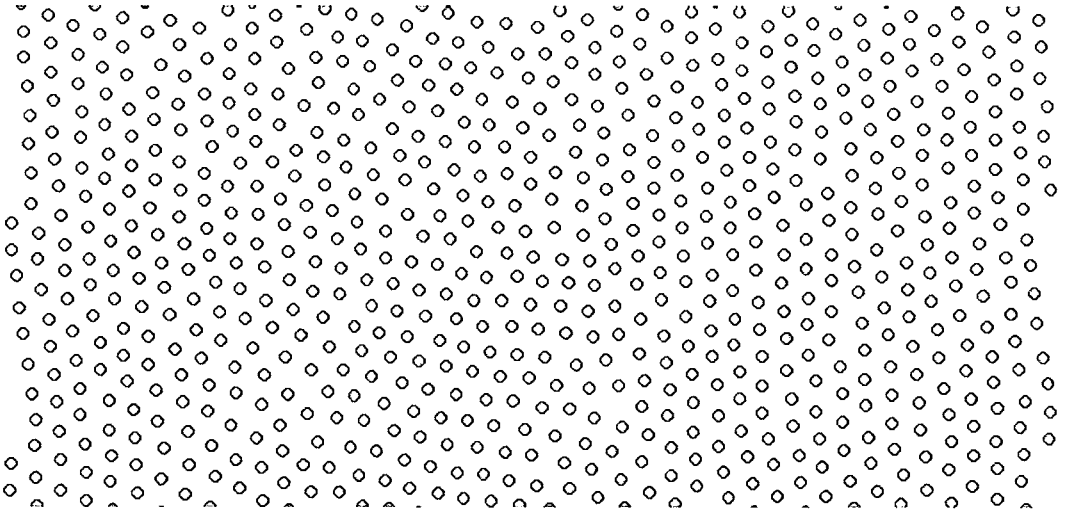

Figure 5-8. Local ordering when average interaction potential is weak

A further increase of the areal density, leading to a considerable increase of the repulsive interaction forces, leads to the formation of wide areas of nearly perfectly ordered particles, as shown in Figure 5-9. However, in order to obtain a particle monolayer of such high density, the surface tension energy must be large enough to overcome the surplus of energy created by pushing all the particles into a single layer.

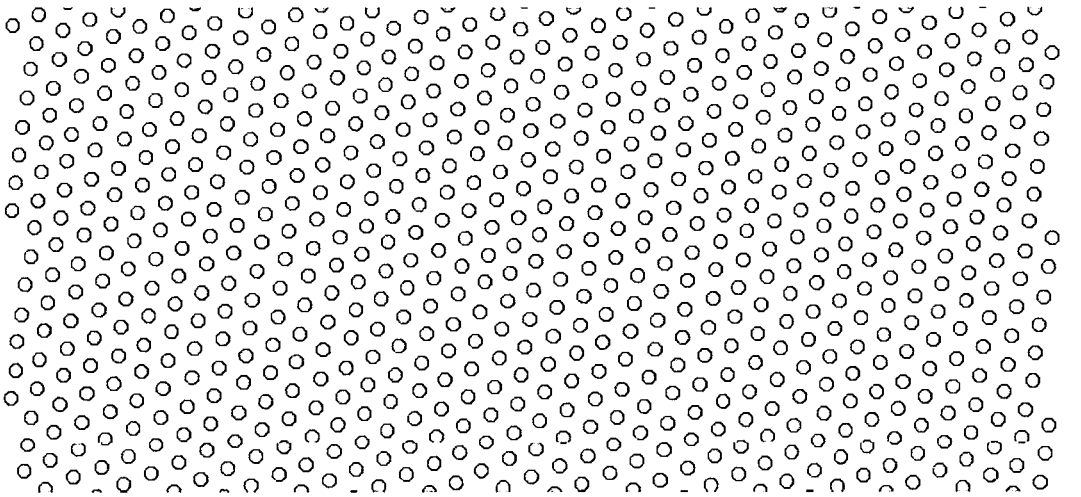

Figure 5-9. Long-range ordering when average interaction potential is strong

Otherwise, when the surface tension is not large enough, it leads to the formation of bilayers or multilayers. Figure 5-10 shows the results obtained for a high density system when the surface tension is not strong enough to push all particles into a monolayer and a bilayer is formed. Figure 5-11 shows only the particles in the bottom layer of the system while Figure 5-12 shows the particles in the top layer.

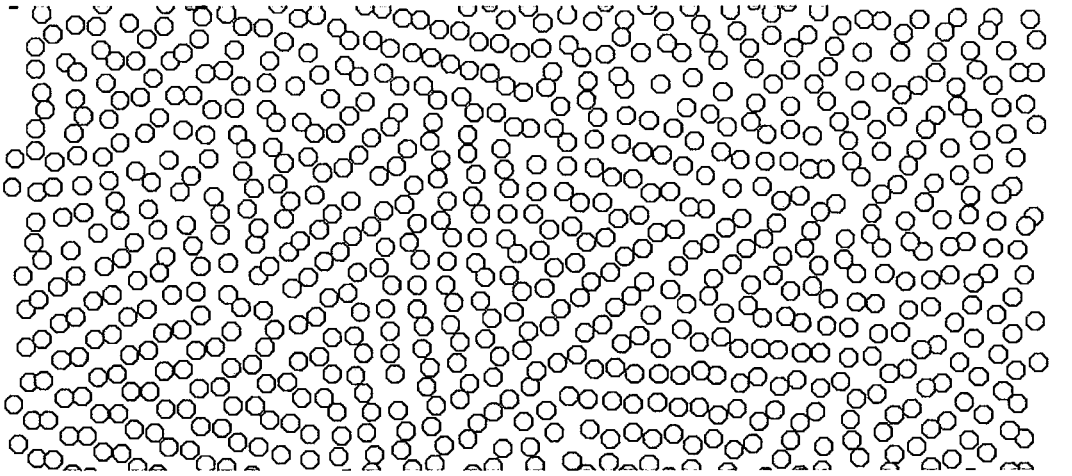

Figure 5-10. Bilayer formed when surface tension cannot overcome repulsion

The bottom layer has a relatively good ordering with some disordered areas that can be ascribed firstly to the fact that the layer density is smaller than that in Figure 5-9. In addition, the interactions with particles in the top layer, which doesn't have perfect order breaks the symmetry of the system.

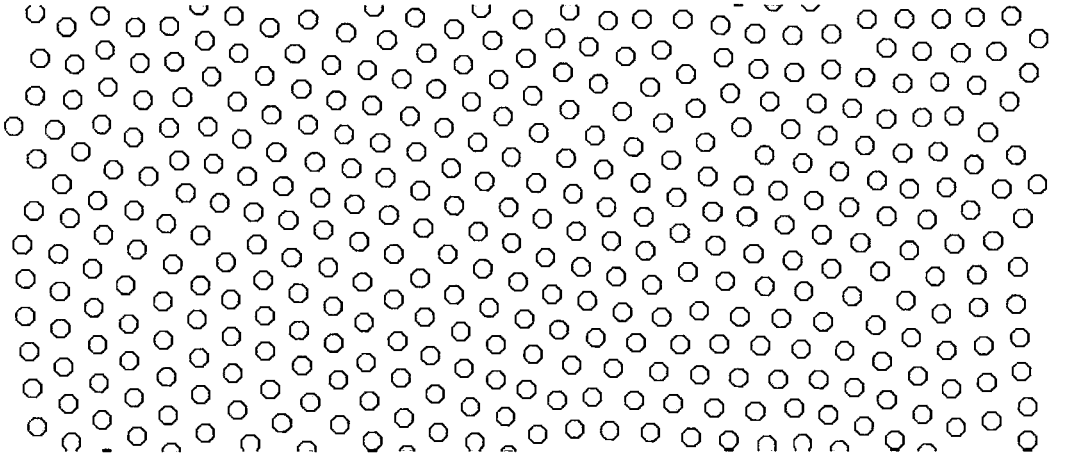

Figure 5-11. Bottom layer ordering

The top layer shown in Figure 5-12 also exhibits some ordering despite the fact that its areal density is way below the critical value. The ordering is produced by the correlation between it and the bottom layer, correlation that is made through the action of the surface tension potential that tries to force the top layer particles to the lowest position possible, i.e. above the interstitial spaces of the bottom layer. The correlation is revealed by the same orientation of the particle rows in both layers and by the fact that the highest degree of ordering is seen in the areas where the top layer has the highest areal particle density.

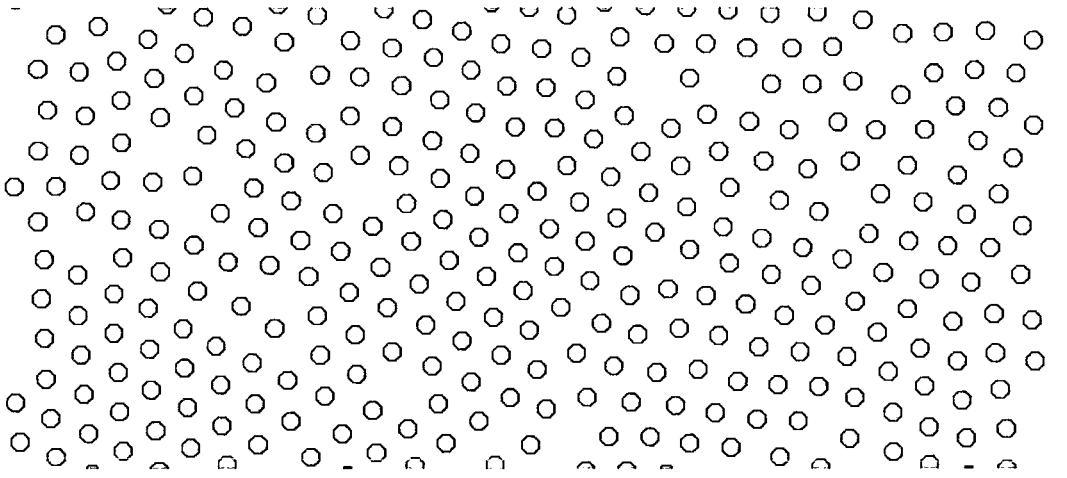

Figure 5-12. Top layer ordering

5.5. *Size distribution effect*

The simulations performed at densities above the critical density but below the values that lead to multilayer formation for a given strength of the interaction potential and surface tension show that it is possible to obtain near perfect ordering over large areas as shown in Figure 5-13. Such perfect ordering has been observed experimentally [88] as shown in Figure 5-14.

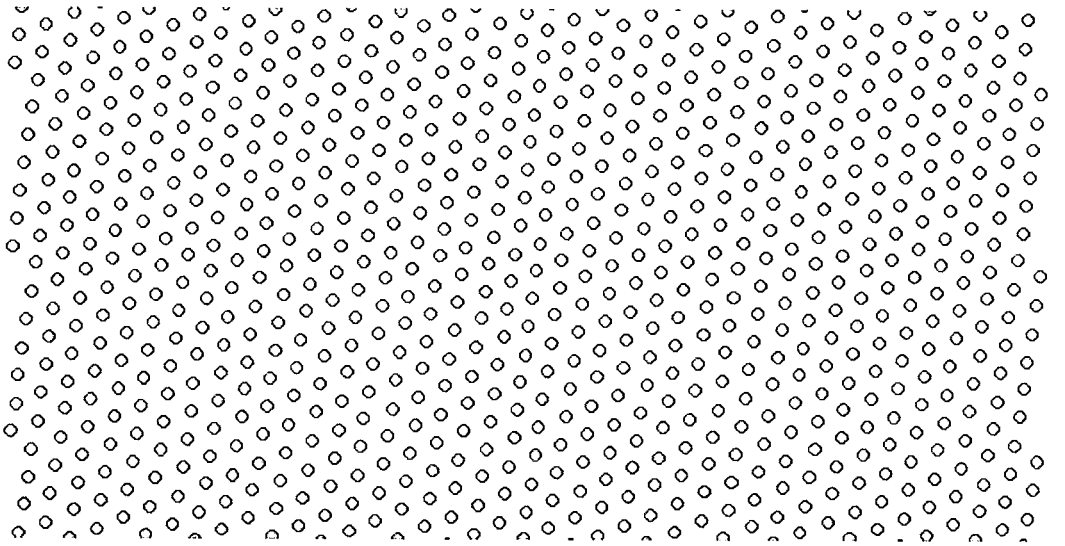

Figure 5-13. Near perfect ordering obtained for a system with no particle size distribution

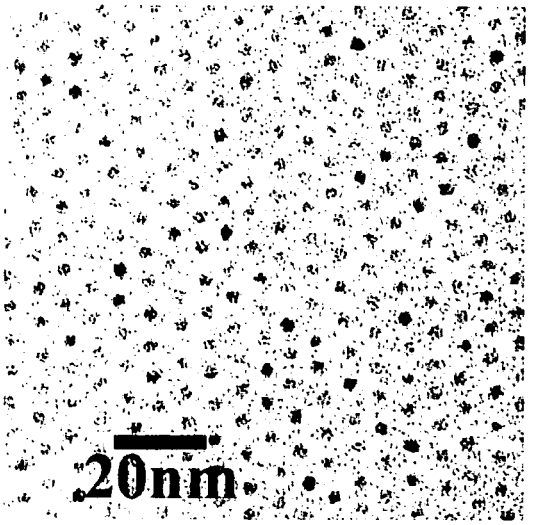

Figure 5-14. TEM image of a near perfect ordered system with no particle size distribution

However, in these initial simulations no particle size distribution was taken into account. Also, even if experimentally is quite difficult to accurately estimate the particle size distribution, the image in Figure 5-14 intuitively shows a very narrow particle size distribution. This is not the case for the experimental sample [88] shown in Figure 5-15 where a broader size distribution led to formation of a system with local but no long-range order.

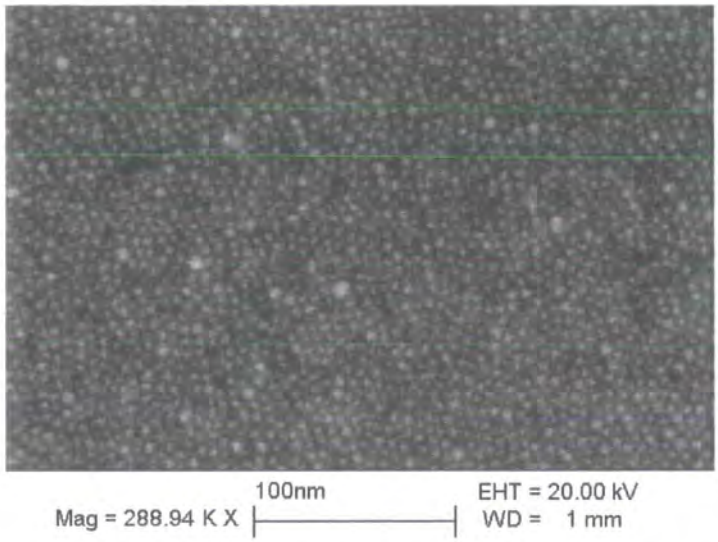

Figure 5-15. SEM image of a system with particle size distribution exhibiting only local order

It became clear that the width of the particle size distribution plays an important role in the self-assembly process. The effect is evident in Figure 5-16 where it can be seen that, although the distance between the surfaces of the particles d_s is almost constant, approximately equal to twice the surfactant molecule length, the particle centre separation is larger in the case of the larger particles (d_1) than in the case of the smaller ones (d_2).

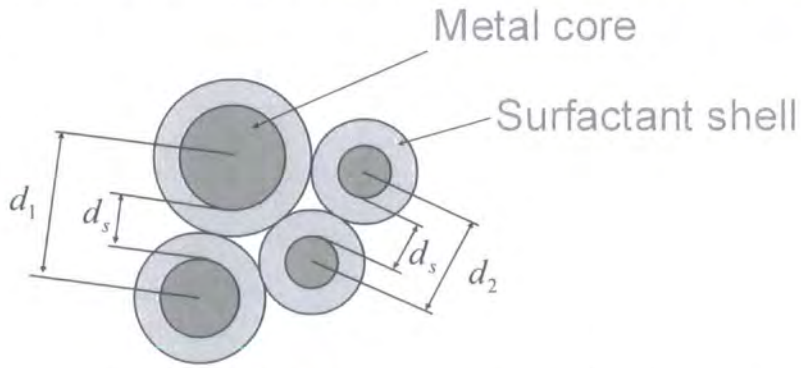

Figure 5-16. Influence of particle size on particle separation

In order to see just how important keeping a narrow size distribution is in the process of obtaining wide areas of self-assembled particles, a set of simulations was performed under identical conditions but using standard deviations of particle diameter in the range [0…0.2]. Some representative results are presented below.

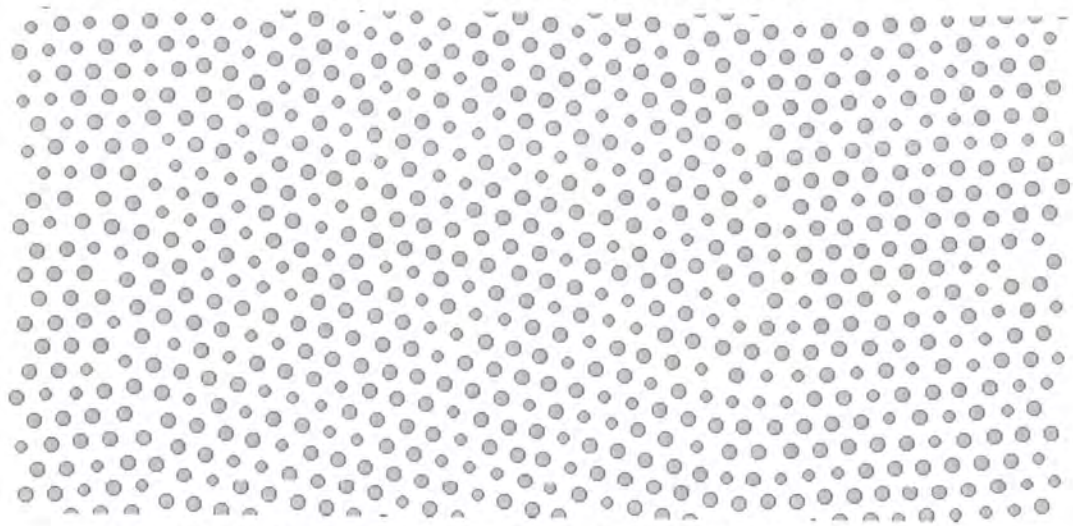

Figure 5-17. System obtained using a 0.05 standard deviation of particle diameter

Figure 5-17 shows that, when a standard deviation of particle diameter of 0.05 is used, there are still large self-assembled areas separated by grain boundaries, the row orientation changing from one self-assembled area to the other. The grain boundaries are generally formed when particles of "extreme" size come in contact, i.e. a row of predominantly large particles is in contact with a row of small ones.

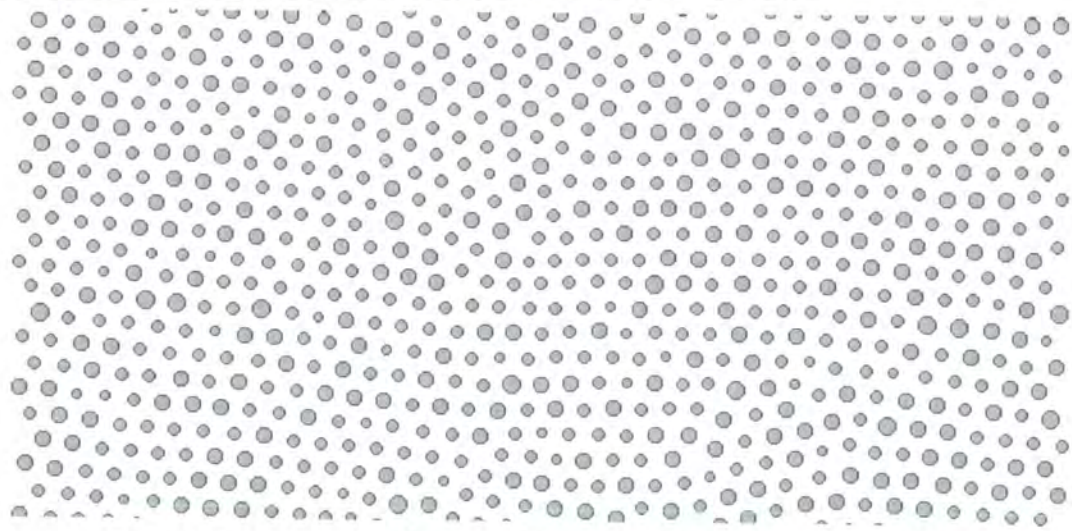

Figure 5-18. System obtained using a 0.10 standard deviation of particle diameter

When the standard deviation of particle diameter is further increased to 0.10 (see Figure 5-18) the particle arrays become curved while for even larger values of the standard deviation the long-range ordering is lost, as shown in Figure 5-19, a situation similar to the experimentally observed one in Figure 5-15

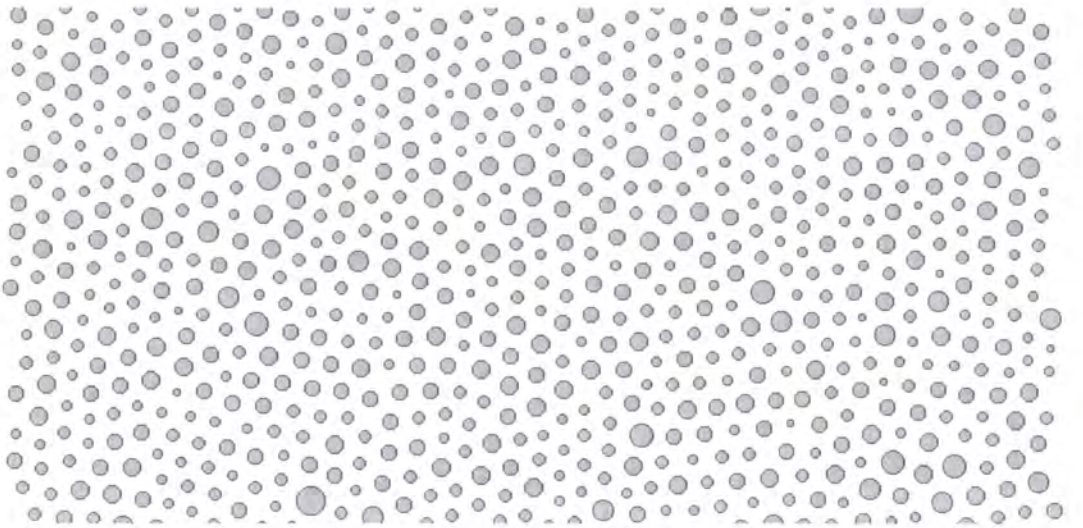

Figure 5-19. System obtained using a 0.20 standard deviation of particle diameter

A large number of simulations show that the upper limit of the diameter standard deviation so that large self-assembled areas can still be obtained is around 0.05.

5.6. *Attraction potential*

The simulations performed so far showed that in order to be able to obtain wide self-assembled areas two conditions must be met: the areal particle density must be above a critical value but below a value leading to multilayer formation and the particle size distribution must be very narrow. The first condition in particular is required even in order to obtain local particle ordering since, as shown in Figure 5-7, an areal density below the critical value leads to a total loss of ordering. However, experimentally [88] it has been observed that in certain conditions local self-assembly occurs even if the overall areal density of particles is below the critical value (Figure 5-20).

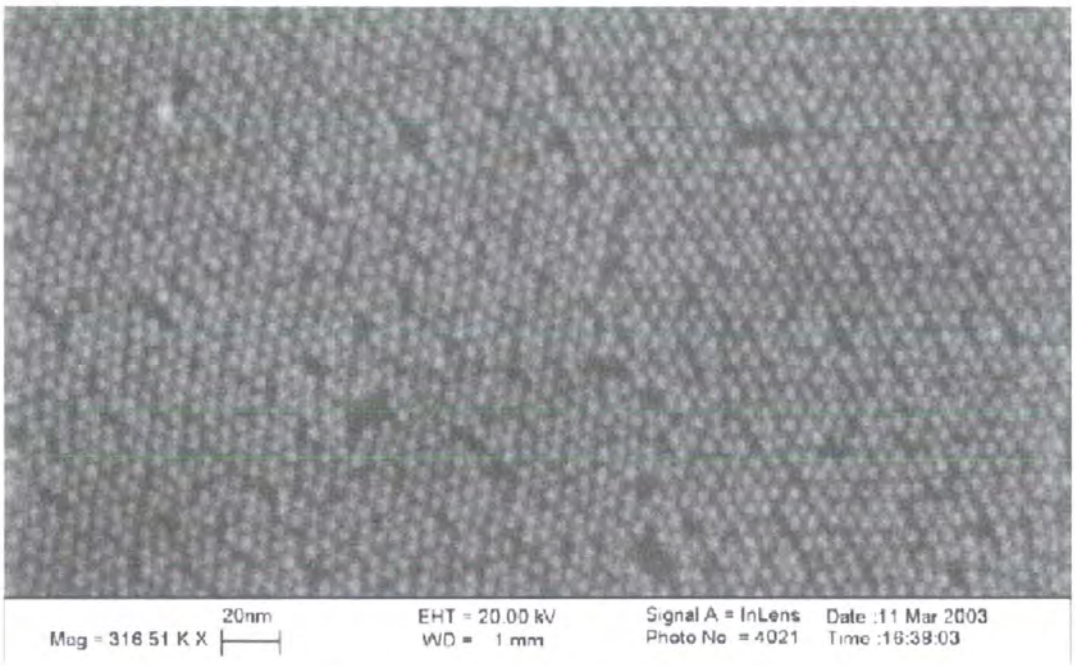

Figure 5-20. Self-assembly in systems with low overall particle density

This is indirect evidence of the fact that some kind of attractive force occurs between particles in specific conditions. If there were no attraction, the particles would tend to uniformly occupy all available space and not self-order, as shown in Figure 5-7.

To validate this hypothesis, attraction term was added to the interaction potential (see Figure 5-21), so that the total energy would have a minimum when the surface-to-surface separation between two particles is 2δ, with δ being the surfactant molecule length.

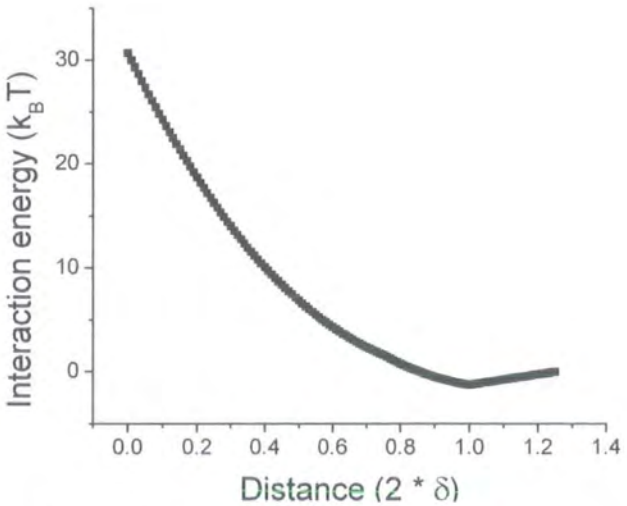

Figure 5-21. Interaction energy with attraction term

Results of simulations performed with this form of the potential, shown in Figure 5-22 reproduce quite well the results seen experimentally in Figure 5-20.

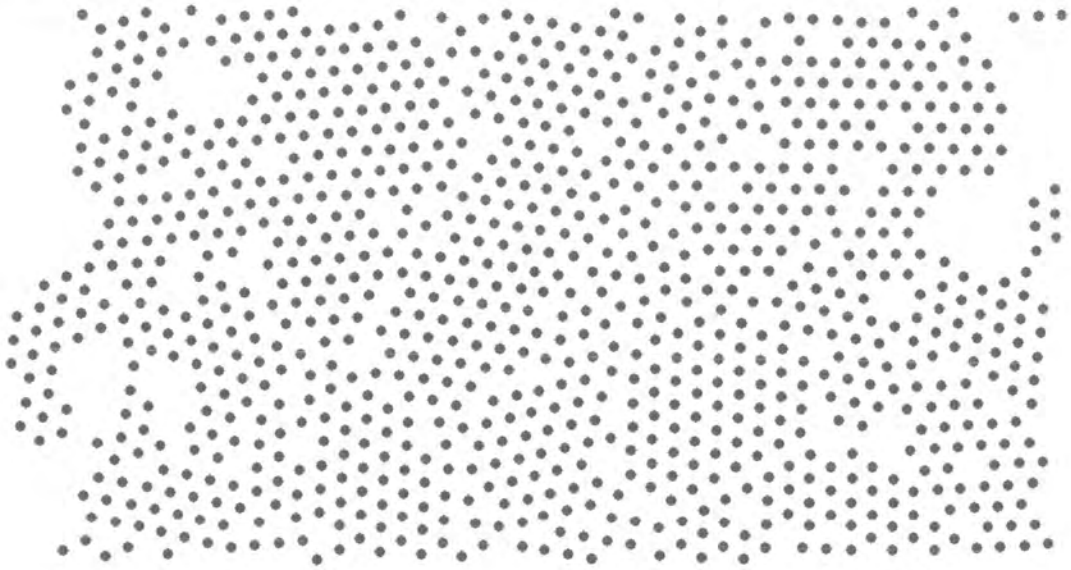

Figure 5-22. Drying simulation using attraction potential

However, this form for the interaction potential also leads to aggregation of particles in the colloidal state (Figure 5-23), an effect that is not experimentally observed.

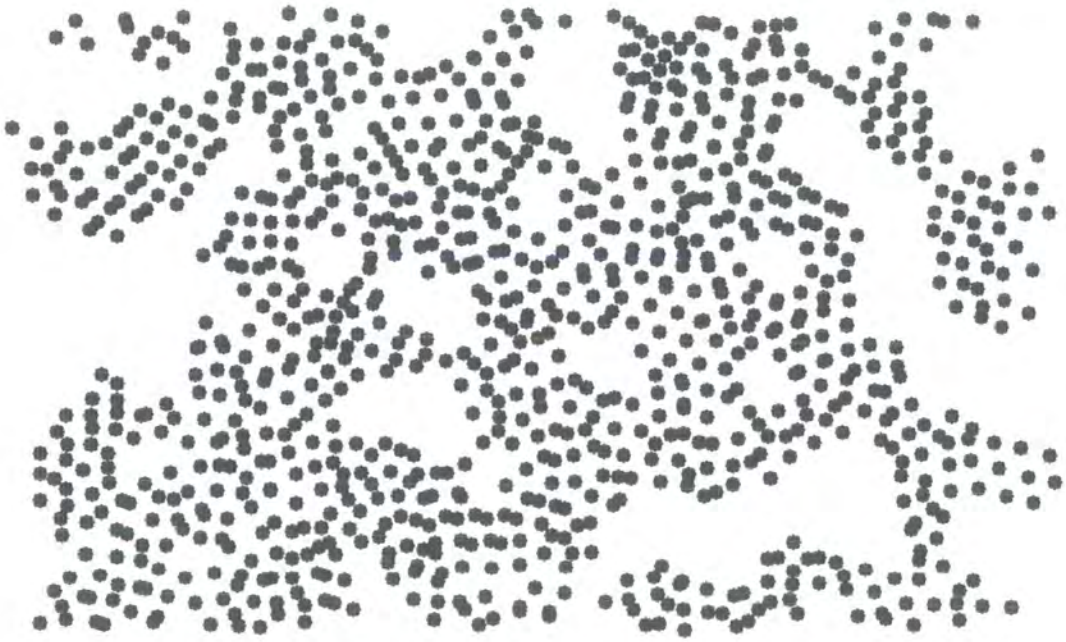

Figure 5-23. Particle aggregation in colloidal state due to attraction interaction

Also, experimentally it is observed that the surface-to-surface separation in the self-assembled systems is not 2δ as it would be expected from the considered shape of the interaction potential but rather δ.

To explain both the decrease in surface-to-surface separation and the lack of aggregation between particles in the colloidal state a new interaction potential was proposed, a potential in which attraction occurs only if there is some overlap between the surfactant molecules attached to the particles. This behaviour may be due to dipole interaction between the surfactant molecules. As seen in Figure 5-24, the interaction between the two dipoles acts as repulsion if the particles are separated by a distance larger than twice the surfactant molecule length but it acts as attraction if the distance becomes less than two molecule lengths.

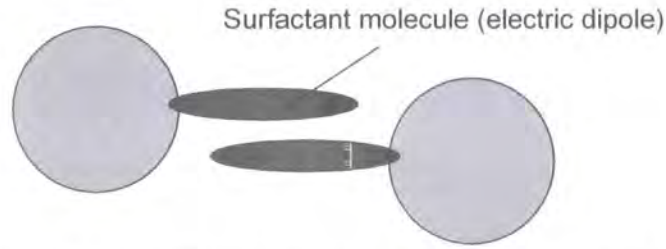

Figure 5-24. Dipolar interactions can act as attraction between particles

The interaction potential was chosen empirically, as a polynomial function of particle surface-to-surface separation, and it is a superposition of a repulsion potential $R(x)$ and an attraction one $A(x)$. The conditions they have to fulfil are that $R(2\delta) = A(2\delta) = A(0) = 0$, $R'(2\delta) = A'(2\delta) = A'(0) = 0$ so that the transition from a non-interacting separation $d_1 > 2\delta$ to an interacting separation $d_2 < 2\delta$ is smooth.

With these conditions, the two polynomials have been found to be of the form:

$$R(x) = C_R\left(\left(1-\frac{x}{2\delta}\right)^{r_1} + \left(1-\frac{x}{2\delta}\right)^{r_2}\right),\ x \in (0, 2\delta)$$

(5.22)

$$A(x) = -C_A\left(\frac{x}{2\delta}\left(1-\frac{x}{2\delta}\right)\right)^{a},\ x \in (0, 2\delta) \qquad (5.23)$$

with C_R and C_A two interaction strength coefficients while r_1, r_2 and a choose how rapidly the potential varies with distance. For simulations, the values $r_1 = 12$, $r_2 = 2$ and $a = 12$ were used and the values of C_R and C_A were varied to change the strength of interactions. For the particular values $C_R = 1 \times 10^3$ and $C_A = 4 \times 10^9$ the interaction potential has the shape in Figure 5-25.

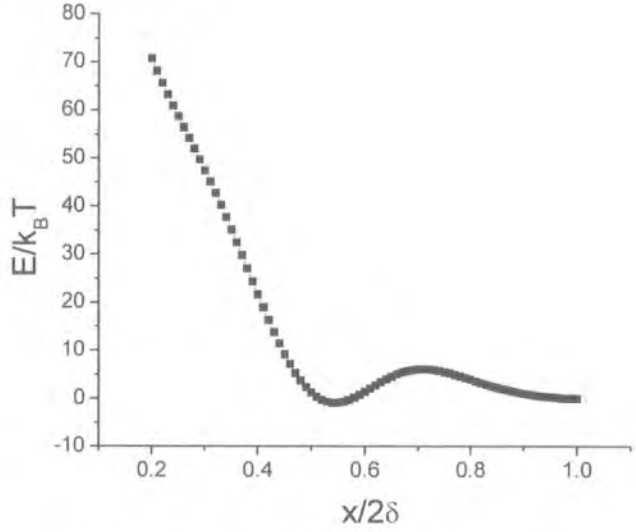

Figure 5-25. Empirical interaction potential

This interaction potential exhibits an initial repulsive energy barrier of the order of $10k_BT$ that is sufficient to keep the particles separated in the colloidal state. When the drying process starts, the extra energy brought by the surface tension can overcome this initial energy barrier so that the interaction becomes of an attractive nature.

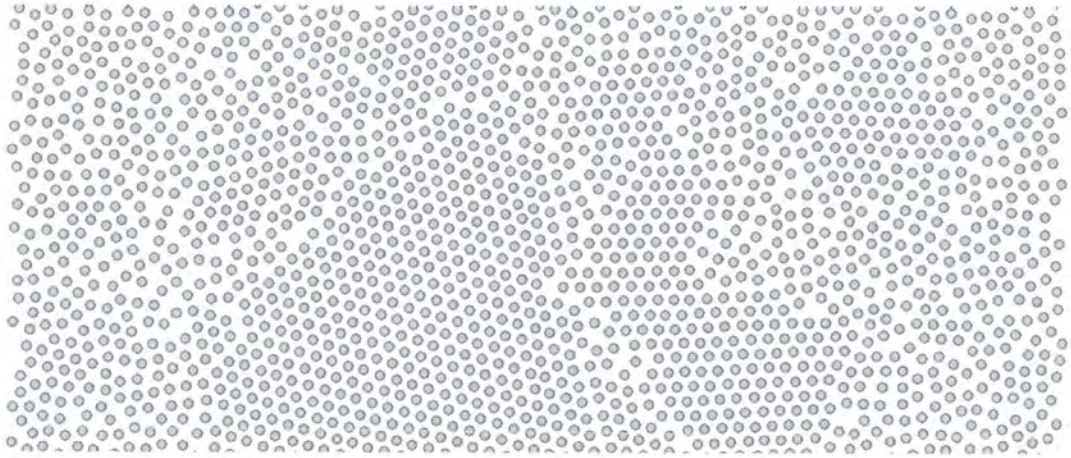

Figure 5-26. Effect of attraction potential on a low density system

Simulations performed using this type of potential show, in certain conditions, a behaviour similar to that experimentally observed in Figure 5-20.

As Figure 5-26 shows, when the empirical potential including attraction is used for a system with areal particle density well below the critical density, depending on the initial random position of particles in the systems, locally the density may become strong enough to overcome the initial repulsion leading to self-assembly formation with average particle separation around one surfactant molecule length. In the surrounding areas, the local density of particles becomes smaller than the average so that no ordering is observed, the particles being evenly distributed.

For a system (Figure 5-27) that would be above the critical density when not using the attraction part of the interaction potential the effect is that, once the initial repulsion barrier is overcame, the attraction brings particles closer together than they would normally be with a repulsive-only potential, leaving gaps between the self-assembled areas, similar to the results shown in Figure 5-20.

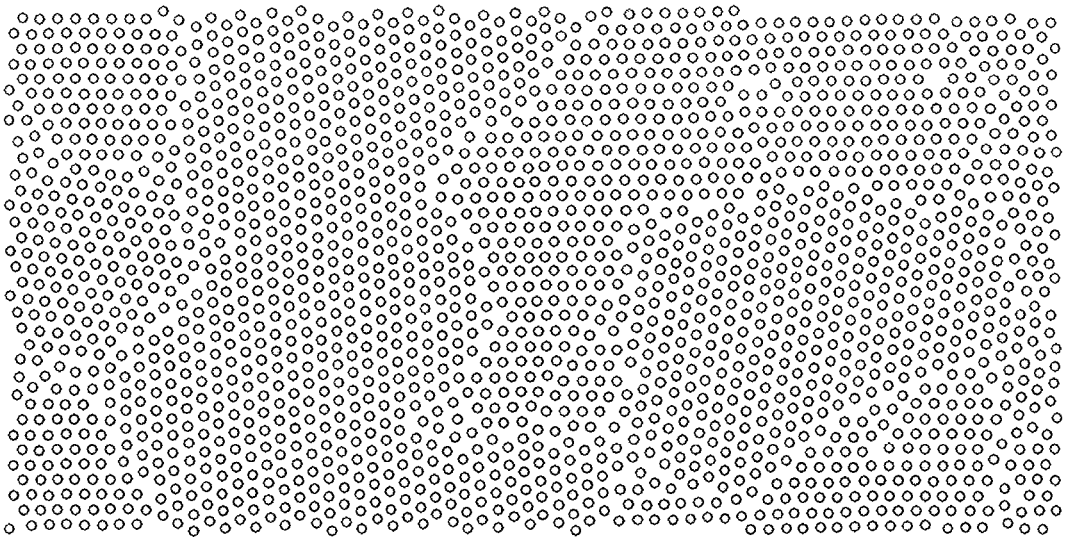

Figure 5-27. Effect of attraction potential on a high density system

5.7. *Square lattices*

Simulations performed on system with densities above the critical density for self-assembly formation can lead, depending on the ratio between the surface tension energy and the interparticle interaction energy, to formation of multilayers. However, in many

cases (Figure 5-28, Figure 5-29), in the bilayer areas the FePt particles assembled in a square lattice rather than the expected hexagonal one.

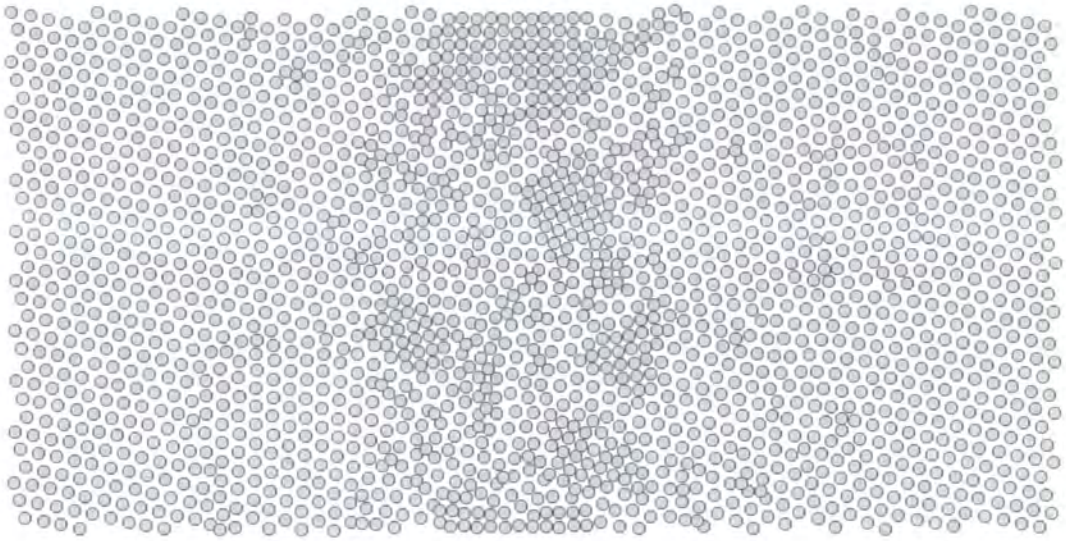

Figure 5-28. System with bilayers having square structure

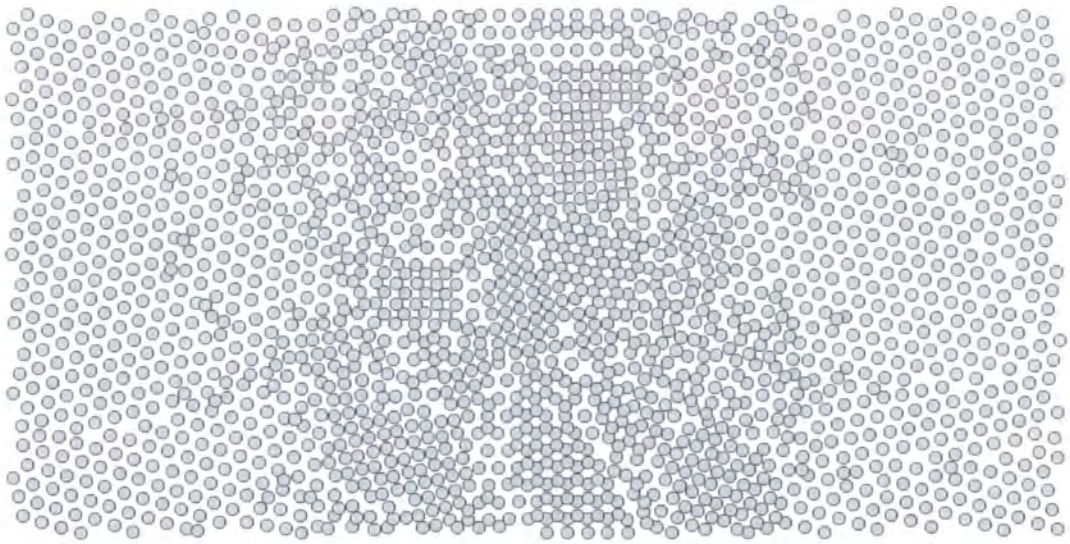

Figure 5-29. System with bilayers having both hexagonal and square structure

Similar results have been found experimentally [86] (Figure 5-30) and the initial explanation for this behaviour was that for the areas with bilayers, the surface tension energy would have a very important contribution and, in order to minimize its value, the particles would tend to assembly in a presumably higher energy square lattice but thus allowing the top layer to stay at a lower height, thereby decreasing the surface tension energy and the overall total energy of the bilayer.

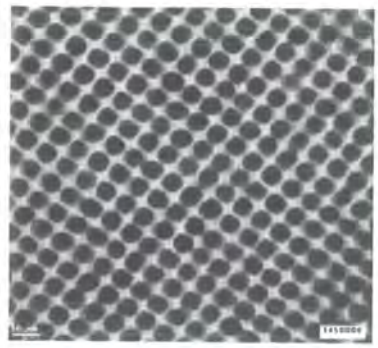

Figure 5-30. TEM image of a multilayer FePt particle system with square lattice

For the simulations shown in Figure 5-28 and Figure 5-29, the phenomenological interaction potential described earlier with both an attractive and repulsive term has been used. Since in none of the simulations performed without the attraction part of the potential a square lattice was observed there was a question of how important the effect of the attraction was in producing this type of ordering. To evaluate the effect of the attraction part of the interaction potential on this behaviour, simulations have been performed with only the repulsive term on. Surprisingly, for a system with the same areal density of particles as the one in Figure 5-28, leaving out the attraction term for the potential led to the formation of an almost perfectly ordered, densely packet single layer with a square lattice, as shown in Figure 5-31.

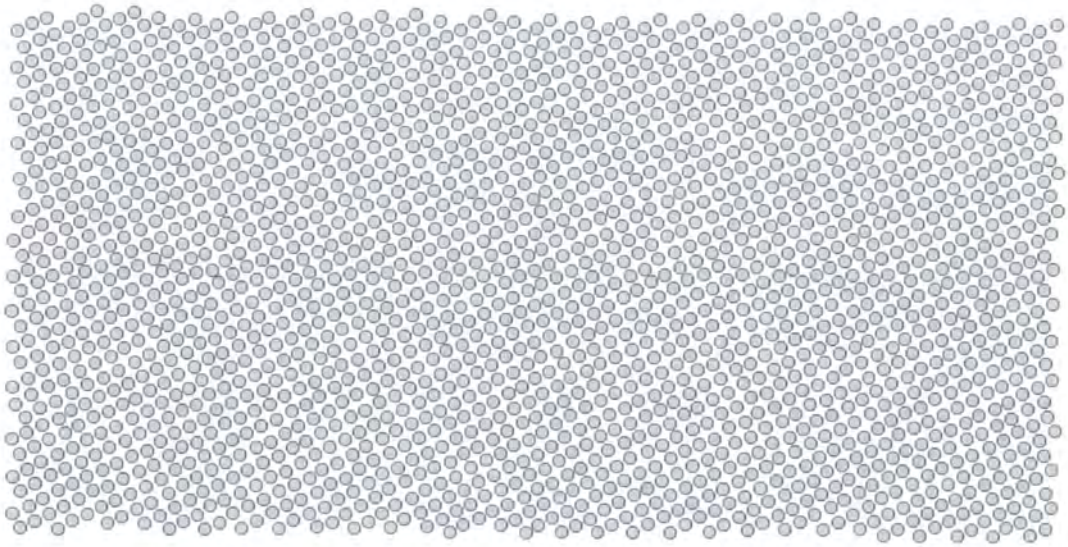

Figure 5-31. In the absence of attraction, square lattice ordering is observed for systems with high areal densities

This led to the conclusion, that a different explanation for obtaining square lattice was needed as in the case of a monolayer the effect of the surface tension is almost identical for all particles and cannot be responsible for the formation of square lattices.

Since the Monte-Carlo model finds the energy minimum of a system, a comparison between the interaction energy corresponding to one particle in a perfect square and hexagonal lattice respectively is needed in order to explain the conditions under which the square lattice forms.

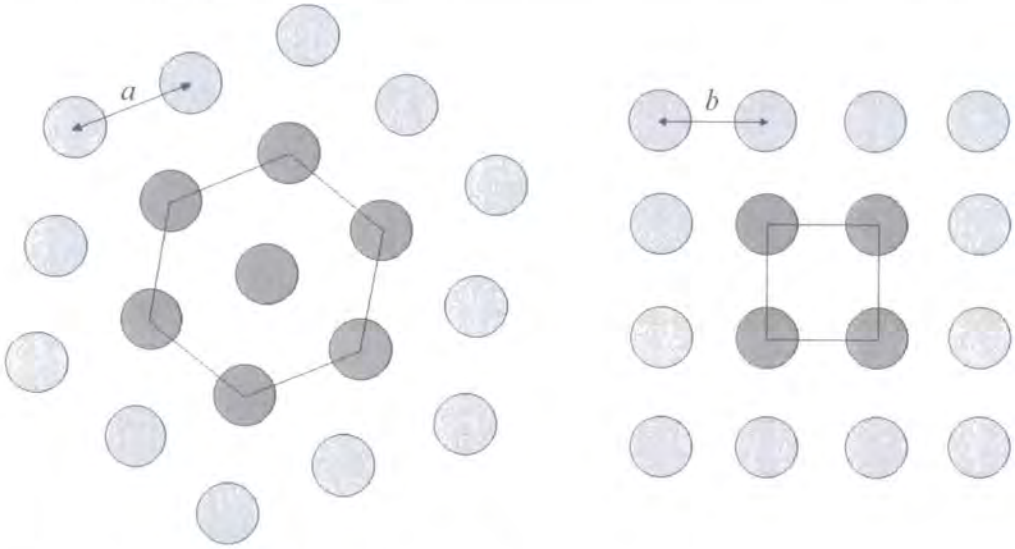

Figure 5-32. Hexagonal (left) and square (right) lattice with parameters *a* and *b* respectively

For a hexagonal structure with lattice parameter a as shown in Figure 5-32, the number of particles in a unit cell is

$$N_{Hex} = 1 + 6 \cdot \frac{1}{3} = 3 \tag{5.24}$$

the unit cell area

$$S_{Hex} = 6 \cdot \frac{1}{2} \cdot a \cdot a \frac{\sqrt{3}}{2} = a^2 \frac{3\sqrt{3}}{2} \tag{5.25}$$

with the areal density

$$\sigma_{Hex} = \frac{N_{Hex}}{S_{Hex}} = \frac{2}{a^2 \sqrt{3}} \tag{5.26}$$

Considering that the interaction energy between two particles is evenly distributed among them, the interaction energy for a single particle is half of the sum of the interaction energies with all the other neighbouring particles:

$$W_{Hex} = \frac{1}{2} 6 \cdot E(a) = 3E(a) \tag{5.27}$$

with $E(x)$ being the interaction potential as a function of the interparticle distance.

For a square structure with lattice parameter b (Figure 5-32), the number of particles in a unit cell is:

$$N_{Sqr} = 4 \cdot \frac{1}{4} = 1 \tag{5.28}$$

with a unit cell area

$$S_{Sqr} = b^2 \tag{5.29}$$

and an areal density

$$\sigma_{Sqr} = \frac{N_{Sqr}}{S_{Sqr}} = \frac{1}{b^2} \tag{5.30}$$

The interaction energy for a single particle is given by the interaction with first order and second order neighbours:

$$W_{Sqr} = \frac{1}{2}\left(4 \cdot E(b) + 4 \cdot E\left(b\sqrt{2}\right)\right) = 2 \cdot E(b) + 2 \cdot E\left(b\sqrt{2}\right) \tag{5.31}$$

In order for the two structures have the same areal density the condition

$$\frac{1}{b^2} = \frac{2}{a^2\sqrt{3}} \Rightarrow b = a\sqrt[4]{\frac{3}{4}} \tag{5.32}$$

is needed. This way, the energy ratio between the two cases can be expressed as:

$$\frac{W_{Hex}}{W_{Sqr}} = \frac{3 \cdot E(a)}{2\left(E(b) + E\left(b\sqrt{2}\right)\right)} \tag{5.33}$$

One structure is more favourably formed than the other depending on the ratio between $E(a)$ and $E(b) + E\left(b\sqrt{2}\right)$ with b given by the equal areal density condition.

The ratio between the interaction energies for the empirical repulsive potential used in the simulation depends on the areal density of particles as shown in Figure 5-33:

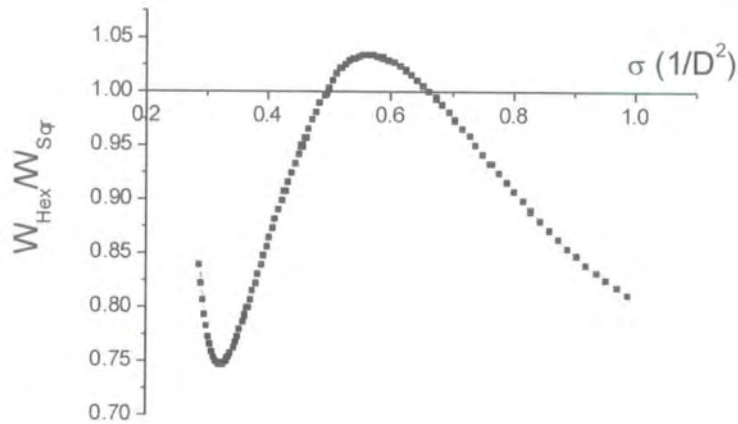

Figure 5-33. Ratio between hexagonal and square lattice repulsion energies vs. areal packing density

These results show that there is a range of values (from 0.50 to 0.66) for which the hexagonal lattice has higher energy than the square one so, when systems with packing densities in that range are produced, they should exhibit square lattice ordering rather than hexagonal ordering.

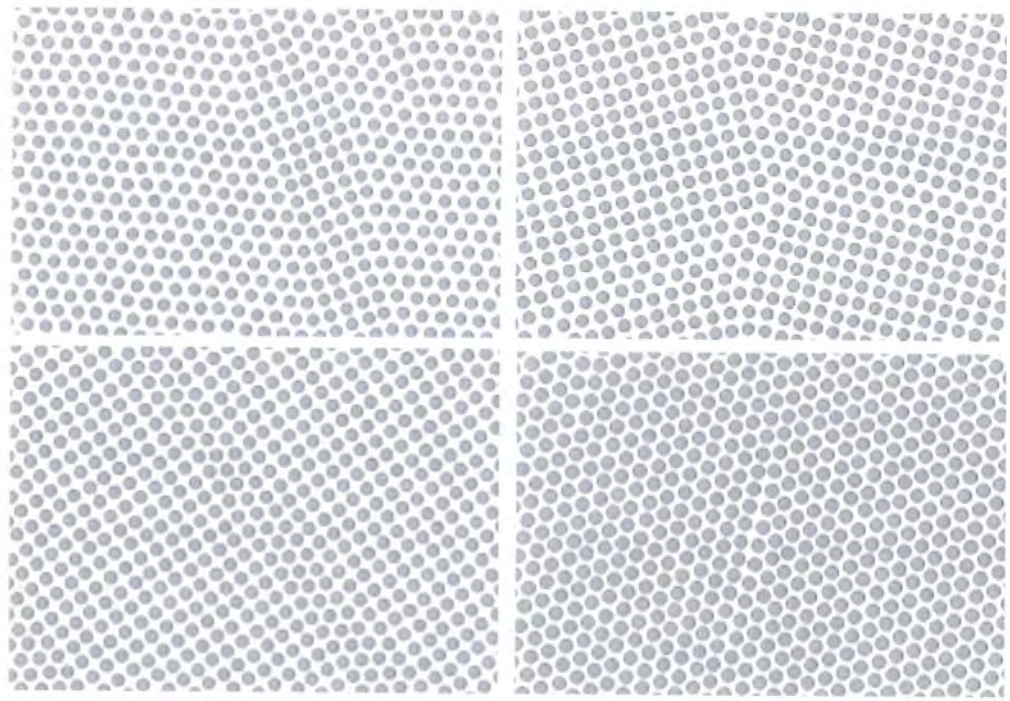

Figure 5-34. Configurations obtained for packing densities of 0.48 (top-left), 0.51(top-right), 0.65 (bottom-left) and 0.68 (bottom-right) showing transition from hexagonal to square and back to hexagonal lattice.

The results were confirmed by simulations performed at packing densities around the limits of the areal density interval for which square lattice should form. As shown in Figure 5-34 at a packing density of 0.48 the particles order mainly in a hexagonal lattice while when the density is increased to just 0.51 the square lattice becomes predominant. Again, for a packing density of 0.65 the square lattice is formed while when the packing density increases to 0.68, just above the second transition point in the energy ratio plot, the particles order in an almost perfect hexagonal structure.

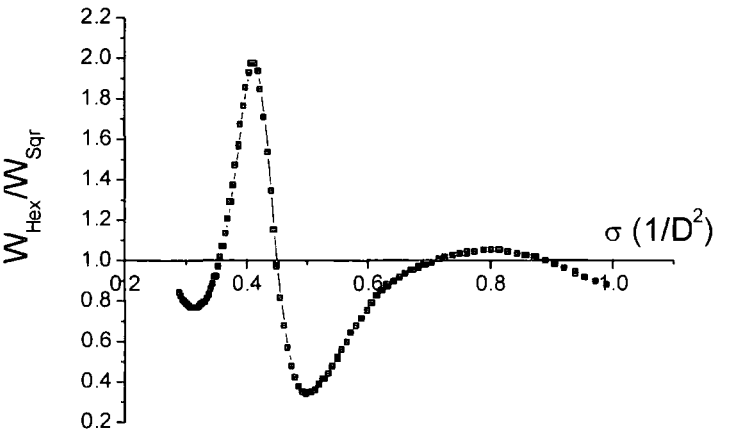

Figure 5-35. Ratio between hexagonal and square lattice total energies vs. areal packing density

If the attraction term is also included, the energy ratio takes the more complicated form in Figure 5-35. There are two regions in which the square lattice has lower energy, one of which is at a lower packing density, which is probably the reason why the first simulations to show square lattice formation were for systems with the attraction term added to the interaction potential.

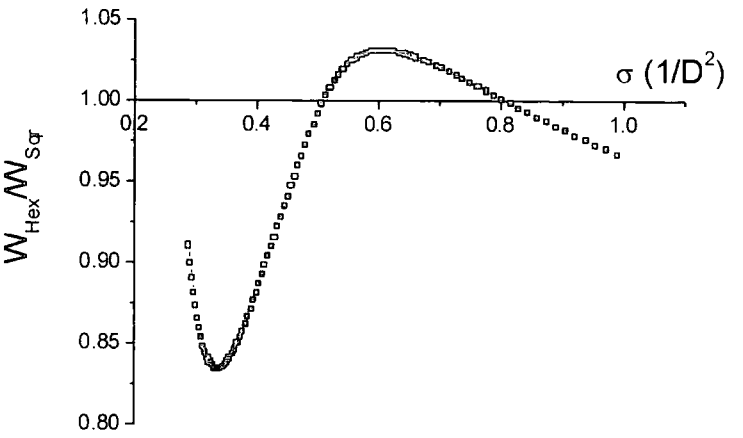

Figure 5-36. Ratio between hexagonal and square lattice entropic repulsion energies vs. areal packing density

For the case when interactions are described by the entropic repulsion term in (5.12) the energy ratio has the dependency shown in Figure 5-36, similar to that obtained for the empirical repulsion-only potential (Figure 5-33).

Chapter 6. Conclusions

In order to be able to increase the recording density of magnetic media all aspects of the media production process and media characteristics must be well understood to find the problems that occur and ways of overcoming them. Although computer models cannot take into account all aspects of the process they try to describe, they can provide useful information about the main effects that can occur in a specific situation, the reason they occur and how they can be influenced by controlling various parameters.

6.1. *Analysis of results*

The computational models presented here were developed in order to study how interactions between the magnetic particles influence the properties of granular magnetic materials, in terms of magnetic characterisation but also in terms of the microstructure obtained from the fabrication process.

The model used to describe the magnetic behaviour of a particle system takes into account dipolar and exchange interactions in the presence of thermal effects, based on the Stoner-Wohlfarth theory combined with a standard Metropolis algorithm for energy minimisation. It is capable of simulating a whole series of magnetic properties for a given system, from various magnetisation curves to ferromagnetic resonance and magnetotransport measurements. A significant improvement in terms of computational time was achieved by the use of the effective field as a mean of finding the minimum and maximum energy orientations of the magnetic moment for a Stoner-Wohlfarth particle, coupled with a scheme of pre-calculating the interaction tensor components, enabling the simulation of a hysteresis loop for a relatively large system of particles in a matter of minutes.

Although this type of calculation has been performed before, previous work lacked a systematic study of the influence of magnetic (anisotropy constant, exchange interaction) and microstructure (packing density) parameters. Results were obtained for microstructures corresponding to granular systems using Co saturation magnetisation and a range of anisotropy constants, with and without exchange interactions. These calculations did not aim to fit a certain set of experimental data but rather to help understanding what properties (either magnetic or structural) of a studied sample can produce a certain magnetic behaviour thus trying to help interpretation of effects observed in experimental data.

The results show that in the absence of exchange interactions and at negligible thermal effects the system is dominated by the formation of closure vortex structures due to the magnetostatic interactions. The closure structures formed favour the demagnetised state and decrease the magnetic order. As the packing density of the magnetic material is increased, leading to an increase in magnetostatic interactions, both remanence and coercivity decrease while the GMR, which is a measure of local disorder of the magnetic moments, increases. The broadening of both the SFD and FMR curves with increasing packing density also shows a large distribution in the local field acting on each individual particle, a distribution that is entirely due to the magnetostatic interactions present. These effects are present regardless of the anisotropy constant value. However, when the system has very strong anisotropy, the magnetic moments are influenced more by the orientation of each particle's easy axis rather than by the orientation of the local field thus reducing the effects of the magnetostatic interaction. Higher remanence and higher coercivity values are induced, as expected, by the increase in the anisotropy constant while the broadening of the FMR response is diminished.

When thermal effects become important, in the absence of interactions most particles become superparamagnetic. The magnetostatic interactions brought in by the increase in the packing fraction lead to an increase in the local energy barrier resulting in an increase in remanence and coercivity, the opposite effect from the one observed at low temperatures. Basically, a superparamagnetic system can gain enough energy from magnetostatic interactions to overcome thermal effects and exhibit hysteretic behaviour. The two different effects can compensate each other for a given temperature keeping the coercivity approximately constant when the packing density is increased or, they can

become dominant at different packing densities, the coercivity of the system increasing from zero to a maximum by increasing energy barriers and then decreasing by formation of flux closure.

Being a short-range type of interaction, the effects of exchange interactions are generally more obvious in systems with high packing densities. When exchange coupling is present, the magnetic moments of the particles tend to align and cooperative reversals are encouraged. The local alignment produces an increase in the remanence of such systems while the cooperative reversals decrease their coercivity. The alignment effect is better shown by the reduction in GMR and its linewidth which implies that the average scalar product between neighbouring magnetic moments does not change as much from the saturated state to the coercive state as in the case with no exchange interactions. This implies that even at coercivity when the overall magnetic moment of a sample is zero, the magnetic configuration being in the least organized state, local magnetic order is present.

Since magnetostatic and exchange coupling interactions have opposite effects on remanence, a competition between the two occurs as the packing density is increased and the system, initially dominated by the dipolar interactions becomes increasingly influenced by the exchange field. This behaviour has been obtained for a certain set of parameters as a dip of the remanence plotted versus packing density.

While exchange coupling interactions have a similar effect as the magnetostatic interactions on the FMR linewidth, i.e. it produces an increase of the linewidth with the packing density, they also affect the value of the resonance field leading to a dramatic decrease going even to negative fields for large values of the anisotropy constant. This decrease is approximately linear with the strength of the exchange coupling. There is a striking similarity in the behaviour of the FMR response when varying the exchange interactions and the value of the damping parameter respectively. An increase in either exchange coupling or α leads to a decrease of the FMR peak, a decrease of the resonance field value and a broadening of the FMR curve corresponding to an increase in the line-width. Further work is required to establish if there is a link between the two effects or the similar behaviour is just a coincidence. Also, since the formulas used for the calculations of the FMR response are valid only when the magnetic moment is in an energy minima, thermal effects couldn't be used in the FMR calculations. In order to include these thermal

effects, a Landau-Lifshitz approach with a thermal stochastic term can be used to describe the dynamics of the magnetic moments and the FMR response.

The described model has also proved its usefulness at reproducing experimental measurement techniques used to obtain values for parameters that are not very well defined in a system such as activation volume. A good agreement in the activation volume trends obtained by experiments and simulations respectively has been obtained. At the same time, the model helped proving consistency between the S/χ_{irr} and the corrected waiting time methods used to estimate the activation volume while showing that the uncorrected waiting time method produces results that can be significantly different from those obtained with the other two. However, these results have only been obtained for non-interacting systems and studying the effect of magnetostatic and exchange interactions on the activation volume will be the subject of a different project.

The particulate media model described in Chapter 4 was developed to study the effects that particle clusters have on the microstructures obtained in the fabrication process. Experimentally is very difficult to differentiate between the effects brought by the intrinsic properties of the clusters and those produced by the cluster influence of the non-cluster particles and for this reason a model of such media was developed.

Simulations show that, regardless of the presence of clusters in the system, the orienting field pulse that is applied in order to align the particles to the direction of the tape must have a duration above a critical value, that depends on the strength of the field, in order to obtain a reasonably good alignment of the free particles. The particle alignment described by the squareness of the hysteresis loop has an asymptotic behaviour when plotted versus the duration of the orienting field pulse and the critical pulse length depends mainly on the field value and the viscosity of the solvent in which the particles are distributed.

Also, in order to obtain values for squareness and coercivity that are comparable with the experimental ones, the number of cluster particles present in the system must be significant (about 20%). The analysis of the free particles in a system that also contains clusters shows that the reduction in the value of the squareness is due not only to the intrinsic low squareness value of the clusters but also to a lower squareness of the free particles. This is presumably due to a disruption of the free particle alignment brought by

the presence of the clusters with their randomly oriented particles. The steric interactions between the free particles and clusters do not allow the free particles to perfectly align in the direction of the orienting field, as usually happens when no clusters are present in the system, thus reducing the degree of alignment in the free particles.

Another important aspect revealed by the simulations is the fact that the cluster size has no significant impact on the squareness of the microstructure as long as the ratio between cluster particles and free particles remains constant. This is despite the fact that smaller clusters tend to have higher anisotropy than larger ones and thus when aligned in the field have higher squareness, and is presumably due to the fact that a larger percentage of small clusters has a more disruptive effect on the free particles than a smaller percentage of large clusters. However, further work is needed to validate this hypothesis and other parameters such as variation of the solvent's viscosity with time can be added for a more complete description of such systems.

Chapter 5 of the thesis presents the Monte-Carlo model developed to understand the mechanisms by which the self-assembly process occurs in systems of surfactant coated magnetic particles and the results obtained with it.

Since the particles involved have nano-scale size, the thermal effects become very important and thus a first goal of the model was to estimate the conditions required in order to make possible the alignment of the particle's easy axes. The results supported both by the Monte-Carlo model and by statistical analysis show that for a good alignment a strong coupling between both the magnetic moment and the easy axis and the magnetic moment and the applied field respectively is needed. A very strong orienting field will not produce the desired alignment if it is not backed up by a large enough anisotropy within the particles. A simple theoretical solution that can be used to overcome this is an increase in the particle size that would be reflected in a corresponding increase of both magnetostatic and anisotropy energy that are proportional to the particle volume.

Amongst the parameters that influence the self-assembly process, of major importance is the areal density of particles which needs to be large enough for the particles to interact via the steric repulsive potential but at the same time not as large as to produce formation of multilayers. The lower critical value for the areal density is determined mostly by the length of surfactant molecules that coat the nanoparticles while the upper critical

value is determined by the strength of the interparticle potential and the strength of the surface-tension potential. Another condition that is required in order to obtain long-range self-assembled systems is a very narrow distribution of particle sizes. The simulations have shown that the maximum standard deviation allowed for which the long-range order is maintained is of about 5%.

The fact that in some particular systems local self-assembly has been observed experimentally even when the areal particle density was below the critical region led to the conclusion that in some circumstances the nature of the interparticle interaction potential changes from repulsion to attraction. The model proposes a phenomenological interaction potential that has an initial repulsion barrier, followed by an attraction well and another much stronger repulsion barrier, as the interparticle distance decreases. This potential can explain the repulsion existent between particles in colloidal state when no aggregates are formed but also the possibility of attraction between particles when the initial energy barrier has been overcome. This form of interaction potential produces results in agreement with the experimental ones.

Although in most cases the samples self-ordered in a hexagonal lattice, specific conditions can also produce square lattices, effect that is successfully described by model. In agreement with analytical results it has been shown that there is a range of areal densities for which the square lattice has lower energy than the hexagonal one, a range that depends solely on the type of interparticle interaction potential.

6.2. *Further work*

The capabilities of the models described here extend beyond the simulations performed so far. The granular media model as described can be used with minor changes to characterise other types of recording media, just by using the appropriate texture of particle arrangement and orientation of easy axis. The use of the effective anisotropy field in performing the Stoner-Wohlfarth calculations can be extended from uniaxial to cubic anisotropy materials although in this case the energy barrier would need a different approach. By explicitly including both interactions and thermal effects, the model can be

used to simulate most equilibrium magnetisation curves thus being able to provide means of validating the interpretation of experimental results. Such is the case of the activation volume simulations where a systematic study on the effect of interactions is possible. Also, in this study the interaction effects were considered only within a sample in which each particle has the same applied field and temperature. This study may be taken further to investigate, for larger systems, the interaction effects that occur in a "recorded" sample, i.e. in a sample where a transition occurs between two regions with different magnetisation orientations, similar to the transition between written bits. This would permit to establish the conditions for an improvement of the signal-to-noise ratio and also how the interactions between the two regions influence spontaneous reversals occurring in the transition region. Another approach would be the use of a temperature gradient in the computational cell to simulate the effects that occur in the so-called "heat assisted magnetic recording" (HAMR) processes that are now being used in the magnetic recording industry.

The inclusion of the Landau-Lifshitz equation in the model also makes possible the description of some dynamic measurements making possible a comparison between the two approaches. An initial comparison has been made between the FMR results obtained via the static description of the susceptibility for a Stoner-Wohlfarth particle and the results obtained with the dynamic Landau-Lifshitz approach. This comparison showed an excellent agreement between the two for systems with dipolar interactions only but a significant difference occurs when exchange interactions are present. It is important to establish what determines this difference and in what conditions can the static approach be successfully used and when the more time-consuming but presumably more accurate dynamic approach must be used.

The particulate media model is currently based on an empirical description: it introduces preformed particle clusters and treats the whole mixture of solvent, resins and coating agents as a fluid with uniform constant viscosity. Although these simplifications greatly reduce the computational time while still describing the main properties of the system, a more rigorous approach is needed for a more in detail description of the sample.

Although the self-assembly model describes quite accurately the experimental results, a better description of the interaction and surface potentials is needed in order to obtain realistic approximations for the critical parameters obtained when using the

phenomenological potential. Further quantum computations may be needed in order to estimate the interactions between the surfactant molecules.

A systematic magnetic characterisation of the configurations obtained is also required to estimate the effects of interactions and thermal activation on the media, enabling an estimation of the most appropriate microstructure properties needed to obtain maximum performance i.e. areal density and stability.

Although the three models described have been developed with different goals in mind, they provide the means for investigating properties of various types of recording media and the magnetic model of the granular media is sufficiently flexible to allow the use of the results produced by the other two models as microstructure configuration enabling thus prediction of their magnetic properties.

Appendix 1. Numerical solution for the Stoner-Wohlfarth model

The C++ implementation of the numerical solution described in 2.2.2 is given below. The implementation uses the classes Vec, representing a 3D vector and Dir representing a 3D orientation via a normalised vector, classes with the implementation freely available at www.dur.ac.uk/claudiu-georgel.verdes/cpp.zip.

```
template<class T>      //std::max not available on VC++6.0
inline const T& Max (const T& a, const T& b)
{
        return a < b ? b : a;
}

double abs_val (const Vec& v)
{
        return Max (fabs (v.x), Max (fabs (v.y), fabs (v.z)));
}

// Finds one equilibrium position for the SW model. Parameters:
// ea – easy axis orientation
// fld – local field normalised to Hk
// mom – input – initial orientation of the moment
//       – output – final orientation of the moment
// maxErr - precision
void SW(const Dir& ea, const Vec& fld, Dir& mom, double maxErr)
{
        Vec momOld(mom);

        while(true)
        {
                mom.Import((ea*mom)*ea + fld);
                momOld -= mom;
                if( abs_val(momOld) < maxErr )
                        break;
                momOld = mom;
        }
}

// Finds the two equilibrium positions of the SW model. If only one equilibrium position
// exists mom1 and mom2 are identical. Parameters:
// ea – easy axis orientation
```

```
// fldVal – normalised value of the local field
// fldDir – orientation of the local field
// mom1 (output) – orientation of moment for which first energy minima is obtained
// mom1 (output) – orientation of moment for which second energy minima is obtained
// maxErr – precision
void SW_Sols( const Dir& ea, double fldVal, const Dir& fldDir,
                        Dir& mom1, Dir& mom2, double maxErr)
{
        double cosTh = ea * fldDir;

        double hx2;
        if( fabs(fldVal) <= 1.0 )
        {
                hx2 = 1.0 - pow(fabs(cosTh*fldVal), 2.0/3.0);
                hx2 *= hx2 * hx2;
        }
        else
                hx2 = 0;

        // are we inside the astroid? – two equilibrium positions
        if( fldVal * fldVal * (1 - cosTh * cosTh ) <= hx2 )
        {
                mom1 = ea;
                mom2 = -ea;
                SW(ea, fldVal * fldDir, mom1, maxErr);
                SW(ea, fldVal * fldDir, mom2, maxErr);
                return;
        }

        // just one equilibrium position
        mom1 = ( fldVal * cosTh < 0 ) ? -ea : ea;
        SW(ea, fldVal * fldDir, mom1, maxErr);
        mom2 = mom1;
}
```

Appendix 2. Numerical solution for the Stoner-Wohlfarth energy maximum

```
//  Finds the orientation of the maximum energy for a SW particle in a given field.
Parameters:
// ea – easy axis orientation
// fldVal – normalised value of the local field
// fldDir – orientation of the local field
// mom (output) – orientation of moment for which maximum energy is obtained
// maxErr – precision
```

```
void SW_max(const Dir& ea, double fldVal, const Dir& fldDir,
                        Dir& mom, double maxErr)
{
        if (fabs (fldVal) < maxErr )
                mom.Import (ea.Cross(Dir::ux));
        else
        {
                Dir rotAx;
                if (rotAx.Import (Sign(fldVal) * ea.Cross (fldDir)) < maxErr)
                        rotAx.Import (ea.Cross(Dir::ux));
                Dir eaMax(rotAx.Cross (ea));
                mom = eaMax;
                SW(eaMax, (-fldVal) * fldDir, mom, maxErr);
        }
}
```

References:

[1] S. H.Charap, P. L. Lu, Y. J. He, "Thermal stability of recorded information at high densities", IEEE Trans. Magn, 33 (1), 978 (1997)

[2] K. Stoev, F. Liu, Y. Chen, X. Dang, P. Luo, J. Chen, J. Wang, K. Kung, M. Lederman, M. Re, G. Choe, J. N. Zhou, M. Yu, "Demonstration and characterization of 130 Gb/in^2 magnetic recording systems", J. Appl. Phys. 93(10), 6552 (2003)

[3] B. D. Cullity, "Introduction to magnetic materials", Addison-Wesley Publ., (1972) 413

[4] http://www.ee.washington.edu/conselec/CE/kuhn/magtape/95x1.htm

[5] M. P. Sharrock, "Particulate magnetic recording media - a review", IEEE Trans. Magn, 25 (6), 4374 (1989)

[6] J. I. Martin, J. Nogues, K. Liu, J. L. Vicent, I. K. Schuller, "Ordered magnetic nanostructures: fabrication and properties", J. Magn. Magn. Mat. 256 (1-3) 449 (2003)

[7] I. D. Mayergoyz, "Mathematical models of hysteresis", IEEE. Trans. Magn., 22(5), 603 (1986)

[8] E. Della Torre, "Measurements of interaction in an assembly of γ-iron oxide particles", J. Appl. Phys., 36(2), 518 (1965).

[9] D. C. Jiles, D. L. Atherton, "Theory of ferromagnetic hysteresis (invited)", J. Appl. Phys. 55(6), 2115 (1984)

[10] J. G. Zhu and N. Bertram, "Micromagnetic studies of thin metallic-films", J. Appl. Phys., 63, 3248 (1988)

[11] D. Kechrakos and K. N. Trohidou, "Magnetic properties of dipolar interacting single-domain particles", Phys. Rev. B., 58, (1998) 12169

[12] M. El-Hilo, R. W. Chantrell and K. O'Grady, "A model of interaction effects in granular magnetic solids", J. Appl. Phys., 84(9), (1998) 5114

[13] G. N. Coverdale, R. W. Chantrell, A. Satoh, R. Vietch, "Molecular dynamic model of the magnetic properties and microstructure of advanced metal particle dispersions", J. Appl. Phys, 81 (8), (1997) 3818

[14] Y Gunal, P. B. Visscher, "Brownian dynamics simulation of magnetic colloid aggregation", IEEE Trans. Mag., 32 (5), (1996) 4049

[15] S. Salaniwal, S. T. Cui, P. T. Cummings, H. D. Cochran, "Self-assembly of reverse micelles in water/surfactant/carbon dioxide systems by molecular simulation", Langmuir, 15 (16) 5188 (1999)

[16] J. B. Maillet, V. Lachet, P. V. Coveney, "Large scale molecular dynamics simulation of self-assembly processes in short and long chain cationic surfactants", Phys. Chem. Chem. Phys, 1 (23), 5277 (1999)

[17] J. L. Dormann, L. Bessais, and D. Fiorani, "A dynamic study of small interacting particles - superparamagnetic model and spin-glass laws", J. Phys. C., 21, 2015 (1988)

[18] J. L Dormann, D. Fiorani and E. Tronc, "On the models for interparticle interactions in nanoparticle assemblies: comparison with experimental results", J. Mag. Mag. Mat., 202 (1), 251, (1999)

[19] J. L. Dormann, D. Fiorani and E. Tronc, "Magnetic relaxation in fine-particle systems", Adv. Chem. Phys., 98, (1997) 283

[20] S. Morup, "Superferromagnetic nanostructures", Hyperfine Interact. 90, (1994) 171

[21] S. Morup and E. Tronc, "Superparamagnetic relaxation of weakly interacting particles", Phys. Rev. Lett., 72 (20), 3278 (1994)

[22] M. F. Hansen and S. Morup, "Models for the dynamics of interacting magnetic nanoparticles", J. Mag. Mag. Mat, 184 (3), 262 (1998)

[23] P. Allia, M. Coisson, M. Knobel, P. Tiberto, F. Vinai, "Magnetic hysteresis based on dipolar interactions in granular magnetic systems", Phys. Rev. B, 60 (17), 12207 (1999)

[24] G. N. Coverdale, R. W. Chantrell, "Calculations of the microstructure and magnetic properties of particulate recording media", J. Mag. Mag. Mat., 209 (2000), 21

[25] G. N. Coverdale, A. Satoh, R. G. Gilson and R. W. Chantrell, "Computational studies of the orientation of advanced particulate media during coating and drying", J. Mag. Mag. Mat, 193 (1999), 322

[26] P. B. Visscher, Y. Gunal, "Field-induced smectic ordering in model magnetic inks" J. Appl. Phys 81 (8), (1997) 3827

[27] R.E. Rosensweig, "Ferrohydrodynamics", Dover Publications Inc., Mineola NY (1985)

[28] C. G. Verdes, B. Ruiz-Diaz, S. M. Thompson, R. W. Chantrell and Al. Stancu, "Computational model of the magnetic and transport properties of interacting fine particles", Phys. Rev. B, 65, (2002) 174417

[29] W. J. Antel, H. Laidler, K. O'Grady, C. Verdes, R. W. Chantrell, "Determination of activation volumes in thin film media", J. Appl. Phys, 91 (10), 7080 (2002)

[30] Dumitru I., Sandu D. D. and Verdes C. G., "Model of ferromagnetic resonance in interacting fine particle systems", Phys. Rev. B, 66 (10), 104432 (2002)

[31] C. G. Verdes, B. Ruiz-Diaz, R. W. Chantrell, S. Thompson and A. Stancu, "Monte Carlo simulations of interaction effects on magnetic viscosity in ferromagnetic granular media", Int. J. Appl. Electrom., 13 (1-4), 251 (2001)

[32] C. G. Verdes, B. Ruiz-Diaz, R. W. Chantrell, S. Thompson and A. Stancu, "Model of ferromagnetic resonance in granular magnetic solids", J. Appl. Phys. 89 (11), 7475 (2001)

[33] E. C. Stoner and P. Wohlfarth, "A mechanism of magnetic hysteresis in heterogeneous alloys", Phil. Trans. R. Soc. London, Ser. A 240, (1948) 599

[34] Al. Stancu, "Capitole speciale de magnetism", Editura Universitatii Iasi, Romania, 1995.

[35] O'Dell T. H. "Ferromagnetodynamics", Macmillan (1981)

[36] Mallinson J. C., "On damped gyromagnetic precession", IEEE Trans. Magn., 25 (5), 2662 (1989)

[37] W. H. Press, B. P. Flannery, S. A. Teukolsky, W. T. Vetterling, "Numerical recipes in Fortran", Cambridge University Press, (1992)

[38] I. S. Jacobs and C. P. Bean, "Magnetism", III, G. T. Rado and H. Suhl, Eds. New York: Academic, (1963) 271

[39] E. P. Wohlfarth, "Magnetism", III, G. T. Rado and H. Suhl, Eds. New York: Academic, (1963) 351

[40] L. Néel, Progress in Low Temperature Physics, 1, C. J. Gorter, Ed., (1955), 336

[41] W. F. Brown Jr., "Thermal fluctuations of fine ferromagnetic particles", IEEE Trans. Magn, 15(5), (1979) 1196

[42] C. P. Bean and L. D. Livingstone, J. Appl. Phys. 30, (1959), 120S

[43] W. F. Brown, J. Appl. Phys. 34, (1963) 1319

[44] H. Pfeiffer, "Determination of anisotropy-field distribution in particle assemblies taking into account thermal fluctuations", Phys. Status Solidi A 118, (1990) 295

[45] N. Metropolis, A. W. Rosenbluth, M. N. Rosenbluth, A. H. Teller and E. Teller, J. Chem. Phys 21, (1953) 1087

[46] Mansuripur M. and Giles R., "Demagnetizing field computation for dynamic simulation of the magnetization reversal process", IEEE Trans. Magn., 24 (6), (1988) 2326

[47] Y. Suganuma, H. Tanaka, M. Yanagisawa, F. Goto, S. Hatano, "Production process and high-density recording characteristics of plated disks", IEEE Trans. Magn. 18 (6), 1215 (1982)

[48] R. Hiskes, S. A. Dicarolis, J. L. Young, S. S. Laderman, R. R. Jacowitz, R. C. Taber, "Single source metalorganic chemical vapor-deposition of low microwave surface-resistance $YBa_2Cu_3O_7$", Appl. Phys. Lett. , 59 (5), 606 (1991)

[49] G. N. Kakazei, A. F. Kravetz, N. A. Lesnik, M. M. P. de Azevedo, Y. G. Pogorelov, G. V. Bondarkova, V. I. Silantiev, J. B. Sousa, "Influence of co-evaporation technique on the structural and magnetic properties of CoCu granular films", J. Mag. Mag. Mat, 197, 29 (1999)

[50] S. Stavroyiannis, I. Panagiotopoulos, D. Niarchos, J. A. Christodoulides, Y Zhang and G. C. Hadjipanayis "CoPt/Ag nanocomposites for high density recording media", Appl. Phys. Lett., 73 (23), 3453 (1998)

[51] M. P. Allen, D. J. Tildesley, "Computer simulation of liquids", Oxford University Press, (1989) 349

[52] C. Dean, R. W. Chantrell, A. Hart, D. A. Parker and J. J. Miles, "Remanence curves of longitudinal thin-films", IEEE Trans. Magn., 27, (1991) 4769

[53] V. Franco, X. Batlle, A. Labarta, and K. O'Grady, "The nature of magnetic interactions in CoFe-Ag(Cu) granular thin films", J. Phys. D, 33, (2000) 609

[54] R. W. Chantrell, N. S. Walmsley, J. Gore and M. Maylin, "Calculations of the susceptibility of interacting superparamagnetic particles", Phys. Rev. B, 63, (2001) 024410

[55] R. W. Chantrell, "Magnetic viscosity of recording media", J. Mag. Mag. Mat, 95 (3), 365 (1991)

[56] R.D. Zysler, D. Fiorani, A.M. Testa, "Investigation of magnetic properties of interacting Fe_2O_3 nanoparticles" J. Mag. Mag. Mat., 224 (1), 5 (2001)

[57] L. Néel, Ann. Geophys. 5, 99 (1949)

[58] E. P. Wohlfarth, J. Phys. F: Met. Phys. 14, 155 (1961)

[59] M. El-Hilo, K. O 'Grady, R. W. Chantrell "Fluctuation field and reversal mechanisms in granular magnetic systems", J. Mag. Mag. Mat., 248, 360 (2002)

[60] A. E. Berkowitz, J. R. Mitchell, M. J. Carey, A. P. Young, S. Zhang, F. E. Spada, F. T. Parker, A. Hutten, G. Thomas, "Giant magnetoresistance in heterogeneous cu-co alloys", Phys. Rev. Lett, 68 (25), 3745 (1992)

[61] J. I. Gittleman, Y. Goldstein, and S. Bozowski, "Magnetic Properties of Granular Nickel Films", Phys. Rev. B 5, 3609 (1972)

[62] J. F. Gregg, S. M. Thompson, S. J. Dawson, K. Ounadjela, C. R. Studdon, J. Hamman, C. Ferman, G. Saux, and K. O'Grady, "Effect of magnetic-interactions and multiple magnetic phases on the giant magnetoresistance of heterogeneous cobalt-silver thin-films", Phys. Rev. B 49, 1064 (1994)

[63] Netzelmann U. "Ferromagnetic-resonance of particulate magnetic recording tapes", J. Appl. Phys, 68 (4), 1800 (1990)

[64] A.H. Thomas, R.W. Chantrell, M. El-Hilo, P.W. Haycock, K. O'Grady "Calculation of FMR in interacting fine particle systems", J. Mag. Mat. Mat., 151, 54 (1995)

[65] K. O'Grady, R. G. Gilson and P. C. Hobby, "Magnetic pigment dispersions (a tutorial review)", J. Mag. Mag. Mat., 95 (1991) 314

[66] G. N. Coverdale, "Computer simulation of the structure and properties of a particulate dispersion", PhD thesis, University of Central Lancashire, (1994)

[67] Seiichi Hisano and Kazuhisa Saito, "Research and development of metal powder for magnetic recording", J. Mag. Mag. Mat., 190 (1998), 371

[68] N. K. Nelson and K. R. Wormuth, "Rheology and microstructure of metal particulate dispersions for data storage applications", proceedings of XIIIth International Congress on Rheology, Cambridge, UK (2000)

[69] J. J. Newman and R. B. Yarbrough, "Motions of a magnetic particle in a viscous medium", J. Appl. Phys, 39, (1968) 5566

[70] J. J. Newman and R. B. Yarbrough, "Theory of the motions of a fine magnetic particle in a Newtonian fluid" IEEE Tans. Mag., (1969) 30

[71] J. J. Newman, "Orientation of magnetic particle assemblies", IEEE Trans. Mag. (1978) 866

[72] P. H. Lissberg and R. L. Comstock, "Orientation of magnetic particles in a recording medium", IEEE Trans. Mag., (1971) 259

[73] Y. Ishii, M. Sato, "Magnetic behaviors of 2 spheres which contact each other with an area", J. Appl. Phys., 57(2), 465 (1985)

[74] Y. Ishii, M. Sato, "Magnetic behaviors of elongated single-domain particles by chain-of-spheres model", J. Appl. Phys., 59(3), 880 (1986).

[75] Huisman H. F, "Dispersion of (magnetic) pigment powders in organic liquids", J. Coating Technology, 57 (727), (1985) 49

[76] J. F. Smyth, S. Schultz, D. Kern, H. Schmid and D. Yee, "Hysteresis of sub-micron permalloy particulate arrays", J. Appl. Phys. 63 (8): 4237 (1988)

[77] P. B. Fischer and S. Y. Chou, "10-nm electron-beam lithography and sub-50-nm overlay using a modified scanning electron-microscope", Appl. Phys. Lett. 62 (23) 2989 (1993)

[78] F. Rousseaux, D. Decanini, F. Carcenac, E. Cambril, M. F. Ravet, C. Chappert, N. Bardou, B. Bartenlian and P. Veillet, "Study of large area high density magnetic dot arrays fabricated using synchrotron radiation based x-ray lithography", J. Vac. Sci Technol. B 13 (6) 2787 (1995)

[79] O. Fruchart, M. Klaua, J. Barthel and J. Kirschner, "Self-organized growth of nanosized vertical magnetic Co pillars on Au(111)", Phys. Rev. Lett. 83 (14) 2769 (1999)

[80] M. Farhoud, M. Hwang, H. I. Smith, M. L. Schattenburg, J. M. Bae, K. Youcef-Toumi and C. A. Ross, "Fabrication of large area nanostructured magnets by interferometric lithography", IEEE Trans. Magn. 34 (4) 1087 (1998)

[81] T. A. Savas, M. Farhoud, H. I. Smith, M. Hwang and C. A. Ross, "Properties of large-area nanomagnet arrays with 100 nm period made by interferometric lithography", J. Appl. Phys. 85 (8) 6160 (1999)

[82] "Nucleation of ordered Ni island arrays on Au(111) by surface-lattice dislocations", D. D. Chambliss, R. J. Wilson and S. Chiang, Phys. Rev. Lett. 66 (13) 1721 (1991)

[83] L. Zhang and A. Manthiram, "Experimental study of ferromagnetic chains composed of nanosize Fe spheres", Phys. Rev. B 54 (5) 3462 (1996)

[84] M. Giersig and M. Hilgendorff, "The preparation of ordered colloidal magnetic particles by magnetophoretic deposition", J. Phys. D-Appl. Phys. 32 L111 (1999)

[85] C. Petit, A. Taleb and M. P. Pileni, "Cobalt nanosized particles organized in a 2D superlattice: Synthesis, characterization, and magnetic properties", J. Phys. Chem. B 103 (11) 1805 (1999)

[86] S. H. Sun, C. B. Murray, D. Weller, L. Folks and A. Moser, "Monodisperse FePt nanoparticles and ferromagnetic FePt nanocrystal superlattices", Science 287 (5460) 1989 (2000)

[87] R. W. Chantrell, private communication.

[88] N. Shukla, J. Ahner, private communication.